

NASA CONTRACTOR REPORT

NASA CR-2882



NASA CR-2

0061721



LOAN COPY: RETURN TO
AFWL TECHNICAL LIBRARY
KIRTLAND AFB, N. M.

ANALYTICAL AND EXPERIMENTAL STUDIES OF ACOUSTIC PERFORMANCE OF SEGMENTED LINERS IN A COMPRESSOR INLET

*R. E. Motsinger, R. E. Kraft,
J. E. Paas, and B. M. Gabn*

Prepared by
GENERAL ELECTRIC COMPANY
Evendale, Ohio 45215
for Langley Research Center



NATIONAL AERONAUTICS AND SPACE ADMINISTRATION • WASHINGTON, D. C. • SEPTEMBER 1977

FOREWORD

The authors would like to express their gratitude to the numerous individuals whose dedicated efforts contributed significantly to the successful completion of the entire program. Especially appreciated was the assistance provided by Mr. L.R. Clark of the Acoustics Branch, NASA-Langley Research Center. Mr. Clark was responsible for coordinating the overall experimental effort at NASA-LRC. This included setting up the test hardware and instrumentation operation of the Langley noise-research compressor, and acquisition of the test data. The authors would also like to acknowledge the assistance provided by: W. Ruehr, who designed and procured the inlet test hardware, directed the aerodynamic testing, and analyzed these data; by W. Cardwell who, together with W. Albertson, designed the spinning-mode probe system and directed its procurement, and further, who provided invaluable assistance operating the mode probe equipment during the testing; by R. Williamson, who calibrated and set up the hot film instrumentation and assisted with the test data acquisition; and by J. Lyons, who coordinated the contractual reporting and completion of contractual commitments throughout the program. The assistance and cooperation in conducting the anechoic chamber test extended by R. Padelt, T. Miller and W. Saunders of NASA-LRC was also excellent. A special thanks is given to Dr. J. Posey of NASA-LRC for his important contributions and assistance during the "ACTAMD" program verification and analysis of spinning mode results. These activities were essential to the successful completion of the program and are greatly appreciated.

Table of Contents

<u>Section</u>		<u>Page</u>
	LIST OF ILLUSTRATIONS	vii
	LIST OF TABLES	xii
	LIST OF SYMBOLS AND DEFINITIONS	xiii
1.0	SUMMARY	1
2.0	INTRODUCTION	3
3.0	OBJECTIVES	5
4.0	THEORETICAL CONSIDERATIONS	7
	4.1 Liner Design	7
	4.2 Wave Field Theory	10
	4.3 Mathematical Model of Test Vehicle	12
5.0	EXPERIMENT	15
	5.1 Experimental Facility and Test Apparatus	15
	5.1.1 Anechoic Chamber	15
	5.1.2 Test Vehicle	15
	5.1.3 Inlet Hardware	20
	5.1.4 Acoustic Treatment Panels	20
	5.2 Instrumentation and Data Acquisition/Reduction	29
	5.2.1 Acoustic	29
	5.2.2 Aerodynamic	34
	5.3 Test Program	42
	5.3.1 Acoustic	42
	5.3.2 Aerodynamic	42
	5.4 Acoustic Data Scaling	42
6.0	RESULTS AND DISCUSSION	47
	6.1 Analysis of Spinning Mode Probe Results	47
	6.1.1 Determination of Modal Information for Use in ACTAMD	47
	6.1.2 Repeatability	55

Table of Contents (Concluded)

<u>Section</u>	<u>Page</u>
6.2 Cylindrical Inlet	60
6.2.1 Basic Experimental Data	60
6.2.2 Comparison of Results with Predictions	72
6.2.3 Sensitivity Studies	82
6.3 High Mach Inlet	91
6.3.1 Acoustic Data	93
6.3.2 Aerodynamic Performance of High Mach Inlet	108
6.4 Inlet Turbulence and Associated Noise for this Experimental Test Configuration	108
6.4.1 Turbulence Data	111
6.4.2 Acoustic Data	117
7.0 CONCLUSIONS	129
REFERENCES	131

LIST OF ILLUSTRATIONS

<u>Figure</u>		<u>Page</u>
1.	Schematics of Treated Cylindrical Inlet and ACTAMD Mathematical Model.	13
2.	NASA-Langley Research Center Anechoic Chamber.	16
3.	NASA-Langley Research Center Anechoic Chamber Test Vehicle with Treated Inlet.	17
4.	Speed Flow Relationship for High Mach Number Inlet.	18
5.	Inlet Designs with Replaceable Panels.	21
6.	Throat Mach Number/Fan Speed Relationship for High Mach Number Inlet.	22
7.	Wall Mach Number Distribution at Design Speed for High Mach Number Inlet.	23
8.	Inlet Turbulence Screen Installed on Test Vehicle.	24
9.	Inlet Turbulence Screen Dimensions.	25
10.	Representative Cylindrical-Inlet Liners.	27
11.	Liner Reactances.	28
12.	Dependence of End Correction Coefficient, K, on Mach Number.	30
13.	In-Duct Microphone and Probe Instrumentation.	31
14.	Spinning-Mode Probe Assembly.	32
15.	Individual Probe.	33
16.	High Mach Number Inlet Rake Total Pressure Profiles.	36
17.	Hot Film Probe Installation in Test Rig.	38
18.	Hot Film Probe Assembly.	39
19.	Block Diagram of Hot Film Probe Instrumentation Setup.	40
20.	Complex Pressure Profile from 40 Hz Bandwidth Cross Spectrum, 44% Speed, 3440 Hz, Blade Passing Frequency, Hardwall Configuration.	48

LIST OF ILLUSTRATIONS (Cont'd)

<u>Figure</u>		<u>Page</u>
21.	Measured Spinning-Mode Content for 44% Speed, 3440 Hz, Blade Passing Frequency.	49
22.	Complex Pressure Profile from 40 Hz Bandwidth Cross Spectrum, 44% Speed, 6920 Hz, Second Harmonic, Hardwall Configuration.	50
23.	Measured Spinning Mode Content, for 44% Speed, 6920 Hz, Second Harmonic.	51
24.	Complex Pressure Profile from 40 Hz Bandwidth Cross Spectrum, 79% Speed, 6120 Hz, Blade Passing Frequency, Hardwall Configuration.	52
25.	Measured Spinning-Mode Content for 79% Speed, 6120 Hz, Blade Passing Frequency.	53
26.	Explanation of Mode Probe Data Redundancy.	56
27.	Complex Pressure Profile from 40 Hz Bandwidth Cross Spectrum, 44% Speed, 3440 Hz, Blade Passing Frequency, Hardwall Configuration, Comparing Repeatability of Data Acquired with Two Different Probes Over Same Arc.	57
28.	Inlet and Mode Probe Configuration for Test of Effects of Probe Position.	58
29.	Variation of Wall Microphone #3 BPF Cross-Spectrum as a Function of Spinning Mode Probe Azimuthal Position.	59
30.	Summary of Phased-Treatment Blade Passing Frequency PWL Suppression at Four Fan Speeds.	61
31.	Summary of Phased-Treatment 50° OASPL Suppression at Four Fan Speeds.	62
32.	Summary of Phased-Treatment OAPWL Suppression at Four Fan Speeds.	63
33.	Representative Phased-Treatment Sound Power Level at 74% N_{FC} .	64
34.	Representative Phased-Treatment OASPL Directivity at 74% N_{FC} .	66

LIST OF ILLUSTRATIONS (Cont'd)

<u>Figure</u>		<u>Page</u>
35.	Representative Phased-Treatment PNL Directivity at 74% N _{FC} .	67
36.	Comparison of Single-Phase and Hardwall 50° Far-Field Narrowband at 74% N _{FC} .	68
37.	Representative Phased-Treatment Sound Power Level at 89% N _{FC} .	69
38.	Representative Phased-Treatment OASPL Directivity at 89% N _{FC} .	70
39.	Representative Phased-Treatment PNL Directivity at 89% N _{FC} .	71
40.	Sound Power Level Spectra for Four Cylinder Inlet Configurations, 74% of Design Speed.	73
41.	Sound Power Level Spectra for Four Cylindrical Inlet Configurations, 89% of Design Speed.	74
42.	Comparison of Measured and PredictedSuppressions, 44% Speed, Blade Passing Frequency.	79
43.	Comparison of Measured and Predicted Suppressions, 44% Speed, Second Harmonic.	80
44.	Comparison of Measured and Predicted Suppressions, 79% Speed, Blade Passing Frequency.	81
45.	Predicted Suppression of Configuration AAA, 44% Speed, 3440 Hz, as a Function of Liner Resistance.	83
46.	Predicted Suppression of Configuration AAA, 44% Speed, 6920 Hz, as a Function of Liner Resistance.	84
47.	Radial Mode Shapes for Spinning Mode Orders $m = 1, 7,$ and 12.	88
48.	Comparison of Measured and Predicted Suppression for Two Different Modal Source Assumptions, 44% Speed, Second Harmonic.	89
49.	Comparison of Measured and Predicted Suppression for Two Different Modal Source Assumptions, 79% Speed, BPF.	90

LIST OF ILLUSTRATIONS (Cont'd)

<u>Figure</u>		<u>Page</u>
50.	Modal Participation at Entrance to Treated Section (Plane 2), Sixth Order Spinning Mode, 79% Speed, Blade Passing Frequency.	92
51.	One-Third Octave Band PWL Spectra for Five Inlet Configurations, 79% of Design Speed, $M_{TH} = 0.60$.	94
52.	One-Third Octave Band PWL Spectra for Five Inlet Configurations, 89% of Design Speed, $M_{TH} = 0.72$.	95
53.	One-Third Octave Band PWL Spectra for Five Inlet Configurations, 94% of Design Speed, $M_{TH} = 0.79$.	96
54.	High Mach Number Inlet, PNL Directivities at 79% N_{FC} ($M_{TH} = 0.60$) for Five Inlet Configurations.	97
55.	High Mach Number Inlet, PNL Directivities at 89% N_{FC} ($M_{TH} = 0.72$) for Five Inlet Configurations.	98
56.	High Mach Number Inlet, PNL Directivities at 94% N_{FC} ($M_{TH} = 0.79$) for Five Inlet Configurations.	99
57.	Maximum Perceived Noise Versus Vehicle Speed.	100
58.	Comparison of PNL Suppression with Other Representative High Mach Number Inlet Results.	102
59.	In-Duct Acoustic Probe Results at 89% N_{FC} ($M_{TH} = 0.72$) for Configuration 22 (Single Phase Treatment) as Measured Near the Wall).	104
60.	BPF Tone Suppression Based on Probe Results for High Mach Number Inlet.	105
61.	BPF Sound Pressure Levels on the Wall of the Single Phase Hybrid for Three Speed Settings.	107
62.	Wall Mach Number Distributions for the Accelerating-Hardwall Inlet.	109
63.	High Mach Number Inlet Recovery.	110
64.	Axial Turbulence Integral-Length Scale, Three Inlets, 74% and 89% N_{FC} , without Screen.	112

LIST OF ILLUSTRATIONS (Cont'd)

<u>Figure</u>		<u>Page</u>
65.	Axial Turbulence Integral-Length Scale, Three Inlets, 74% and 89% N_{FC} , with Screen.	113
66.	Mean-Velocity Profiles, Cylindrical Inlet.	114
67.	Mean-Velocity Profiles, Accelerating Inlet.	115
68.	Mean-Velocity Profiles, Hybrid Inlet.	116
69.	Axial Turbulence Intensity, with and without Inlet Screen, Cylindrical Inlet.	118
70.	Axial Turbulence Intensity with and without Inlet Screen, Accelerating Inlet.	119
71.	Axial Turbulence Intensity with and without Inlet Screen, Hybrid Inlet.	120
72.	Circumferential Turbulence Intensity with and without Inlet Screen, Cylindrical Inlet.	121
73.	Circumferential Turbulence Intensity with and without Inlet Screen, Accelerating Inlet.	122
74.	Circumferential Turbulence Intensity with and without Inlet Screen, Hybrid Inlet.	123
75.	Effect of Inlet Screen on PWL Spectra, Cylindrical Inlet.	124
76.	Effect of Inlet Screen on PWL Spectra, Accelerating Inlet.	125
77.	Effect of Inlet Screen on PWL Spectra, Hybrid Inlet.	126
78.	Effect of Inlet Screen on BPF 1/3 Octave Band Level as a Function of Farfield Angle, 74% N_{FC} .	128

LIST OF TABLES

<u>Table No.</u>		<u>Page</u>
I.	Predicted Suppressions.	9
II.	Compressor Stage Reference Information.	19
III.	Cylindrical Inlet Acoustic Test Points.	43
IV.	High Mach Inlet Acoustic Test Points.	44
V.	Mode Probe Acoustic Test Points (Cylindrical Inlet).	44
VI.	Scaling Parameters.	45
VII.	Effect of Changing Porosity in All Panels: One-Third Octave PWL Suppression at BPF, dB.	75
VIII.	Effect of Changing Porosity in One Panel Only: One-Third Octave PWL Suppression at BPF, dB.	76
IX.	Occurrence of Double Eigenvalues in Suppression Prediction Calculations.	78
X.	Effect of Radial Mode Content.	85
XI.	Number of Cut-On Radial Modes for Dominant Spinning Mode Orders.	87

LIST OF SYMBOLS

A	=	Voltage Signal from Sensor "A" of Hot Film Probe
A	=	Cross sectional area
A*	=	Cross sectional area at throat
ACTAMD	=	"Acoustic Theory of Axisymmetric Multisectioned Ducts" Computer Program
B	=	Number of blades
B	=	Voltage Signal from Sensor "B" of the Hot Film Probe
B&K	=	B&K Instruments, Inc. - Bruel & Kjaer Precision Instruments
B&H	=	Bell & Howell
BPF	=	Blade Passing Frequency
c	=	Speed of sound in a stationary medium
CTOL	=	Conventional takeoff and landing
d	=	Hole diameter
D	=	Vehicle inlet duct diameter
D/D _t	=	Total derivative
e	=	Base of natural logarithm
f	=	Frequency
FM	=	Frequency Modulation
GR	=	General Radio, Inc.
i	=	$\sqrt{-1}$
j	=	Radial mode order
J _m	=	M _{th} order Bessel function, first kind
k	=	Free space wave number
k	=	Arbitrary positive or negative integer
K	=	Mass reactance correction dependent on airflow Mach number
L	=	Sound level
L	=	Inlet treatment axial length
L _w	=	Blade passing frequency PWL
ℓ	=	Acoustic treatment cavity depth
LRC	=	Langley Research Center
L/D	=	Treated length over duct diameter

LIST OF SYMBOLS (Continued)

LE	=	Leading Edge
m	=	Spinning mode order
M, M ₀	=	Uniform mean flow Mach number
MPT	=	Multiple Pure Tone
M _{th}	=	One-dimensional, averages throat Mach number
n	=	Boundary condition index
n	=	Arbitrary integer
\vec{n}	=	Unit vector normal to wall
N _F	=	Compressor stage rotational speed, uncorrected
N _{FC}	=	Compressor stage rotational speed, corrected to Standard Day Conditions
OAPWL	=	Overall Sound Power Level calculated by summation of power levels at each 1/3 octave band
OASPL	=	Overall Sound Pressure Level calculated by summation of sound pressure levels at each 1/3 octave band
p	=	Acoustic pressure
P _S	=	Static pressure
P _T	=	Total pressure
P _{T0}	=	Ambient total pressure
PNL	=	Perceived Noise Level; a calculated, annoyance weighted sound level
PNdB	=	Perceived Noise Decibels
PWL	=	Sound Power Level, Re: 10 ⁻¹³ watts
r	=	Radial variable
R(r)	=	Radial solution to wave equation
R _{xx}	=	Autocorrelation function
R	=	Acoustic resistance
R/ρc	=	Resistance ratio
RMS	=	Root Mean Square
SAE	=	Society of Automotive Engineers
STC	=	Steamtube Curvature
SPL	=	Sound Pressure Level; Re: 0.0002 dynes/cm ²

LIST OF SYMBOLS (Continued)

t	=	Time
t	=	Faceplate thickness
T	=	Period for autocorrelation function
T_0	=	Minimum time delay required for the auto correlation function to reach zero
u	=	Axial turbulence velocity component
\overline{u}	=	RMS value of axial turbulence velocity
\overline{U}	=	Axial mean velocity of the airstream
v	=	Circumferential turbulence velocity component
\overline{v}	=	RMS value of circumferential turbulence velocity
V	=	Number of vanes
W	=	Weight flow
W_{FS}	=	Weight flow of fuel scale vehicle
W_M	=	Weight flow of scale model
$W\sqrt{\theta/\delta}$	=	Fan airflow, corrected to standard day conditions
x	=	Arbitrary variable in autocorrelation function
X	=	Acoustic reactance
$X/\rho c$	=	Reactance ratio
z	=	Axial variable
$Z(z)$	=	Axial solution to wave equation
Z	=	Acoustic impedance
$Z/\rho c$	=	Acoustic impedance ratio
α	=	Correction factor compensating for losses through vehicle struts
α	=	Characteristic parameter
β	=	Wall admittance ratio
δ	=	Pressure ratio relative to standard day ambient pressure
δ	=	0.85 Kd, empirical mass reactance end correction
η	=	Measured inlet recovery
θ	=	Temperature ratio relative to standard day ambient temperature
θ	=	Circumferential angle
$\theta(\theta)$	=	Circumferential solution to wave equation

LIST OF SYMBOLS (Concluded)

κ	=	Axial propagation constant
λ	=	Wavelength of sound
ρ	=	Airstream static density
ρv	=	Mass flux
ρc	=	Characteristic impedance of air
σ	=	Faceplate porosity
τ	=	Integration variable (time) in autocorrelation function
∇	=	Gradient operator

DEFINITIONS

Cylindrical Inlet	-	An inlet of uniform inside diameter with a conventional bellmouth, no centerbody.
High Subsonic Mach Inlet	-	An inlet of varying inside diameter, having the minimum area, or throat, immediately aft of the bellmouth, thence diffusing into the same diameter at the discharge plane as the cylindrical inlet.
Accelerating Inlet	-	A high subsonic Mach inlet without acoustic treatment.
Hybrid Inlet	-	A high subsonic Mach inlet with acoustic treatment.
Standard Day	-	15° C (59° F) temperature and 70% relative humidity.

ANALYTICAL AND EXPERIMENTAL STUDIES OF ACOUSTIC PERFORMANCE
OF SEGMENTED LINERS IN A COMPRESSOR INLET

R.E. Motsinger, R.E. Kraft, J.E. Paas, and B.M. Gahn

General Electric Company

SECTION 1.0

SUMMARY

This report presents the results of an analytical and experimental investigation of acoustic suppression expected versus that actually achieved with multi-segmented treatment on the inlet of a compressor stage simulating the fan of a turbofan engine. The analytical prediction for the multi-segmented treatment from the analysis developed by W. Zormuski (Reference 1) was found to provide the correct order of magnitude of suppression and was generally within 50% of that determined experimentally. In order to improve the correlation, further refinements are required in: (1) measurement of the source characteristics in terms of its complex acoustic pressure and constituent modal amplitude and phase; (2) the algorithm used in the programming of the analysis to find the eigenvalues of the treated duct; (3) the determination of the acoustic impedance of the treatment under conditions equivalent to those imposed by aircraft engine ducts. While this work was exploratory in nature, particularly in regard to the measurement of the modal characteristics of the source, the results suggest that work to develop this approach further will lead to a useful and reliable prediction method.

In addition, this report presents the results of an experimental study of the acoustic suppression that can be achieved by means of the effect of high-subsonic flow Mach number in the inlet, per se, and of the amount that this effect can be augmented by means of acoustic treatment. The data show that the suppression due to high subsonic Mach number flow effects become significant above an average throat Mach number of 0.65 to 0.7 and that 20 PNdB can be achieved with an average throat Mach number in the range of 0.80 to 0.85; further, the data show that an inlet with a length-to-diameter ratio of 1.42 operated with pressure recovery of 0.99 or greater over this throat Mach number range. It showed that the effects of flow and of treatment are not additive, but that the acoustic treatment was as effective in the high Mach inlet as in the cylindrical inlet.

Finally, data are given for the measured turbulence in the inlet, including the axial and circumferential turbulence intensities and the axial integral length scale. These data are presented for the inlets as tested for the inlet suppression studies and for the inlets after an inlet screen was added to smooth the turbulence. Data with and without the inlet screen are presented, showing that the screen reduced the turbulence intensities and that the BPF noise was reduced as a consequence.



SECTION 2.0

INTRODUCTION

Reduction of noise radiated from the inlets of turbofan engines without resort to the use of acoustically treated splitters is essential for meeting Federal regulations on aircraft flyover noise while avoiding performance penalties and operational difficulties, or even potentially hazardous conditions, which could arise from ice formation on such splitters. As regulated noise limits are progressively lowered in the years to come, the continued need for improvement in suppression techniques will require the use of more and more sophisticated design approaches.

Two such approaches have been investigated in the present study: one is based on the multisegmented (or multi-phased) treatment concept evolved by Zorumski⁽¹⁾, and the other is based on the high-subsonic velocity flow effects upon acoustic propagation (attenuation) that has been experimentally observed for untreated inlets of variable cross-sectional area*.

The multi-phased treatment concept consists of incorporating two or more acoustic treatments of different impedances on the duct wall so that at the interfaces between any two treatment panels, reflection and redistribution of acoustic energy into higher order modes occur, thereby causing the treatment to be more effective in absorbing the noise. Zorumski's analysis⁽¹⁾ provides the understanding and permits the analytical prediction of these effects.

The effect of high-subsonic velocity flow on duct propagation is not as well understood. The surprising aspect is that the suppression becomes significant well before sonic velocities are reached in the inlet, but this is already known from prior tests*. The present study, therefore, was concerned with achieving this effect with high performance and with determining the benefit of incorporating treatment so as to include the combined benefits of flow and (single or multi-phased) treatment in the so-called "hybrid" concept. Because the high-subsonic velocities needed to achieve acoustic suppression are too large to present to the compressor rotor, relative to current design practice limits, the inlet is contoured so as to have the smallest flow area (throat) immediately downstream of the inlet lip, then the area is increased so that the airflow is diffused and the velocity is slowed to values that are within acceptable limits. The possible effect of this diffusion process upon ingested aerodynamic turbulence cell-size and intensity-levels and, thence, the effect of this (possibly amplified) turbulence on the rotor-generated noise^(2,3,4) led to some concern with regard to whether any suppression benefit from the high-subsonic flow effects might be reduced or totally lost as a result of increased source noise level. Therefore, this aspect was also studied experimentally in this program.

*Unpublished data.

Use of trade names or names of manufacturers in this report does not constitute an official endorsement of such products or manufacturers, either expressed or implied, by the National Aeronautics and Space Administration.

SECTION 3.0

OBJECTIVES

The general objectives of this report are: to show the correlation obtained between predicted and measured acoustic attenuation in a compressor inlet duct with multisectional acoustic treatment; to show the effect of high-subsonic-velocity flow on the acoustic and aerodynamic performance of an inlet with and without such treatment; and, to document the inlet turbulence levels and associated farfield noise from the compressor when tested in the NASA-LRC anechoic chamber with the conventional and high-subsonic Mach inlets, with and without an inlet screen for smoothing the turbulence. More specifically:

1. The primary purpose of this report is to compare the suppression predicted for specified inlet treatment configurations from the analysis developed at NASA-LRC by Zorumski⁽¹⁾ and implemented in the "Acoustic Theory of Axisymmetric Multisectioned Ducts" computer program, ACTAMD, with the suppression achieved by these configurations on an experimental compressor and, to make recommendations for any improvements in the analysis identified as a result of this comparison.
2. A secondary objective is to provide information on the experimentally determined aerodynamic performance and acoustic suppression for an "accelerating" inlet with and without multisectional treatment, showing the effect of high subsonic velocity flow, up to 0.83 average throat Mach number, on the suppression achieved.
3. The final objective is to provide information on the axial and circumferential turbulence intensity levels and on the integral length scale in the axial direction of the turbulent cells, for both the conventional (cylindrical) and the accelerating inlet on the compressor as installed in the NASA-LRC Anechoic Chamber also, to document the measured farfield noise levels radiated from the compressor inlet for the same test conditions, without instrumentation rakes in the inlet; finally, to show the effect of an inlet screen on both turbulence and noise for each inlet type.

SECTION 4.0

THEORETICAL CONSIDERATIONS

The basis for the design of the acoustic treatment, a discussion of the wavefield theory, and the mathematical model of the test vehicle used for the analytical program are presented in this section.

4.1 LINER DESIGN

Since the primary purpose of this study was to establish the experimental verification of the analytical prediction of suppression by the acoustic field theory outlined by Zorumski(1), the acoustic treatment designs evolved for the experiment included six different basic panels. These six allow permutations of three at a time to provide 120 different possible treatment configurations. In this way the segmentation effects postulated by Lansing and Zorumski in Reference (5) and by Zorumski in Reference (6) as having possible beneficial effect could be investigated by selection of favorable combinations.

The criteria used for evolving these particular panel design choices consisted of the following:

- o One of the panels should be designed for the values of reactance and resistance expected to be near optimum for the $m=-7$ Tyler-Sofrin rotor-stator interaction(7) mode expected for the vehicle with its 19 rotor blades and 26 stators. A baseline test of this panel, at the same treated length-to-diameter ratio as used for the multi-segmented configurations, should be included as a reference for evaluating the improvement achieved by multi-segmenting or "multi-phasing".
- o To obtain the beneficial effect of impedance mismatch at the interfaces between adjacent segmented panels, the specific reactance of the panels, $X/\rho c$, must change abruptly in sign(6) (from negative to positive or vice-versa). Desirable values of the specific reactance at the design frequency should be -1, 0, and a high positive value; also, in the adjacent 1/3 octave frequency bands on either side of the design frequency two of the panels should have reactances of opposite sign so that the criteria of Lansing and Zorumski(5,6) could be met at more than one frequency. Three panel depths were selected to meet these criteria (see Section 5.1.4).

To include the possible differences in effects between dissipative and reflective liners(5), there should be two sets of panels of different resistances: one set with a nominal 10% porosity in the faceplate and the other with 25%. The 10% porosity is estimated to provide between 1.0 and 1.5pc resistance, typical of dissipative panels; and, the 25%, between 0.4 and 0.6pc, approaching that of reflective panels.

Six panels, therefore, were designed to obtain a range of variations on both reactance and resistance which, in general, met the criteria which prior studies showed were desirable in order to achieve enhanced suppression as a result of the use of multisectional treatment.

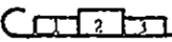
The computer program of Zorumski's analysis, ACTAMD, was used to screen from the possible 135 multisegment permutations* a total of 15 segmented configurations for test in the experimental program (see Section 5.1.4 and Table III). A hard walled baseline case and two different lengths of uniform treatment were also tested. For this study, the principal frequency considered was 6300 Hz (which occurs at a test-vehicle rpm that yields subsonic absolute tip Mach number, see Section 5.1.2), but since sensitivity to bandwidth may also be of concern, the adjacent 1/3 octave midpoint frequencies of 5000 and 8000 Hz were also considered in some cases.

At this time, the source characteristics of the compressor and inlet duct had not yet been determined, so the screening analysis was done assuming that the blade passing frequency tone noise was dominated by rotor-stator noise; accordingly, the Tyler-Sofrin prediction for rotor-stator interaction (seventh-order) spinning mode number was assumed. Additional assumptions for this study included: 1) the first three radial modes (which are all cut on) were of equal amplitude and zero relative phase at the entrance to the treated section (input into the softwall); 2) the resistances of the 10% and 25% porosity faceplate were 1.5 and 0.5pc, respectively; 3) the airflow was of uniform velocity, 0.4 Mach number, throughout the duct cross-section; 4) the boundary condition at the wall was continuity of particle displacement. The suppressions predicted on this basis for 49 configurations of the 6 treatment panels, including 6 single phase and 43 multisegment combinations, are summarized in Table I; those configurations selected for test are also identified.

Calculated suppressions for a given duct configuration are strongly dependent upon the source characteristics (relative amplitudes and phases of the excited modes), so that a truly valid test of the theory can only be made if the source is well defined. For this purpose, a "Mode-probe" (see Section 5.2.1) was used to determine the spinning mode order present at a particular radius of the test vehicle; this measured information was used in the ACTAMD program to predict suppressions for selected configurations as presented and discussed in Section 6.2.

*Permutations of (A,B,C,D,E,F) taken 3 at a time, $\frac{6!}{3!} = 120$
permutations of A, A plus one of B,C,D,E,F = 15; Total 135.

Table I. PredictedSuppressions.

Panel Number			Termination  Source			Selected for Test*	
			Predicted Insertion Loss, ΔPWL, dB			Cylindrical Inlet	High Mach Inlet
1	2	3	5000 Hz	6300 Hz	8000 Hz		
H	H	H	0.0	0.0	0.0	✓ 1,16,19	✓ 21
A	A	A	13.0	7.1	5.2	✓ 2	✓ 22
B	B	B	12.6	6.9	4.7		
C	C	C	10.3	3.8	5.2		
D	D	D	5.4	4.2	-		
E	E	E	5.6	7.6	2.1		
F	F	F	4.8	1.4	2.9		
C	B	A	12.8	6.5	5.4	✓ 4	
C	A	B	13.6	6.9	5.0	✓ 8	✓ 23
A	C	B	12.0	6.3	4.7		
B	C	A	12.3	6.4	4.9		
A	B	C	12.3	8.3	5.4	✓ 3	
B	A	C	14.2	9.3	5.2	✓ 7	
E	B	A	-	7.0	-		
B	E	A	-	7.3	-		
E	A	B	-	7.3	-		
A	E	B	-	7.4	-		
B	A	E	10.7	7.7	-		
A	B	E	10.3	7.4	-		
C	E	A	-	6.8	-		
E	C	A	-	6.6	-		
C	A	E	-	7.3	-	✓ 20	✓ 24
A	C	E	-	6.3	-		
E	A	C	-	9.3	-	✓ 14	
A	E	C	-	8.5	-	✓ 15	
E	C	B	-	6.0	-		
C	E	B	-	6.7	-		
E	B	C	-	8.2	-		
B	E	C	-	8.3	-		
C	B	E	-	6.7	-		
B	C	E	-	6.0	-		
F	E	D	6.1	6.1	-	✓ 6	
E	F	D	6.6	5.6	-		
F	D	E	6.1	7.1	-		
D	F	E	6.4	5.4	-		
E	D	F	7.0	-	-		
D	E	F	5.8	9.1	-	✓ 5	
E	A	D	-	6.7	-		
B	A	D	11.0	6.6	-		
A	E	D	-	7.1	-		
A	B	D	10.9	6.7	-		
E	E	C	-	8.3	-		
E	E	F	-	7.9	-		
E	C	F	-	4.9	-		
B	A	F	11.3	-	-	✓ 10	
A	B	F	10.0	-	-	✓ 9	
A	B	A	13.2	-	-	✓ 18	
A	A	C	13.6	-	-	✓ 13	
A	A	B	13.1	-	-	✓ 17	
A	A	F	10.8	-	-	✓ 11	
A	A	H	-	-	-	✓ 12	

*Numbers denote the configuration identification as defined in Tables III and IV.

4.2 WAVE FIELD THEORY

The acoustic wave propagation in a duct with mean flow is described by a second order partial differential equation known as the convected acoustic wave equation⁽¹⁾,

$$\nabla^2 p = \frac{D^2 p}{Dt^2} \quad (4.1.2-1)$$

and associated wall boundary conditions

$$\nabla p \cdot \vec{n} = i \left(1 - M_o \frac{\kappa}{k}\right)^n \beta k p \quad (4.1.2-2)$$

where

- p = acoustic pressure
- t = time
- M_o = mean flow Mach number
- κ = axial propagation constant
- \vec{n} = unit vector normal to wall
- i = $\sqrt{-1}$
- k = free space wave number
- β = wall admittance
- n = 1, particle velocity continuity, =2, particle displacement continuity
- ∇ = gradient operator

$$\frac{D}{Dt} = \frac{\partial}{\partial t} + M_o \cdot \frac{\partial}{\partial z}$$

z = axial length variable

It is assumed that the mean flow is uniform across and along the duct. If the duct geometry possesses sufficient symmetry, the method of separation of variables can be applied to Equations (4.1.2-1) and (4.1.2-2) by assuming a solution of the form

$$p(r, \theta, Z) = R(r) \Theta(\theta) Z(z) \quad (4.1.2-3)$$

this leads to a set of ordinary differential equations and boundary conditions.

In the case of the cylindrical duct (no centerbody), the characteristic solution in the axial direction is of the form,

$$Z(z) = e^{ikz} \quad (4.1.2-4)$$

the circumferential solution is of the form,

$$\Theta(\theta) = e^{im\theta} \quad (4.1.2-5)$$

and the solution in the radial direction involves Bessel functions, such that

$$R(r) = J_m(\alpha r) \quad (4.1.2-6)$$

where

θ = circumferential variable

m = spinning mode order

J_m = m th order Bessel function, first kind

r = radial variable

α = characteristic parameter

Following the classical method of solution, it can be shown that application of the boundary conditions in the radial direction leads to a discrete set of characteristic functions, known as eigenfunctions, with associated eigenvalues. The eigenfunctions form a complete set of functions⁽⁸⁾ in the Fourier series sense, from which general solutions can be constructed by series expansions.

This modal analysis approach forms the basis for the exact solution for the wave field in a uniform, segmented, axisymmetric duct, as described by Zorumski⁽¹⁾. To complete the solution, it is necessary to provide a description of the noise source in terms of modal source characteristics at some plane (or planes) of the duct. The source enters as a non-homogeneity in the differential equation at the source planes.

The solutions in different segments of the duct at the planes of intersection between segments are coupled by means of equations of continuity of acoustic pressure and the axial component of acoustic velocity across the interfaces. These relationships can be cast into the form of transfer matrix equations with the modal amplitudes of the solution at duct segment end planes as the unknown quantities. These transfer matrix equations are then stacked into a large system matrix equation, which can be solved for the modal amplitude vector by standard methods for systems of linear equations.

The solution is exact in the sense that the only approximation involved is that due to the convergence of the series expansions, in a Fourier series sense. The errors can be reduced to any desired value by including a sufficient number of modes in the series expansion. When the modal solution in each duct section is determined, the energy flux and thus the overall suppression can be calculated from the acoustic intensity expression.

The wave field solution in terms of component modes provides a number of advantages to purely numerical solutions such as finite differences or finite elements in that it allows a complete description of the propagation phenomena in terms of modal redistribution, reflection, and attenuation. The interpretations afforded by the modal description provide critical insights to propagation effects which influence the performance of liner designs.

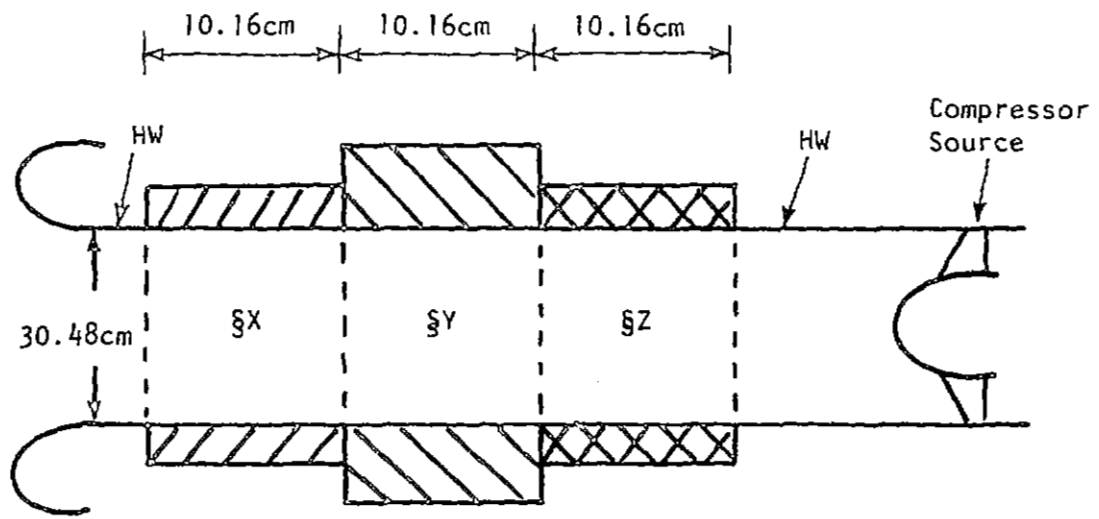
4.3 MATHEMATICAL MODEL OF TEST VEHICLE

The mathematical model of the test vehicle is based on the ACTAMD analytical program input requirements for a cylindrical, multi-segmented inlet with mean flow. The primary input to the program consists of duct geometry, treatment definition, source modal characteristics, mean flow Mach number, and spinning mode order. The frequency information is included by nondimensionalizing all lengths in the program by the inverse of the wavenumber.

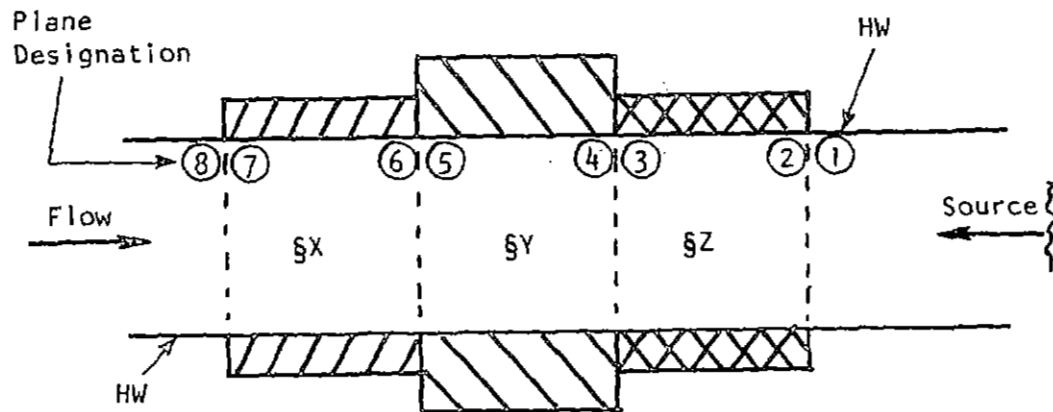
Figure 1 shows schematics of the actual inlet geometry and the mathematical model input to ACTAMD. The inlet is modeled as semi-infinite length duct, such that acoustic reflections from the bellmouth inlet (duct termination) are ignored. The mean flow is assumed to be uniform across and along the duct.

The source plane is taken to be the hardwall plane designated as Plane 1 in Figure 1 adjacent to the entrance to the first treatment section. The mode weightings as determined by the in-duct modal measurements were entered at this plane for each spinning mode order, assuming all energy to occur in the forward propagating wave. The overall PWL suppression was calculated by comparing the net flux at Planes 1 and 8, under the assumption that very little energy was reflected at Plane 1.

The treatment definition is based on the analytical impedance models presented in Section 5.1.4. It is assumed that the effects of boundary layers, both on the wave propagation and treatment impedance, can be neglected.



CYLINDRICAL INLET



MATHEMATICAL MODEL

Figure 1. Schematics of Treated Cylindrical Inlet and ACTAMD Mathematical Model.

SECTION 5.0

EXPERIMENT

The experimental facility, test hardware, data acquisition and reduction procedures, and the test program for both acoustic and aerodynamic data are defined in this section.

5.1 EXPERIMENTAL FACILITY AND TEST APPARATUS

5.1.1 Anechoic Chamber

The NASA-LRC, Bldg 1218A, anechoic chamber shown in Figure 2 was used in this test program. The internal dimensions of the chamber are approximately 7.6 x 7.6 x 7.0 m (25 x 25 x 23 ft) between wedge tips. All surfaces of the chamber are covered with fiberglass wedges impregnated with phenol-formaldehyde and enclosed with hardware cloth to increase rigidity. The wedges on the floor are overlaid with a metal grating to allow walking access to the test equipment.

The test vehicle is installed in one corner of the room, as shown in Figure 2, with a small (15°) cant from the adjacent sidewall. The airflow that passes through the test vehicle enters the chamber through an intake stack in the roof, and is exhausted into a discharge plenum, a discharge valve, and an exhaust stack. Back pressure on the test vehicle is controlled by the discharge valve.

The test vehicle is driven by an electric motor coupled to the shaft of the rotor stage; the drive is isolated from the room by the wall of the chamber.

5.1.2 Test Vehicle

The test vehicle was a single-stage transonic compressor 30.5 cm (12 in.) in diameter, consisting of 19 rotor blades and 26 outlet guide vanes with a spacing of 1.02 true rotor pitch chord lengths. There were 5 center-body support struts 2.7 (strut) chord lengths upstream of the rotor. A cross section of the test vehicle as configured for this test is shown in Figure 3.

On the operating line, the pressure ratio of the stage is 1.325 at 100% rpm, and the airflow as a function of percent rpm in the range from 70 to 100% is given in Figure 4. Reference information on absolute rpm, tip speed, and blade passing frequency as a function of percent rpm is given in Table II. The stage was operated on this operating line during the test program.

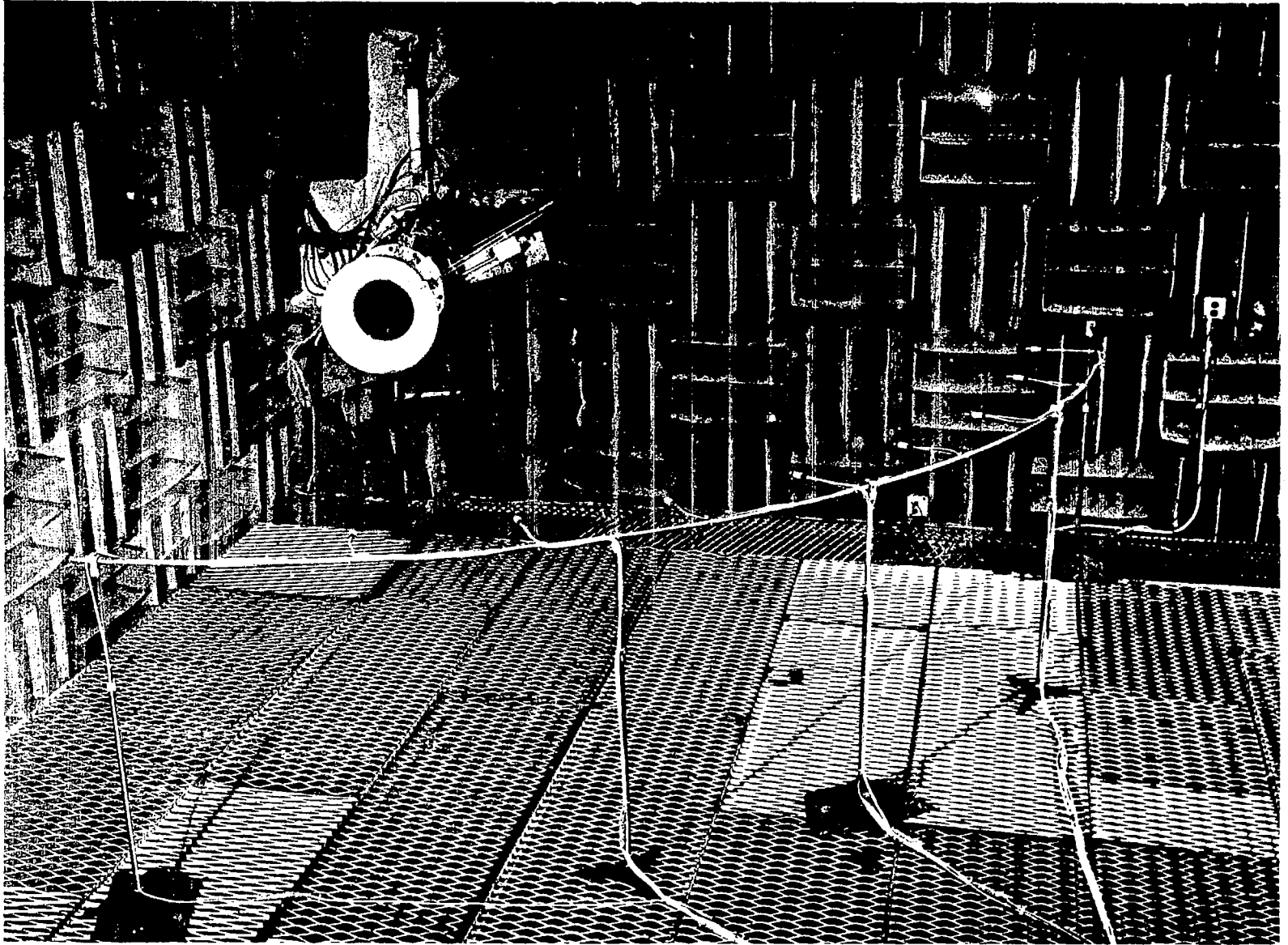


Figure 2. NASA-Langley Research Center Anechoic Chamber.

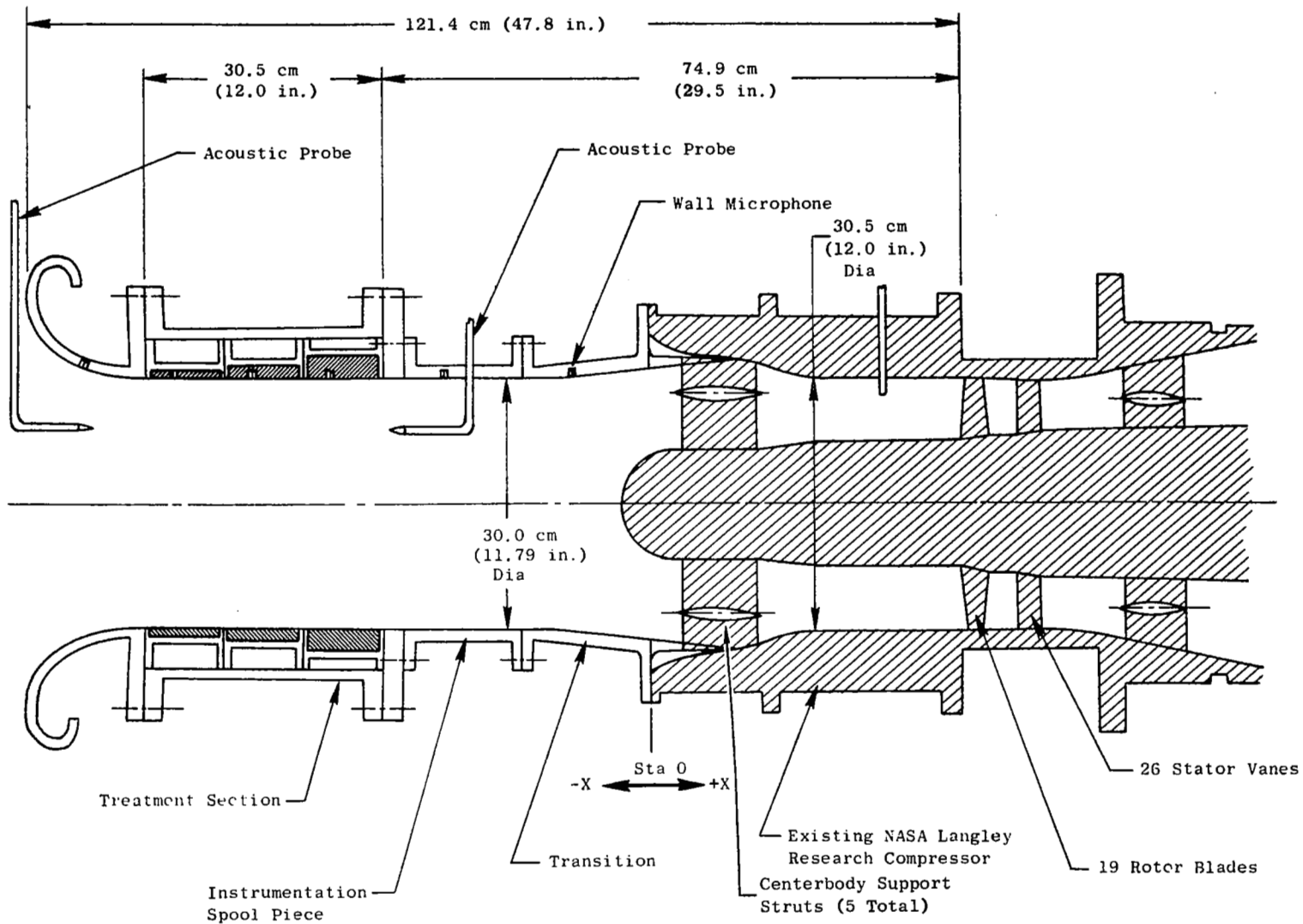


Figure 3. NASA-Langley Research Center Anechoic Chamber Test Vehicle with Treated Inlet.

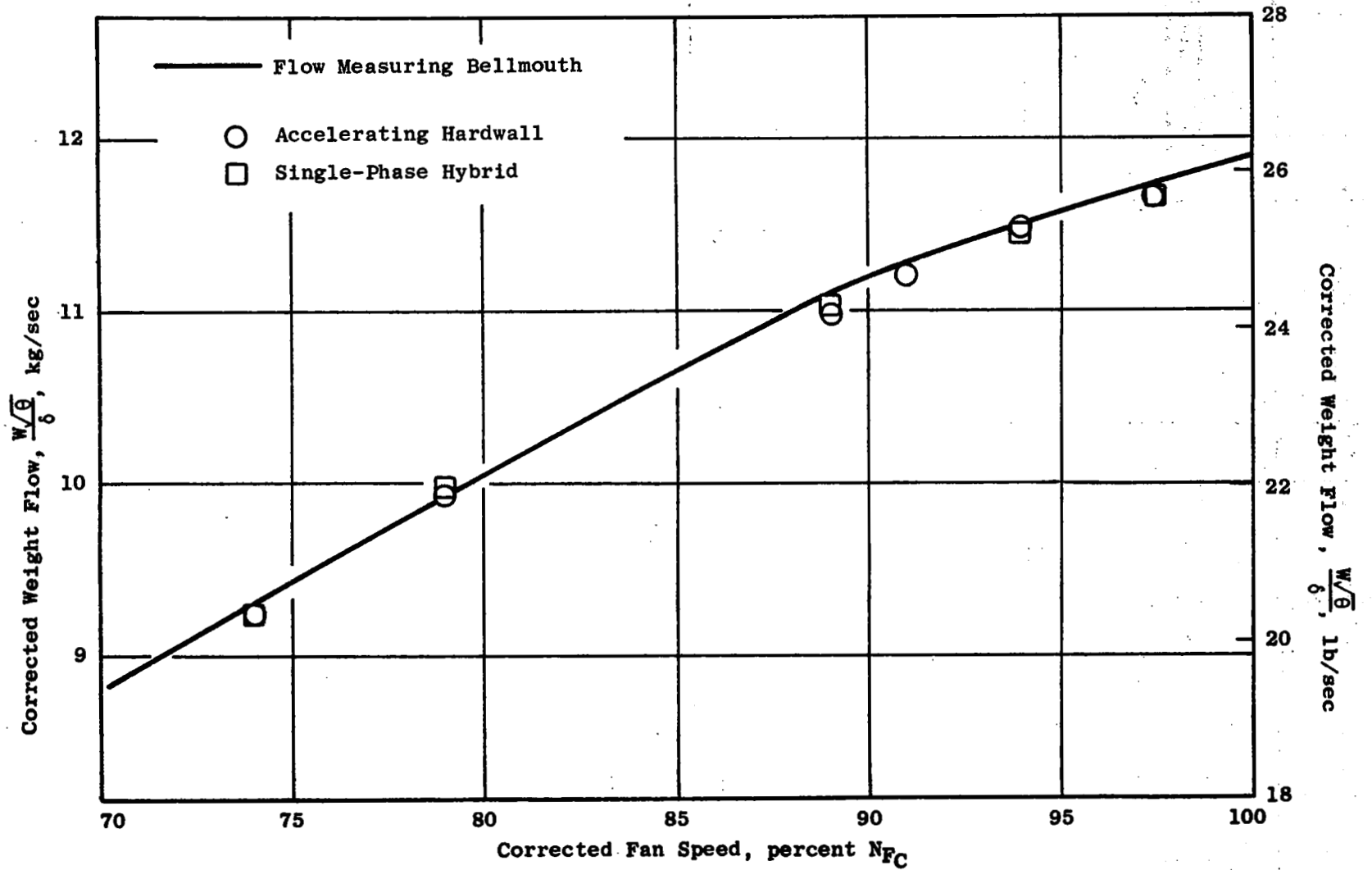


Figure 4. Speed Flow Relationship for High Mach Number Inlet.

Table II. Compressor Stage Reference Information.

Rational Speed		Tip Speed		Absolute Mach No.	Blade Passing Frequency	
Percent of Design rpm	NFC rpm	M/s	(ft/s)		Model	Full Scale**
100	24,847	396.5	(1301)	1.16	7868	1960
97.5	24,226	387	(1268)	1.14	7672	1911
94	23,356	373	(1223)	1.10	7396	1842
91	22,611	361	(1184)	1.06	7160	1783
89*	22,114	353	(1158)	1.04	7003	1744
79	19,629	313	(1028)	0.92	6216	1548
74	18,387	293	(963)	0.86	5822	1450
69	17,144	274	(898)	0.80	5429	1352
44	10,864	173	(569)	0.51	3440	857

* Design point for the High Mach Inlet.

** See Section 5.4.

5.1.3 Inlet Hardware

Two inlets were tested: a cylindrical and a high-Mach-number inlet. Both were designed to accommodate three separate replaceable liner segments, either hardwall or acoustically treated to achieve a treated length-to-diameter ratio, L/D, of 1.0. The two designs shown in Figure 5 illustrate the manner in which this was done.

Each inlet had a bellmouth lip: a standard-type, large lip was used with the cylindrical inlet; an "aero/acoustic" lip was used with the high Mach number inlet. The aero/acoustic lip was designed to provide inlet flow characteristics representative of a flight lip in terms of the pressure distribution aft of the peak wall-Mach-number location. The treatment sections for both inlets were one fan diameter in length and were located the same distance from the rotor.

The high Mach number inlet was designed for a one-dimensional throat Mach number of 0.72 at 89% rpm stage speed. This average throat Mach number is about the highest practical level for CTOL aircraft engine inlets without variable geometry. Nevertheless, the design is such that the inlet will operate without flow separation up through an average throat Mach number of 0.83, permitting operation of the compressor stage up to 97% rpm. The average throat Mach number over the range of rpm from 70% to 97% is shown in Figure 6. This design was based on streamtube curvature (STC)⁽⁹⁾ flow analysis and Stratford-Beaver boundary layer analysis⁽⁹⁾ programs which were employed to evaluate boundary layer growth and stability. The L/D of the inlet was 1.42 (to the simulated fan face) and the diffuser area ratio was 1.46.

At the 89% rpm design point, the calculated flow Mach number at the wall along the length of the inlet is shown in Figure 7. This shows that at the throat, where the average Mach number is 0.72, the value at the wall is close to sonic, being about 0.97; aft of the throat, the flow is diffused such that in the region which includes acoustic treatment, the wall Mach number is a maximum of 0.68 and decreases to 0.42 at the downstream end. Note that the inside diameter of the high Mach inlet at the downstream end of the diffuser is identical with that of the cylindrical inlet.

Inlet turbulence, being of concern with regard to its effect on noise generation, was measured as described in Section 5.2.2 with and without a screen over each of the inlets. The screen assembly was installed as shown in Figure 8. The screen, of 20 x 20 mesh and 51.8% porosity, was supported by thin rods (visible in the figure) built according to the dimensions shown in Figure 9.

5.1.4 Acoustic Treatment Panels

Six softwall acoustic treatment panels, designed for this test on the basis described in Section 4.1, consisted of the combination of three cavity depths and two faceplate porosities; the basic construction of the

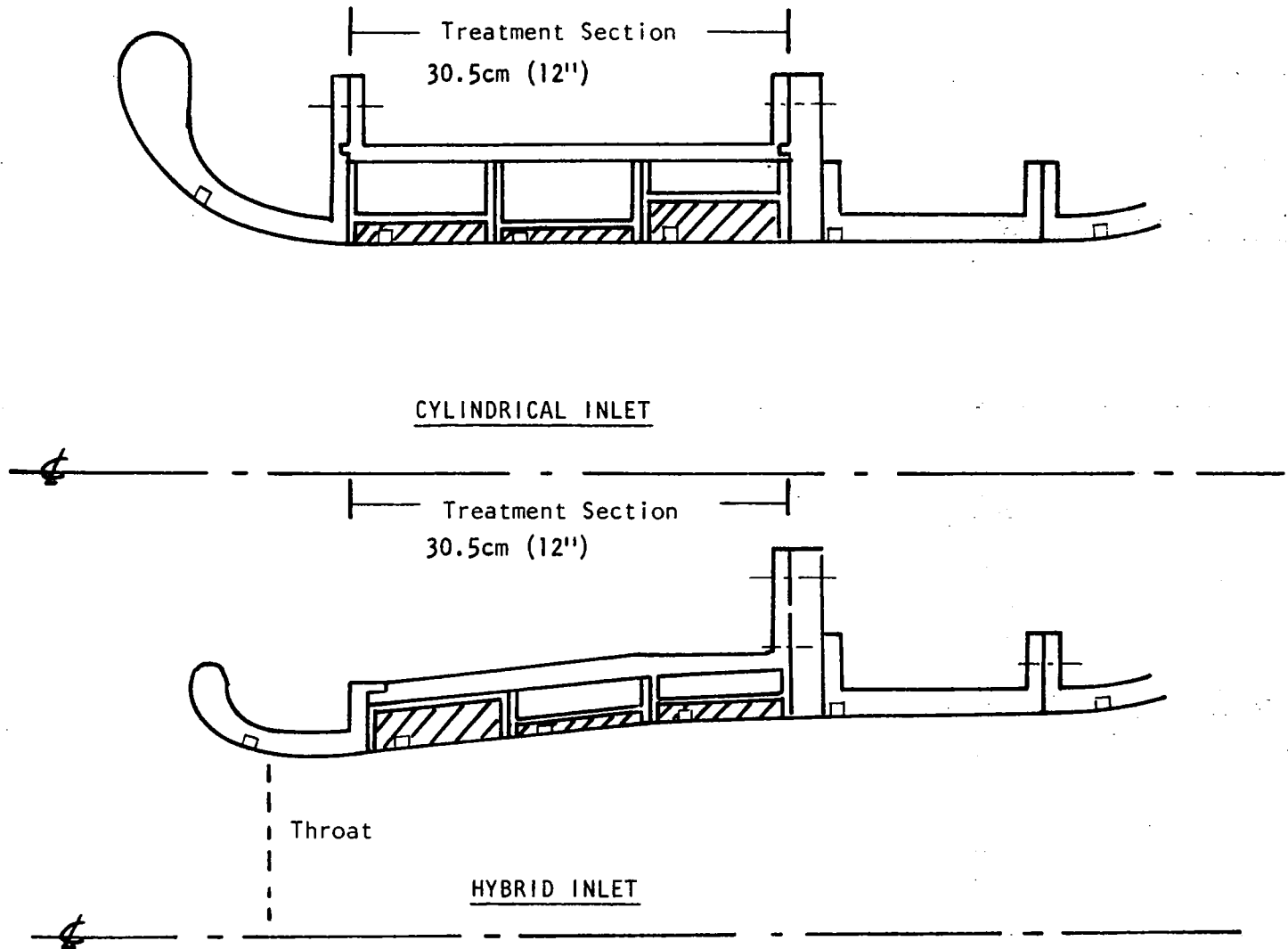


Figure 5. Inlet Designs with Replaceable Panels.

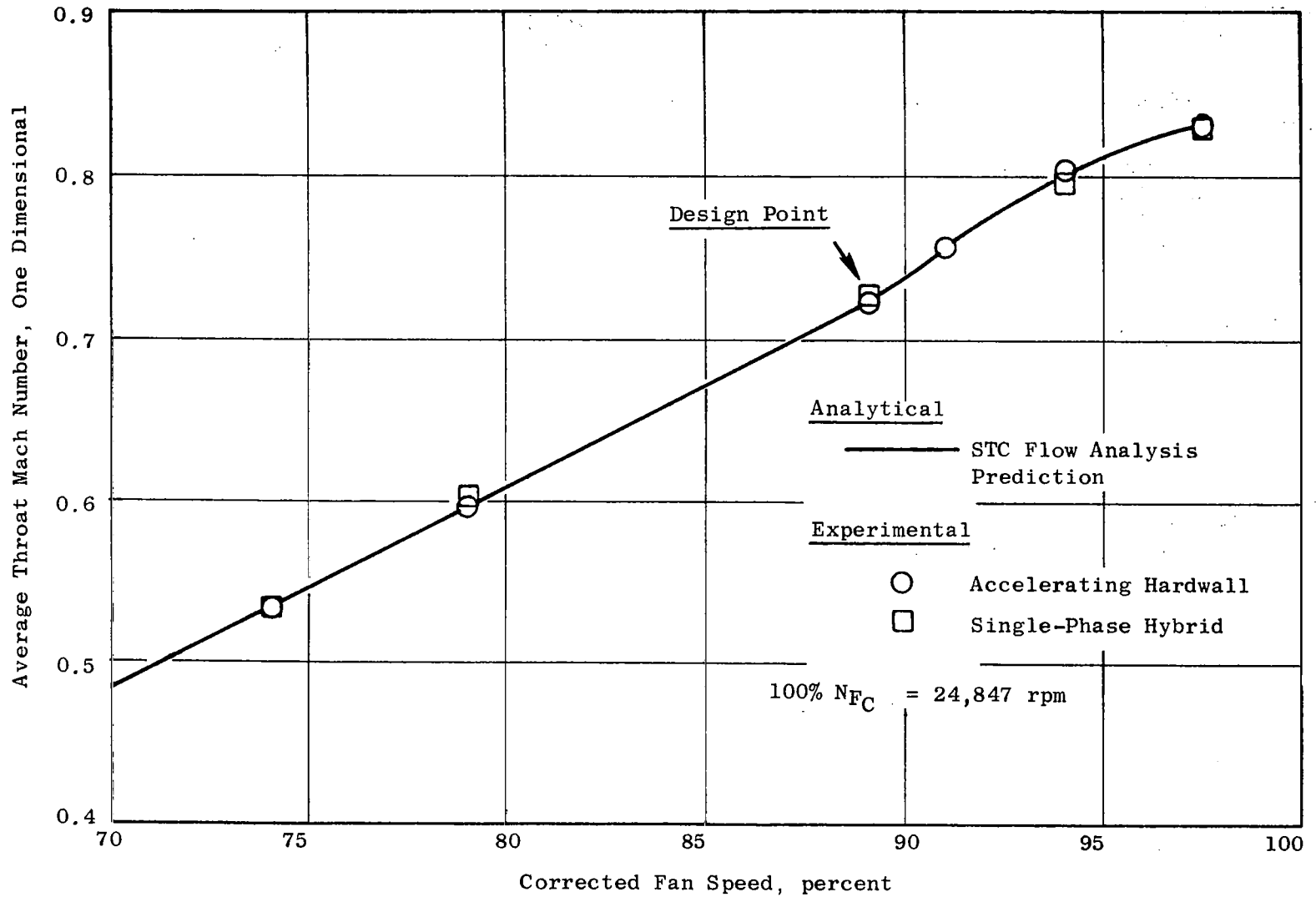


Figure 6. Throat Mach Number/Fan Speed Relationship for High Mach Number Inlet.

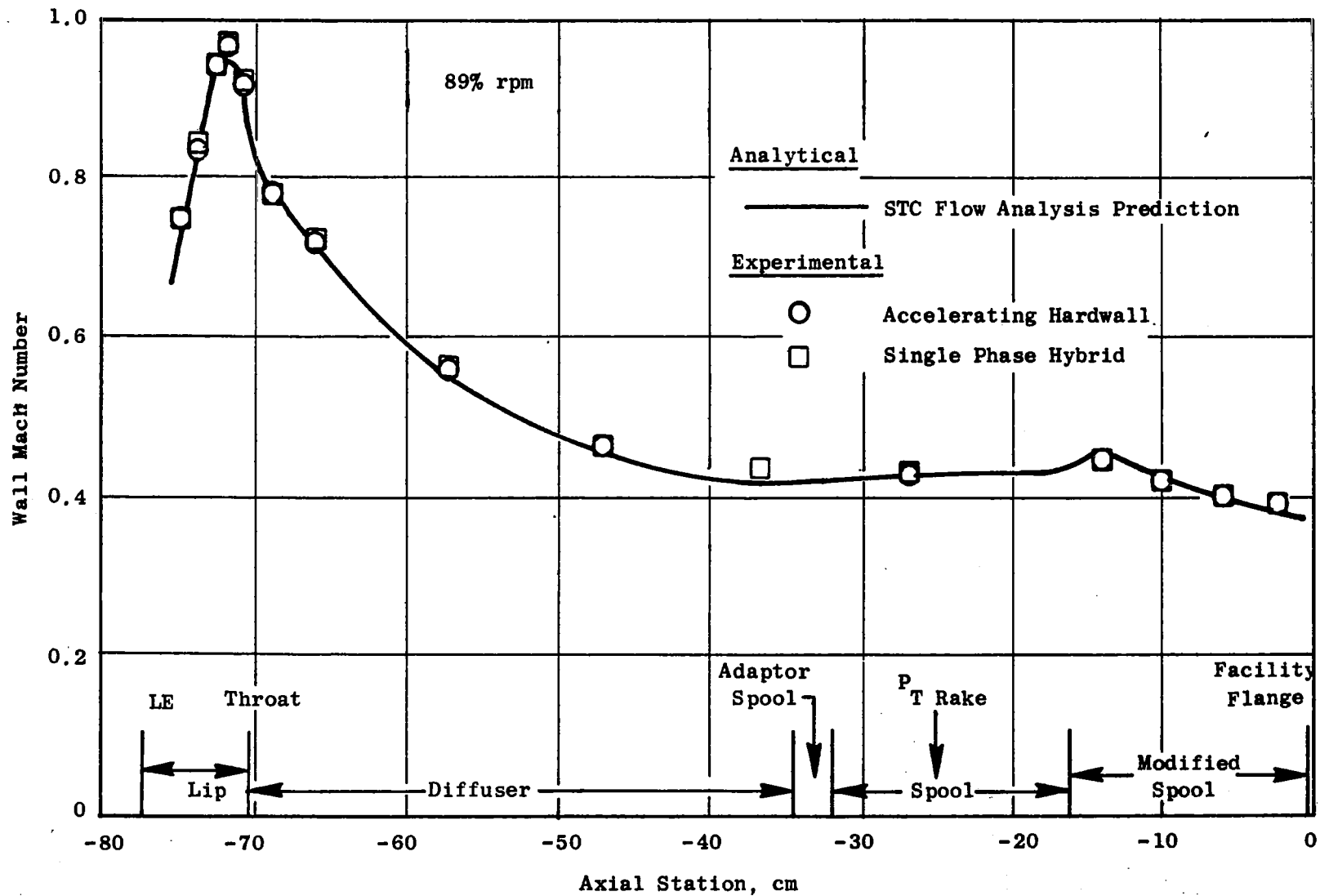


Figure 7. Wall Mach Number Distribution at Design Speed for High Mach Number Inlet.

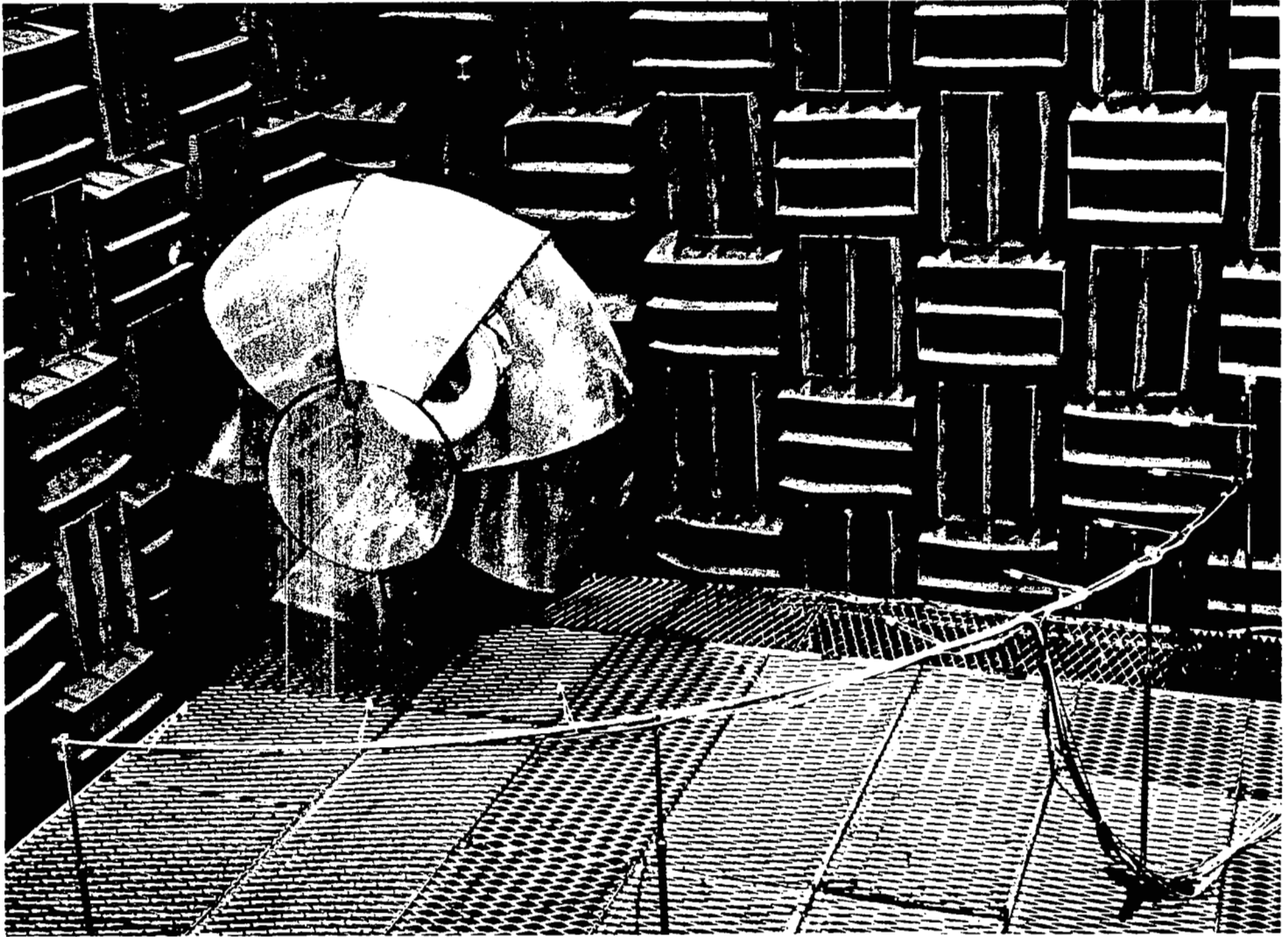


Figure 8. Inlet Turbulence Screen Installed on Test Vehicle.

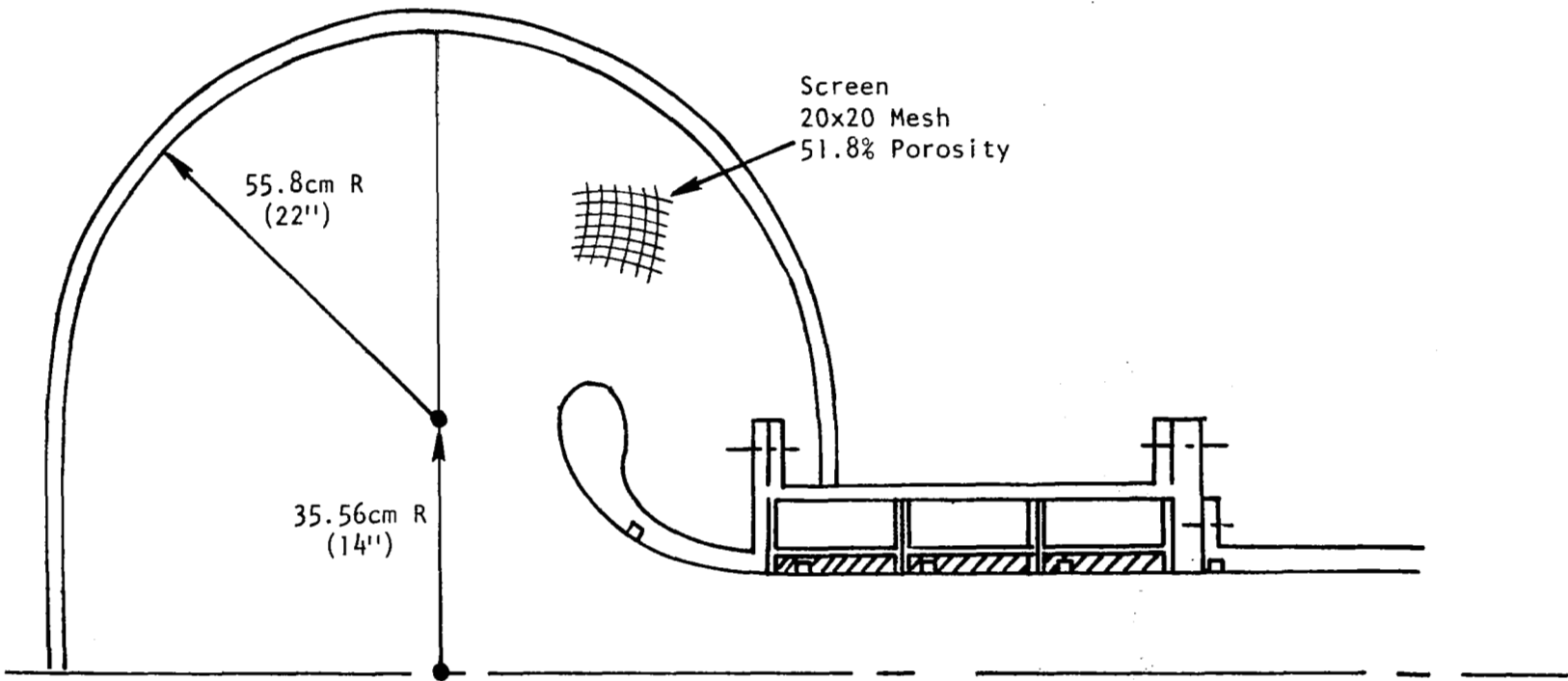


Figure 9. Inlet Turbulence Screen Dimensions.

panels consisted of a solid metal backplate, an air cavity (maintained by a metal honeycomb of the specified thickness), and a perforated faceplate. Hardwall panels (solid metal faceplate) were used to establish the baseline, unsuppressed source levels. Two representative softwall and one hardwall panel are shown in Figure 10.

The panels consisted of the following:

Panel Designation	Faceplate Porosity, %	Cavity Depth, cm (in.)
A	10	0.64 (0.25)
B	10	1.27 (0.50)
C	10	2.54 (1.00)
D	25	0.64 (0.25)
E	25	1.27 (0.50)
F	25	2.54 (1.00)

For each panel the element length was 10.16 cm (4 in.); the faceplate was 0.04 ± 0.01 cm (0.016 ± 0.004 in.) thick with hole diameter of 0.10 cm (0.04 in.); the cell size of the honeycomb in the cavity was 0.64 to 0.96 cm (0.25 to 0.38 in.).

The 10 percent porosity was chosen to obtain a panel resistance between 1.0 and 1.5 ρc ; the 25 percent porosity, to obtain between 0.4 and 0.6 ρc . The resistance is estimated by the empirical formula given by Rice⁽¹⁰⁾.

$$\frac{R}{\rho c} = \frac{0.3M}{\sigma}$$

where: R = Resistance
M = Uniform mean flow Mach number
 σ = Faceplate porosity
 ρc = Characteristic impedance of air.

The calculated reactance versus frequency for each of the six panels is given in Figure 11. The reactance was calculated by:

$$\frac{X}{\rho c} = \frac{k(t+\delta)}{\sigma} - \cot k\ell$$

where: X = Reactance
k = Free-space wavenumber
t = Faceplate thickness
 δ = 0.85 Kd an empirical end correction to establish the effective thickness of the faceplate

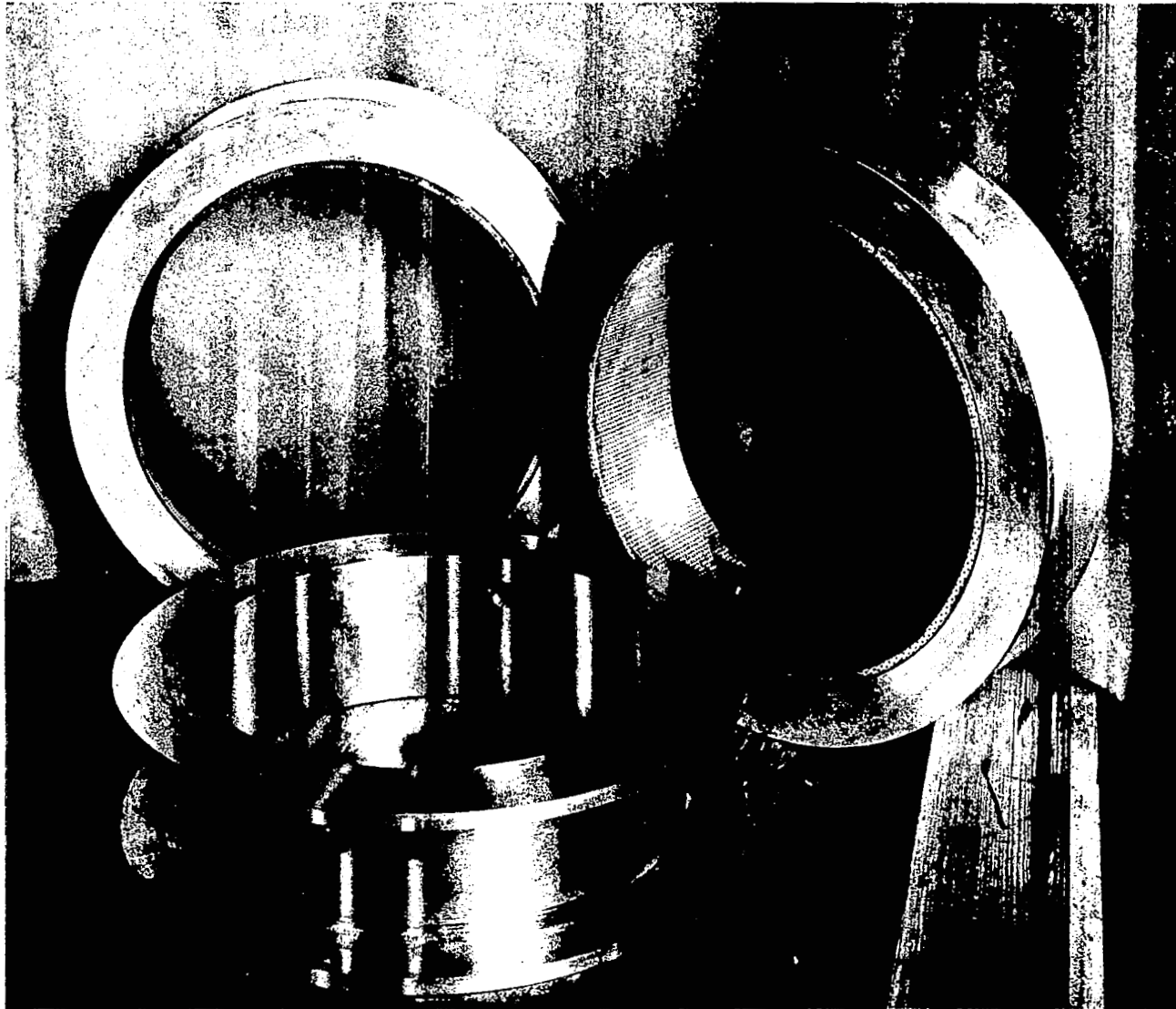


Figure 10. Representative Cylindrical-Inlet Liners.

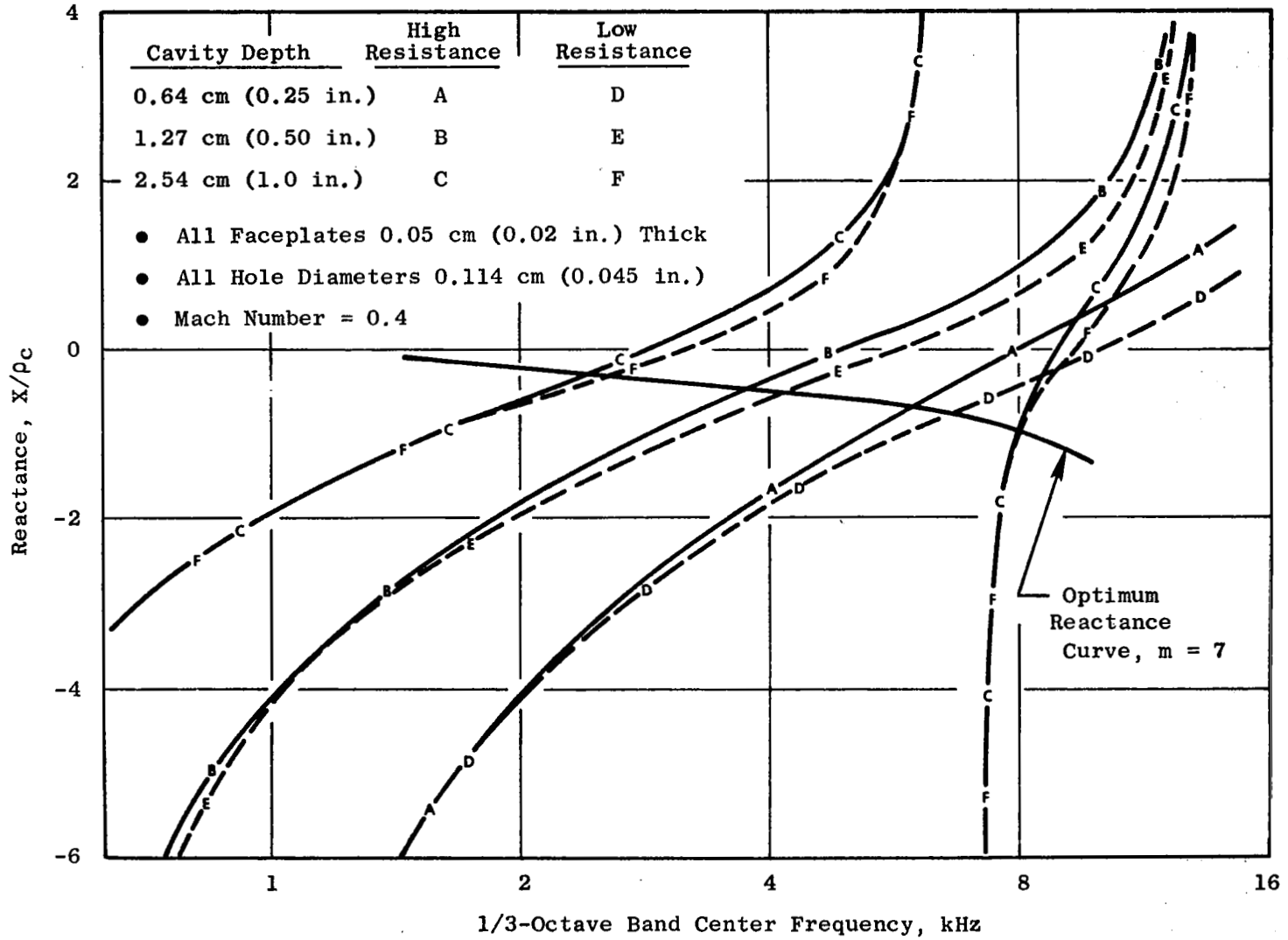


Figure 11. Liner Reactances.

where: d = Hole diameter

K = Correction dependent on airflow Mach number,
given in Figure 12.

The effect of Mach number on the empirical end correction in the reactance model is from Phillips(13).

5.2 INSTRUMENTATION AND DATA ACQUISITION/REDUCTION

5.2.1 Acoustic

Instrumentation for acoustic information included both far-field and in-duct measurements for the determination of sound pressure levels. In addition it included a "mode-probe" for in-duct measurement of the circumferential profile of coherent acoustic pressure amplitude and phase (relative to a stationary reference) for the determination of the circumferential acoustic modes.

Farfield noise measurements were made with nine B&K 4133 microphones of 1.27 cm (1/2 in.) diameter. As shown in Figure 2, they were placed on a circular arc of 3.05 cm (10 ft.) radius centered on the axis of the inlet at the inlet plane, spaced at 10° increments from 0° through 80° relative to the inlet axis, and positioned at the same height as the compressor.

In-duct microphones and traversable acoustic probes with Kulite transducers were installed as shown in Figure 13. The wall-mounted sensors consisted of six B&K 4135 microphones of 0.64 cm (1/4 in.) diameter, flush mounted at the locations indicated by the dashed lines in Figure 13. The traversable acoustic probes were located upstream and downstream of the acoustic treatment as illustrated in Figure 13; an additional probe was used on the High Mach inlet at the upstream location to determine the SPL both at the inlet plane and at the throat plane of the inlet.

A mode probe was developed, designed, and built for application to the test vehicle. The device consists of four probes separated by a 90° angle, which can be rotated circumferentially, and two stationary reference probes. The rotating probes were immersed 5.1 cm (2 inches) from the outer wall. Figure 14 is a photograph of the assembled mode-probe apparatus. The pressure sensing elements were Kulite transducers of 0.318 cm (0.125 in.) diameter mounted in the tips of the probes. Figure 15 is a closeup of an individual probe, indicating the location of the transducer. The signal from each transducer in the system was preamplified, using a low-noise high-gain amplifier, and recorded on tape for subsequent data reduction.

The acoustic data for determination of SPL were recorded on analog tape, using a 14-channel Bell and Howell wideband (Group I) tape recorder, in the FM mode at 152.4 cm/sec (60 in./sec) in order to obtain flat frequency response to 40 kHz. (An exception was the acoustic far-field data taken in

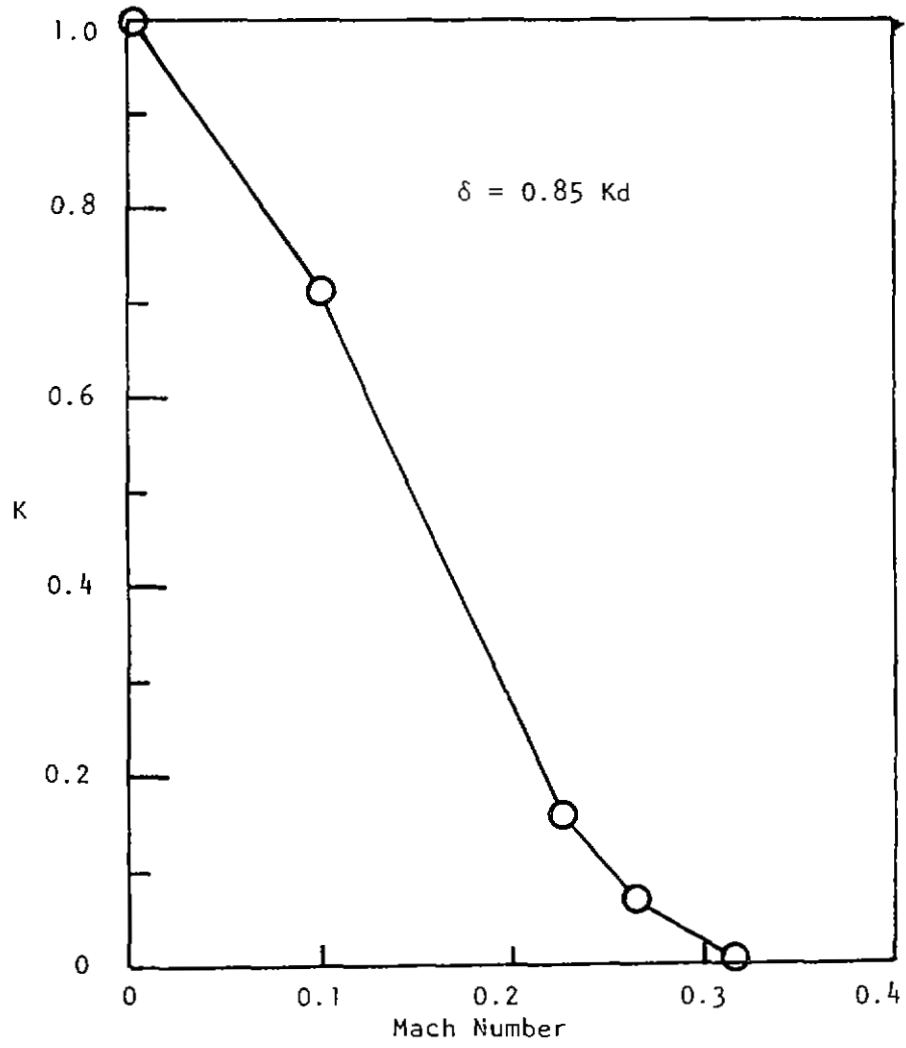


Figure 12. Dependence of End Correction Coefficient, K , on Mach Number.

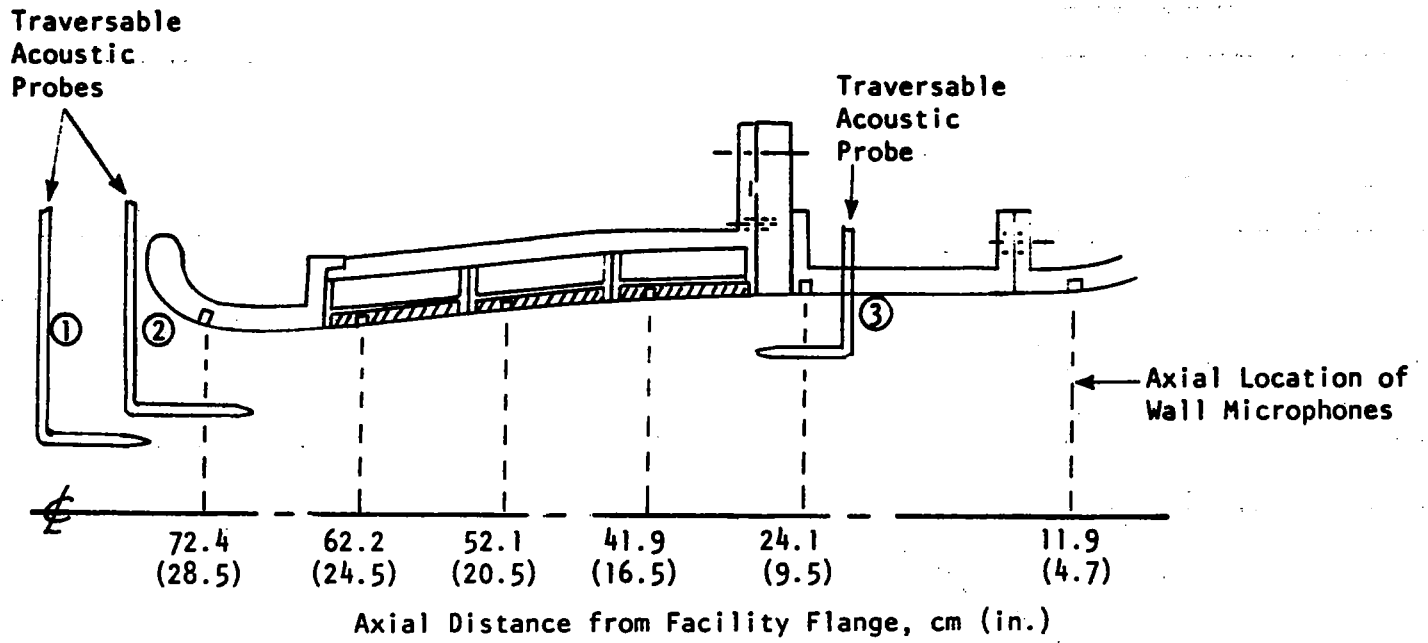
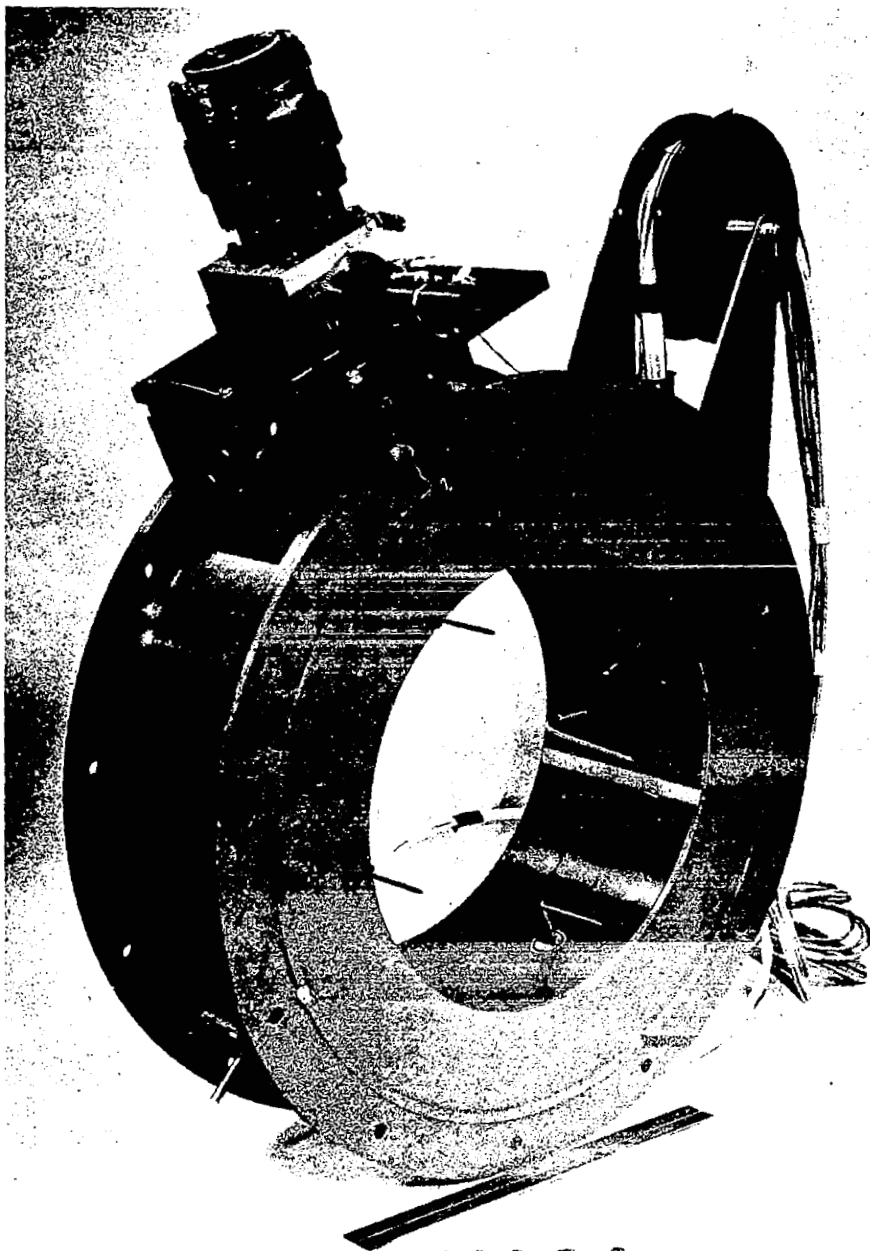


Figure 13. In-Duct Microphone and Probe Instrumentation.



NASA
Langley
Spinning-Mode
Probe
- Jan 1975

Figure 14. Spinning-Mode Probe Assembly.

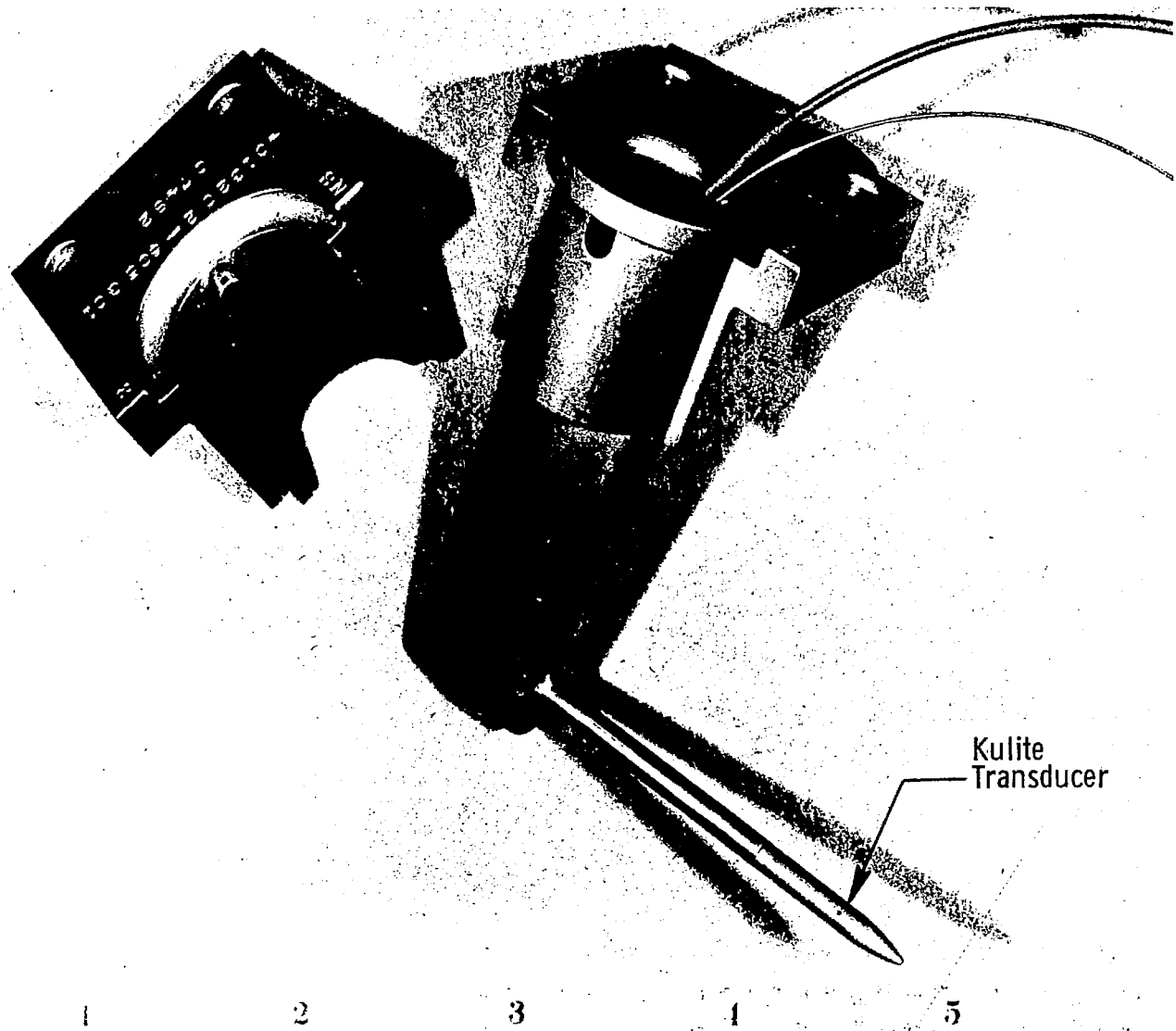


Figure 15. Individual Probe.

conjunction with the hot film turbulence data which were recorded at half of this tape speed.) At least one minute of data were recorded at each data point.

The far-field data were analyzed with a GR 1921 1/3-octave band analyzer, and adjusted from the atmospheric-absorption attenuation present under the ambient conditions of the test to standard day conditions, 15° C (59° F) temperature and 70% relative humidity, according to the method described in SAE 866(12). Sound power levels (PWL) were calculated assuming the sound wave propagates on a spherical wave front. Overall sound pressure levels were calculated by the summation of sound pressure levels at each 1/3-octave.

The modal measurement data reduction consists of the calculation of cross-spectral densities between each of the traversing probes and the reference probe at each circumferential immersion. This was accomplished using a Time Data Fast Fourier Analyzer system to provide tabulated cross-spectra in 40 Hz bandwidths. A total of 250 averages were used for each sample. At particular frequencies, the magnitude and phase of the cross-spectral density were plotted as a function of circumferential angle to provide complex acoustic pressure profiles. These profiles were then expanded into component spinning modes using a numerical Fourier analysis procedure(13).

5.2.2 Aerodynamic

The aerodynamic instrumentation consisted of static pressure taps, located along the length of the inlet duct, and a total pressure rake. For the turbulence intensity tests, a radially traversing hot film probe was installed between the centerbody support struts and the rotor, approximately 10.16 cm (4 in.) upstream of the rotor leading edge. Aerodynamic performance parameters, calculated from static and total pressure data, included wall Mach numbers, recovery, and distortion factors. The following methods of determining the weight flow and inlet throat Mach numbers were used.

Inlet weight flow for the high Mach number inlet was determined from the wall static pressure axial distribution. Inviscid inlet axial wall static pressure distributions were calculated for the hybrid inlet using a streamtube curvature (STC) flow analysis program(9) and compared with measured values at a number of different inlet weight flows. The predicted diffuser wall pressures were then adjusted by the effective boundary layer blockage to account for viscous effects:

$$P_S/P_{T_{inviscid}} \diamond A/A^*$$

$$A/A^*_{effective} = A/A^* \frac{(r - \delta^*)^2}{r^2}$$

$$A/A^*_{effective} \diamond P_S/P_{T_{viscous}}$$

Only static pressures aft of the minimum pressure were adjusted since viscous effects are negligible forward of this station. Predicted static pressure ratios below 0.5283 (sonic) could not be adjusted in this fashion.

At the plotted tap locations, the measured wall static pressure ratio was used to infer an inlet throat Mach number using analytical flow prediction techniques. Ideally, all static taps will indicate an identical throat Mach number for a given operating condition. This is unlikely to occur as a result of expected flaws in the model hardware or slight errors in the analysis. Thus, to obtain the final value, the throat Mach numbers indicated by all available static taps were averaged.

Inlet flows calculated using this method were corrected to fan face condition as follows:

$$\frac{W\sqrt{\theta}}{\delta_2} = \frac{W\sqrt{\theta}}{\delta_o} \left(\frac{1}{\eta\alpha} \right)$$

α = correction factor compensating for losses through vehicle struts ($\alpha = 0.986$ from previous test results)

η = measured inlet recovery, $\bar{P}_{T_{rake}}/\bar{P}_{T_o}$

The predicted fan face flows were then compared to the vehicle flow speed relationship as a check on the flow measurement procedure.

Wall Mach numbers were calculated from the static pressure measurements for each of the configurations at each of the fan speeds. Figure 7 shows a typical comparison of predicted and measured wall Mach numbers at the inlet design throat Mach number, 0.72. These results were used to infer the one-dimensional, average throat Mach numbers. The throat Mach numbers versus percent corrected speed were shown in Figure 6.

The recovery factors for the inlets were determined from the total pressures measured with the twenty element radial rake located in the instrumentation spool. The recovery for the hybrid inlet was generally the same both with and without the inlet turbulence screen. The rake total pressure profiles from which the recovery factors were calculated are presented in Figure 16 for the accelerating and hybrid configurations at the two highest speeds. The data at 94% fan speed indicate consistently higher total pressures and therefore higher recovery for the high Mach number inlet when the hardwall panels are installed than with treatment liners. At 97.5% fan speed the profiles cross at approximately 1.2 cm (0.47 in.) from the wall such that the resulting average total pressure and likewise the calculated recovery were about the same. The pressure levels of the accelerating inlet were lower along the wall also suggesting local shocks near the wall for this speed.

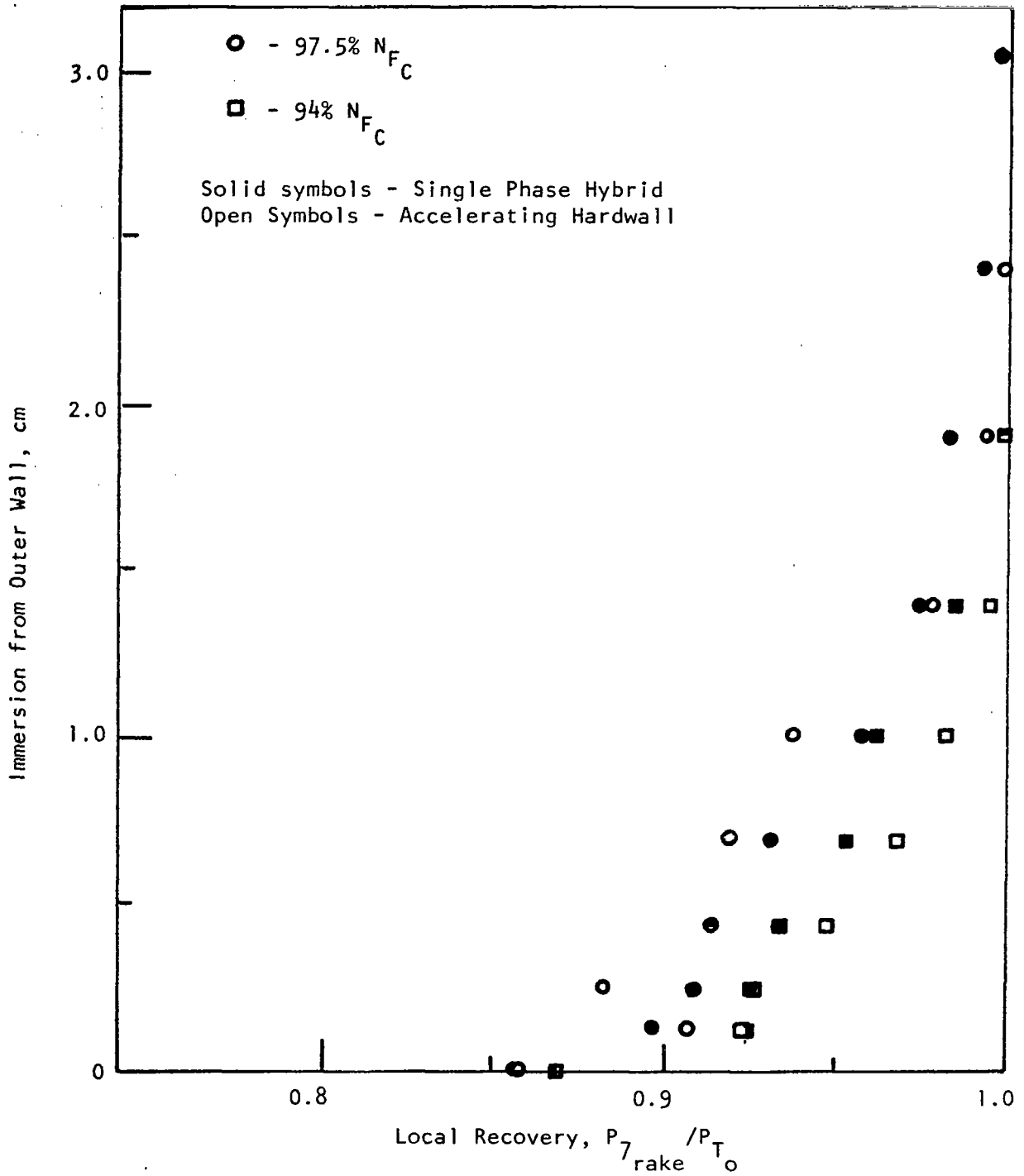


Figure 16. High Mach Number Inlet Rake Total Pressure Profiles.

The airflow - speed relationship shown previously in Figure 4 is based on the static pressure measurements and the calculated recovery factor. The corrected flow derived from the flow function for the one-dimensional, average throat Mach number was adjusted by these recovery factors as well as by the empirical strut loss factor (from previous tests) in order to determine the corrected flow at the fan face. The flows agree very well with the calibration curve which was determined by previous aerodynamic tests with a flow measuring bellmouth in conjunction with the compressor manufacturer's calibration data.

Measurements of flow turbulence were made inside the inlet of the test vehicle to assess the severity of the turbulence impacting the fan rotor. This was accomplished by radially traversing a two-dimensional "X" array hot film probe (TSI Model 1240-60) upstream of the fan rotor as shown in Figure 17. A sketch of the probe tip and 0.64 cm probe support is included in Figure 18. The two probe elements provided turbulent velocity data in the axial and circumferential directions. The probe operates on a heat transfer principle such that as the mass flux (ρv) varies at the measuring station, heat transfer to the fluid varies proportionally. This heat transfer change results in a voltage signal. Measurements were taken close to the rotor in order to obtain the turbulence characteristics injected by the rotor. The probe was positioned circumferentially such that it would be outside the wake of the centerbody support struts.

A block diagram of the hot film probe data acquisition equipment is shown in Figure 19. Signals A and B from the two probe tip sensors were measured by the two TSI Model 1054A anemometer units, where the signals were amplified and linearized. These signals were then added and subtracted in the TSI Model 1063 sum and difference unit. The probe was oriented such that axial velocity was proportional to the mean value of the (A + B) signal, while the transverse (circumferential) velocity was proportional to the (A - B) signal.

Requirements for frequency response to zero Hertz made it necessary to record the data DC-coupled. A technique was thus required to remove the steady DC voltage from the raw hot film A + B signal to preserve good signal-to-noise ratio on tape. This DC suppression was accomplished by a two step process. First the A + B signal was passed through a TSI Model 1057 signal conditioner where an integer number of volts were subtracted from the signal. The remaining fractional DC voltage was then subtracted by a battery-potentiometer setup. Hence the signal recorded on tape was essentially AC information, which retained frequency response to zero Hertz.

Since the steady DC voltage was removed before recording, but was required for mean velocity calculations, two digital volt meters were used to read the mean values of the raw A + B and A - B signals on-line. RMS values of these two signals were also read using TSI Model 1060 RMS volt meters. Model 122 NEFF linear DC amplifiers were used ahead of the tape recorder to boost signals to a level which would provide good signal-to-

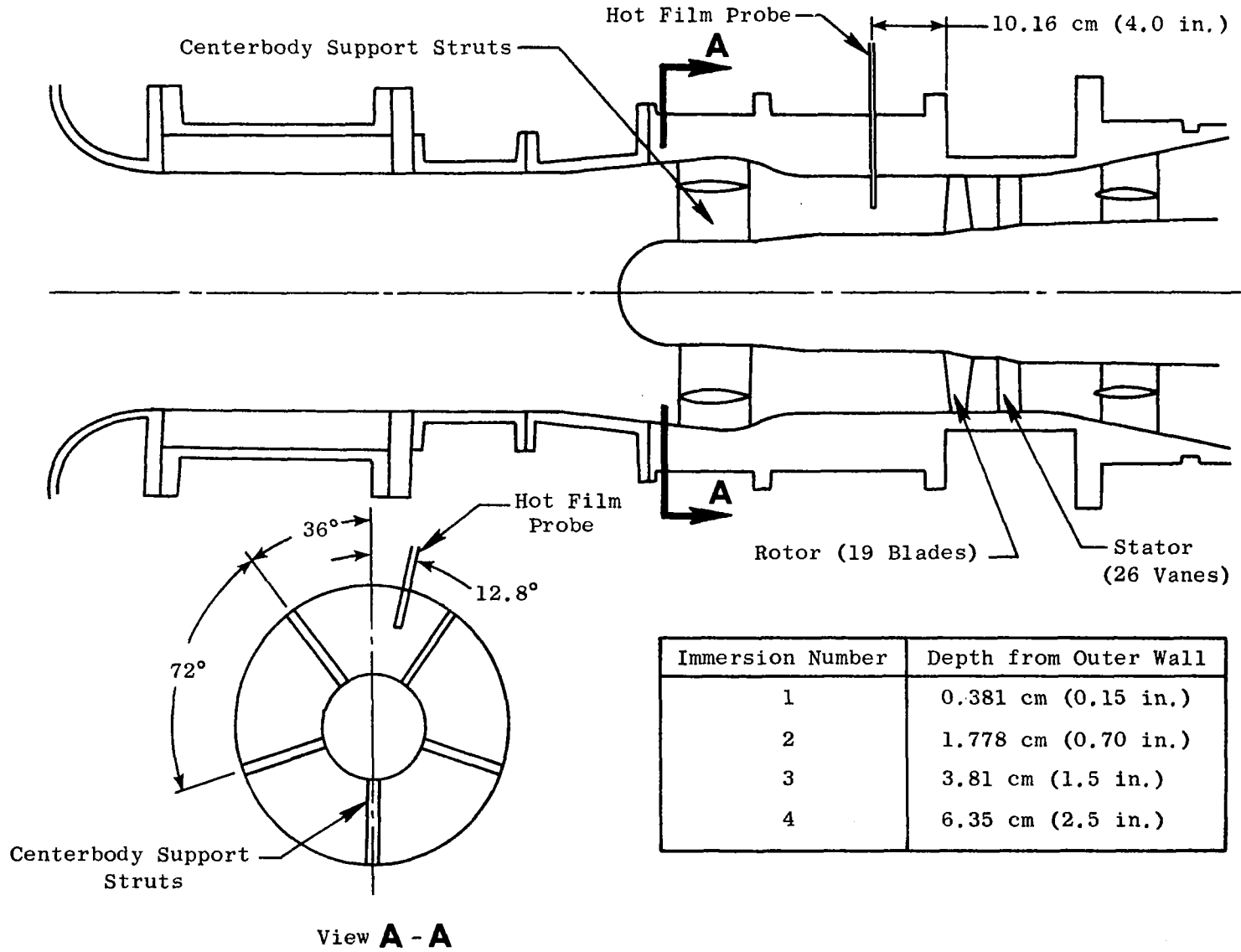


Figure 17. Hot Film Probe Installation in Test Rig.

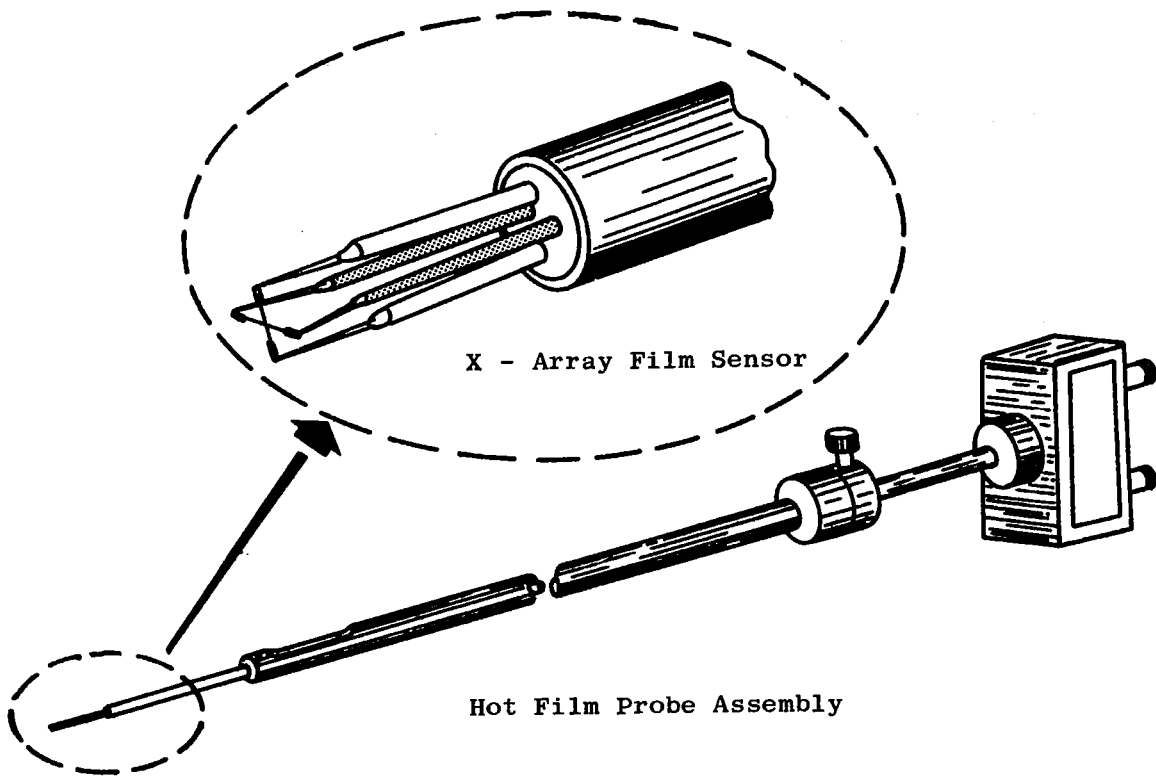


Figure 18. Hot Film Probe Assembly.

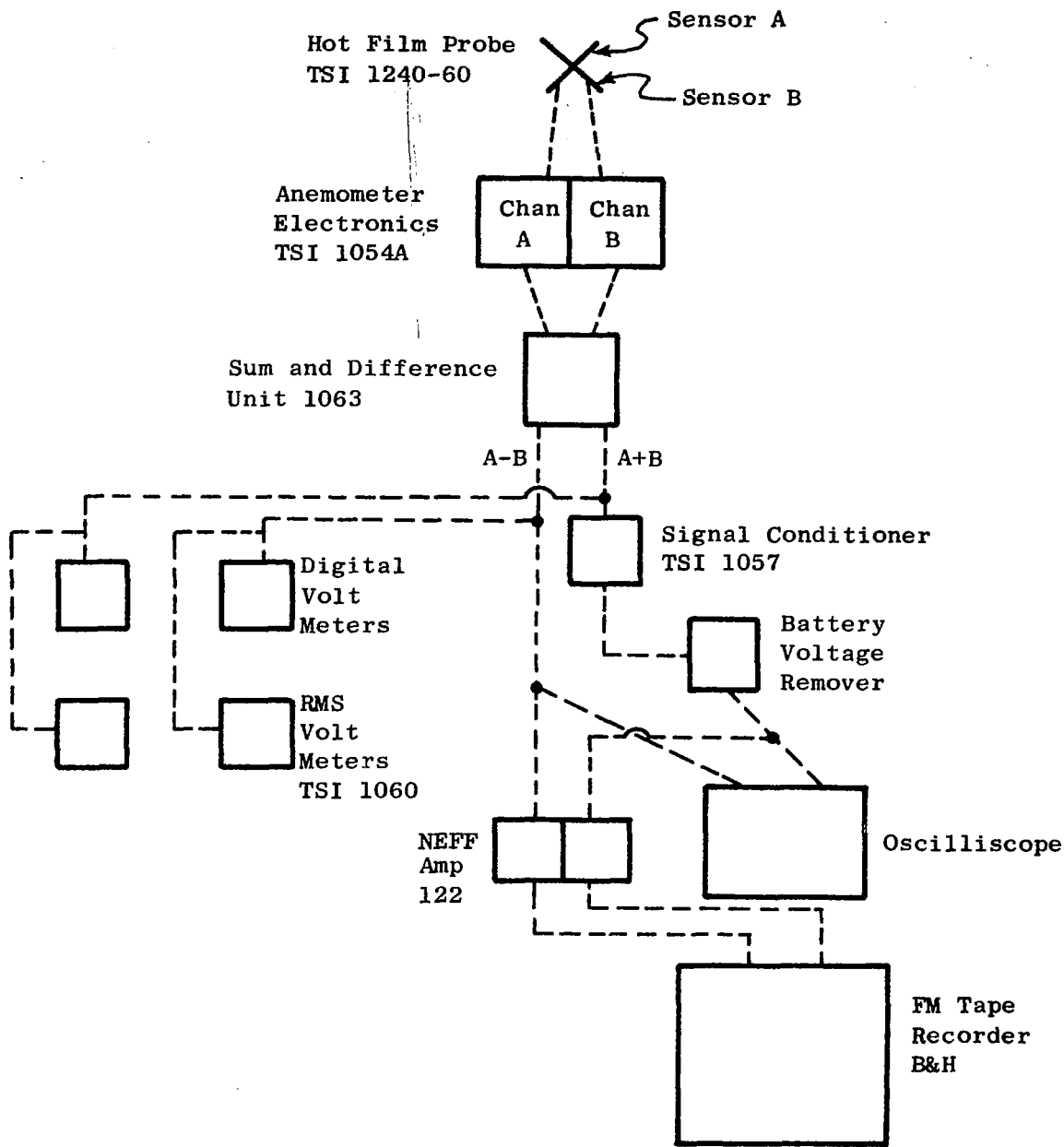


Figure 19. Block Diagram of Hot Film Probe Instrumentation Setup.

noise ratio on tape. An oscilloscope was used to monitor the signals just ahead of recording on the FM Bell & Howell 14-track tape recorder.

Five minutes of hot film probe data were recorded for each data point in order to provide sufficient record length for statistical repeatability. In addition to turbulence data, one minute of acoustic data from the nine far-field microphones was recorded at each data point. This far-field sound information was recorded with the hot film probe completely removed from the flow.

The axial integral-length scale was determined by:

$$L = \bar{U} \int_0^{T_0} \frac{R_{uu}(\tau) dt}{R_{uu}(0)}$$

and the turbulence intensity components were determined by:

$$\text{Axial Intensity} = \frac{\sqrt{\bar{u}^2}}{\bar{U}} = \frac{\sqrt{R_{uu}(0)}}{\bar{U}}$$

$$\text{Traverse Intensity} = \frac{\sqrt{\bar{v}^2}}{\bar{U}} = \frac{\sqrt{R_{vv}(0)}}{\bar{U}}$$

Where: $R_{xx}(\tau)$ is the autocorrelation function

$$R_{xx}(\tau) = \frac{1}{T} \int_0^T x(t)x(t+\tau) dt$$

T_0 is the minimum time delay required for the autocorrelation function to reach zero.

The operations indicated by these equations were done by means of a digital Time Data Fast Fourier analyzer for a 0 to 200 Hz turbulence spectral range. This range was adequate because the relative turbulent energy above 50 Hz was negligible; the resulting bandwidth resolution was 0.1 Hz.

5.3 TEST PROGRAM

5.3.1 Acoustic

The acoustic test program consisted of a series of tests with cylindrical inlets and a series of high Mach number hybrid inlet tests. The treatment configurations and speed points run for these tests are summarized in Table III for the cylindrical inlets and Table IV for the high Mach inlets. In addition, measurements were taken with the spinning mode probe for three configurations, as summarized in Table V.

The turbulence, and related acoustic measurement, aspect of the test program consisted of testing three inlet configurations, each with and without an inlet screen. The three inlets tested were the hardwall cylindrical, accelerating, and single-phase hybrid configurations. Three speed points (74%, 89%, and 94%) were run for each of the six configurations.

5.3.2 Aerodynamic

Aerodynamic performance measurements were taken for the accelerating hardwall and hybrid single phase configurations, as indicated in Table IV. Hot film probe measurements of mean flow turbulence intensity were taken during the turbulence test program for the six configurations mentioned previously, in conjunction with the acoustic data.

5.4 ACOUSTIC DATA SCALING

Although the primary interest in the acoustic data is for the actual 12 inch diameter size, meaningful comparisons of interest to design engineers require that the data be also presented so as to be representative of a typical full size vehicle. In particular, comparisons involving the PNL unit are meaningful only when the data are scaled, and so where pertinent, this has been done for the data presented in Section 6. For this purpose, the full size vehicle assumed as being representative consisted of the key parameters listed in Table VI, with the actual test vehicle (model) parameters shown for direct comparison. Sound levels, L, were scaled by:

$$L_{FS} = L_M + 10 \log (W_{FS}/W_M)$$

and, frequencies, f, were scaled by:

$$f_{FS} = f_M \times \frac{D_M}{D_{FS}} \times \frac{B_{FS}}{B_M}$$

Table III. Cylindrical Inlet Acoustic Test Points.

Configuration	Duct Liner Configurations		Percent Stage Speed, % N_{FC}							
	Flow	Sound	44	69	74	79	89	94	99	Other
1. HARDWALL			X	X	X	X	X	X	-	54%, 84%
2. SINGLE PHASE			X	X	X	X	X	X	-	-
3. PHASED (ABC)			X	X	X	X	X	X	-	-
4. PHASED (CBA)			X	X	X	X	X	X	-	-
5. PHASED (DEF)			X	X	X	X	X	X	-	-
6. PHASED (FED)			X	X	X	X	X	X	-	-
7. PHASED (BAC)			X	X	X	X	X	X	-	-
8. PHASED (CAB)			X	X	X	X	X	X	-	-
9. PHASED (ABF)			X	X	X	X	X	X	-	-
10. PHASED (BAF)			X	X	X	X	X	X	-	-
11. PHASED (AAF)			X	X	X	X	X	X	-	-
12. PHASED (AAH)			X	X	X	X	X	X	X	-
13. PHASED (AAC)			X	X	X	X	X	X	X	-
14. PHASED (EAC)			X	X	X	X	X	X	X	-
15. PHASED (AEC)			X	X	X	X	X	X	X	-
16. HARDWALL (REP.)			X	-	X	X	X	X	X	-
17. PHASED (AAB)			X	X	X	X	X	X	X	-
18. PHASED (ABA)			X	X	-	X	X	-	-	-
19. HARDWALL (REP.)			X	-	X	X	X	X	-	91%, 97.5%
20. PHASED (CAE)			X	-	X	X	X	X	-	-

* See Section 5.1.4 for definition of panel construction.

Table IV. High Mach Inlet Acoustic Test Points.

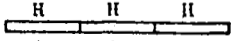
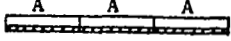
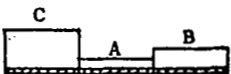

CONFIGURATION	DUCT LINER CONFIGURATIONS FLOW → ← SOUND	Percent Stage Speed, % N_{FC}					
		74	79	89	91	94	97.5
21. HARDWALL		X	X	X	X	X	X
22. SINGLE PHASE		X	X	X	X	X	X
23. PHASED (CAB)		X	X	X	X	X	X
24. PHASED (CAE)		X	X	X	X	X	X

Table V. Mode Probe Acoustic Test Points (Cylindrical Inlet).

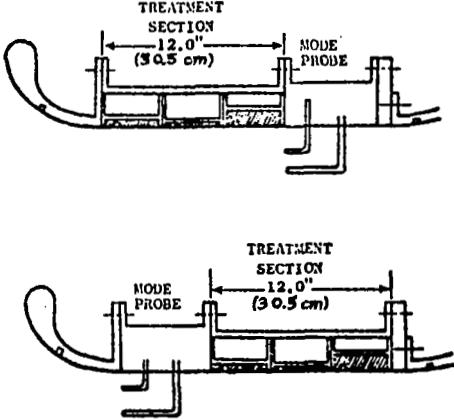
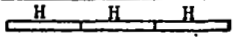

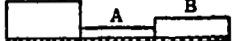
CONFIGURATION	DUCT LINER CONFIGURATIONS FLOW → ← SOUND	Percent Stage Speed, % N_{FC}			Mode Probe Position 
		44	79	89	
25. HARDWALL		X	X	X	
26. SINGLE PHASE		X	-	X	
27. PHASED (CAB)		X	-	X	

Table VI. Scaling Parameters.

Parameter	Model	Typical High Bypass Fan
Design Fan Tip Speed	396.5 m/sec (1301 ft/sec)	396.5 m/sec (1301 ft/sec)
Fan Diameter	30.5 cm (12 inch)	180.3 cm (71 inch)
Design Rotational Speed	24,847 rpm	4,200 rpm
Design Flow	11.9 kg/sec (26.3 lbm/sec)	426.0 kg/sec (940.5 lbm/sec)
Number of Blades	19	28

where: D = Vehicle diameter
B = Blade number in the rotor

Subscripts: FS = Full scale
M = Model

All dimensional data and vehicle rpm's are quoted only for the actual (model) test vehicle.

SECTION 6.0

RESULTS AND DISCUSSION

This section presents the results of the analytical and experimental work done toward meeting each of the three principal objectives. Because of its importance in the analytic prediction of suppression, the results of the measurement of the acoustic modes in the inlet are presented and discussed first. Next, the results of the tests of the cylindrical inlet are given, followed by the comparison of the predicted (by ACTAMD) versus measured suppression for those cases for which the analysis could be performed successfully. Then, the experimental results are presented and discussed for the high Mach inlets and for the turbulence study.

6.1 ANALYSIS OF SPINNING MODE PROBE RESULTS

6.1.1 Determination of Modal Information for Use in ACTAMD

Spinning mode measurements were performed for two different inlet configurations, first in a duct with hardwall panels in place of treatment with the mode probe on the rotor side (downstream) of the treatment location, and second in a treated duct with the mode probe located on the inlet side (upstream) of the treatment. The measurements were performed at three operating speeds, 44%, 79%, and 89%. The measurements were made at one radial position, using the circumferentially traversing mode probe apparatus described in Section 5.2.1.

The experiment was exploratory in nature, aimed at providing information about the feasibility of the method under conditions of airflow Mach number and fan tip speeds typical of aircraft turbofans. A detailed description of the modal measurement experiment and results can be found in Reference 14.

The spinning-mode probe data reduction consists of: (1) the calculation of cross-spectra between probe and reference signals for a large number of angular positions, (2) the plotting and smoothing of the cross-spectrum magnitude and phase versus angle for a number of chosen frequencies, and (3) the Fourier analysis of the resulting complex functions of azimuth expanding them into component spinning modes. The cross-spectrum calculation was accomplished on a Time/Data Fast Fourier Analyzer System.

Results of the modal measurements for the hardwall configurations at 44% speed blade passing frequency and second harmonic and for the 79% speed blade passing frequency are presented in Figures 20 to 25. These include the complex acoustic pressure profiles and their expansion into spinning modes. Tyler-Sofrin rotor-stator interaction theory (Reference 7) predicts the excitation of modes with circumferential mode orders given by

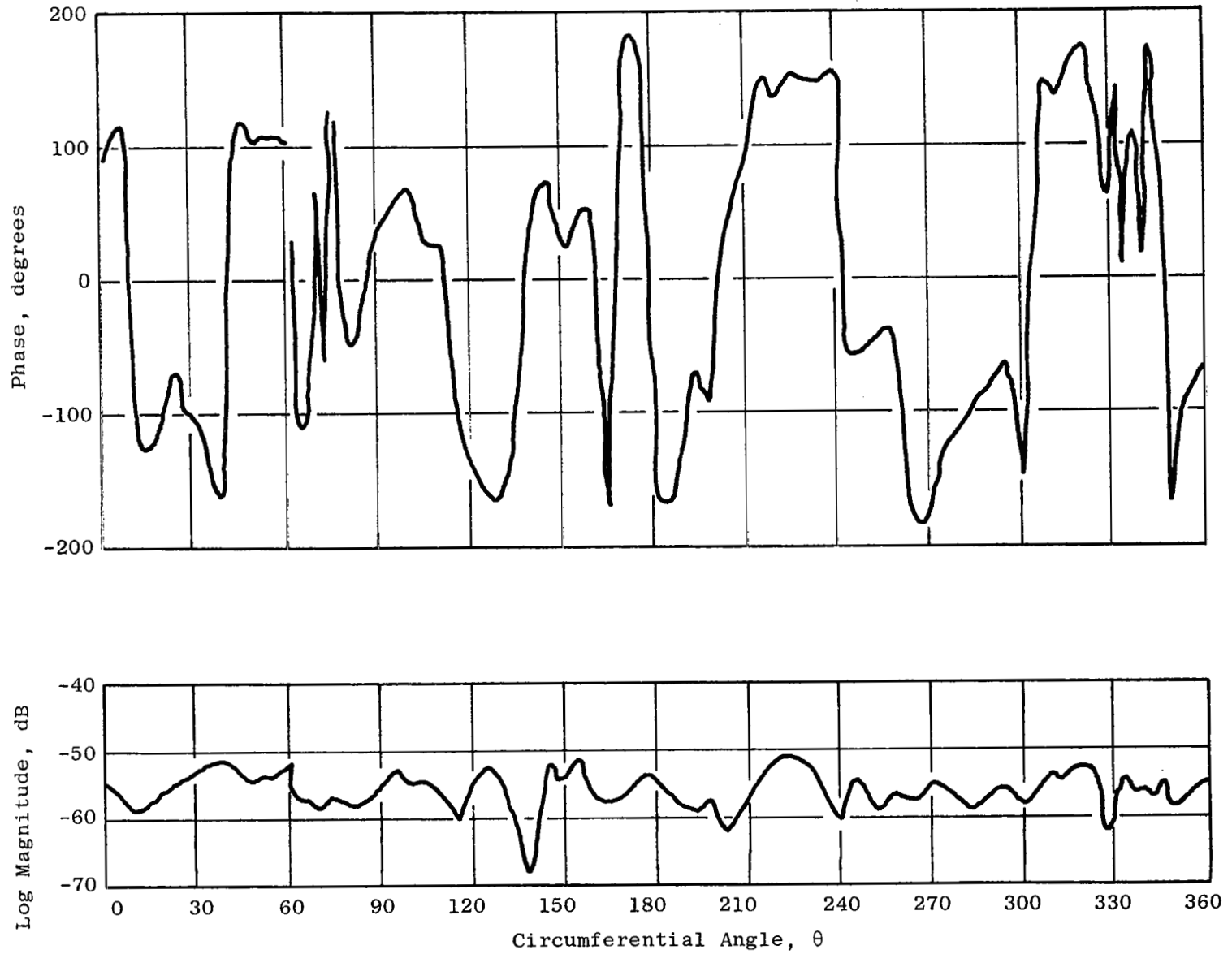


Figure 20. Complex Pressure Profile from 40 Hz Bandwidth Cross Spectrum, 44% Speed, 3440 Hz, Blade Passing Frequency, Hardwall Configuration.

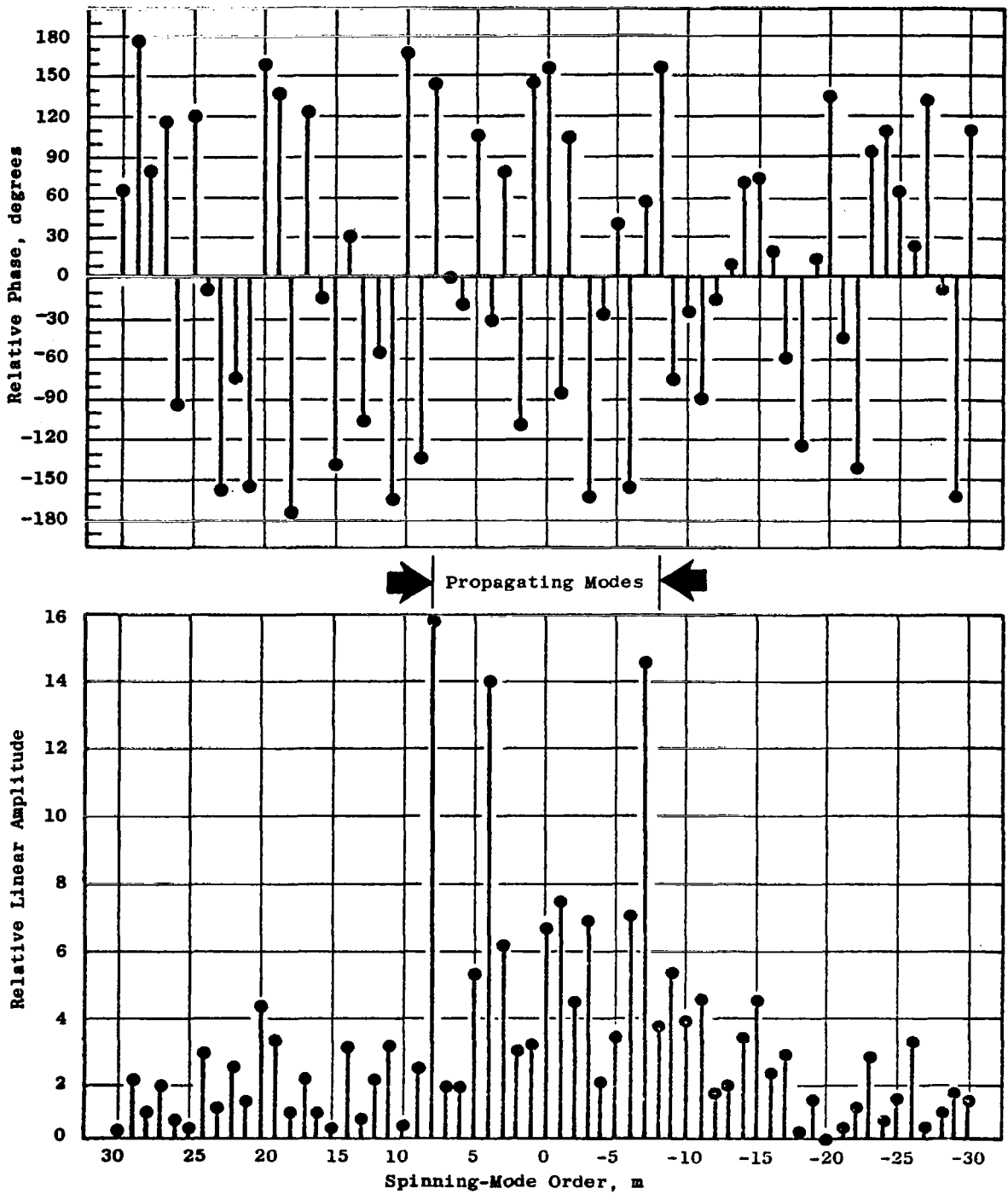


Figure 21. Measured Spinning-Mode Content for 44% Speed, 3440 Hz, Blade Passing Frequency.

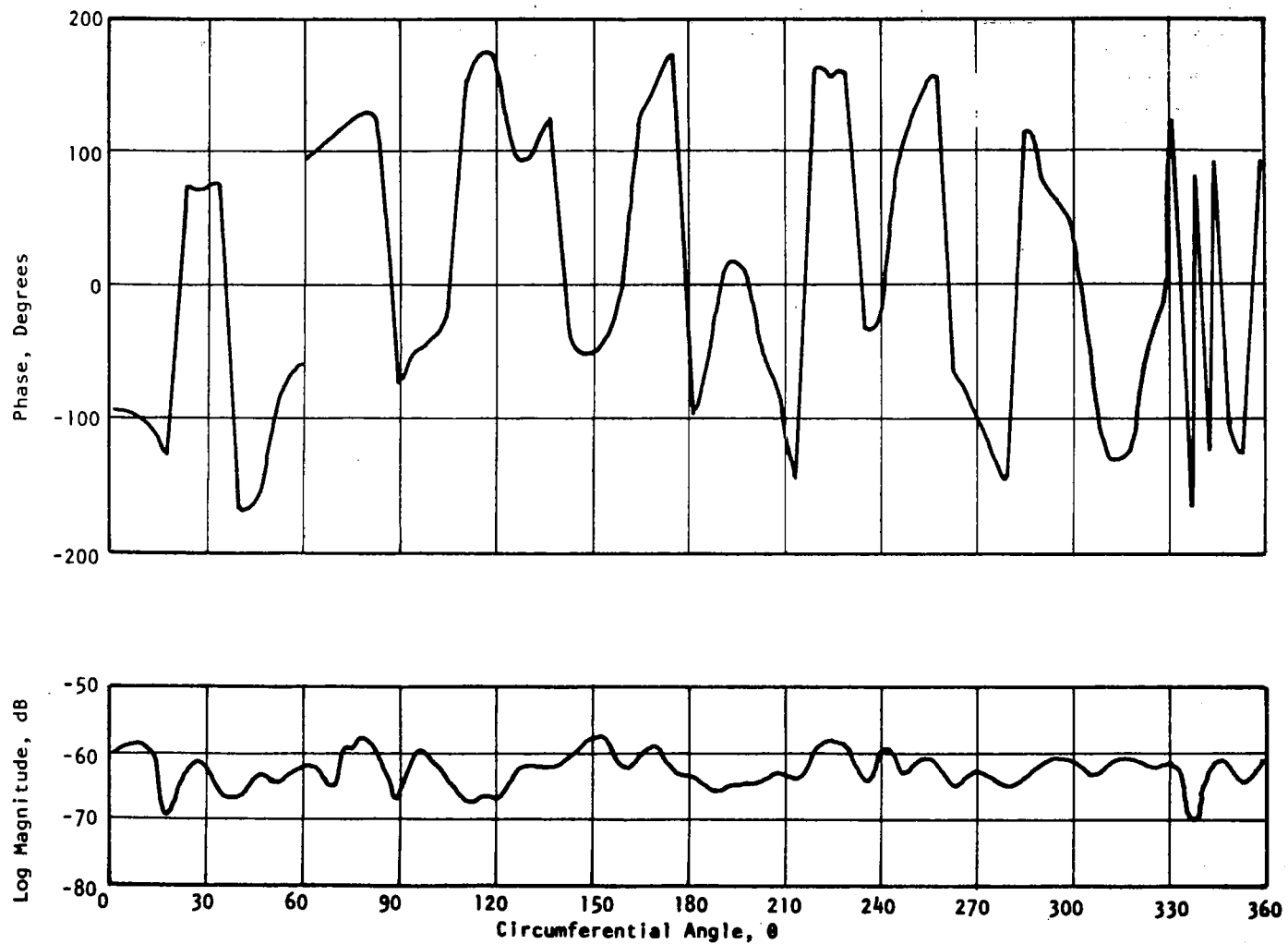


Figure 22. Complex Pressure Profile from 40 Hz Bandwidth Cross Spectrum, 44% Speed, 6920 Hz, Second Harmonic, Hardwall Configuration.

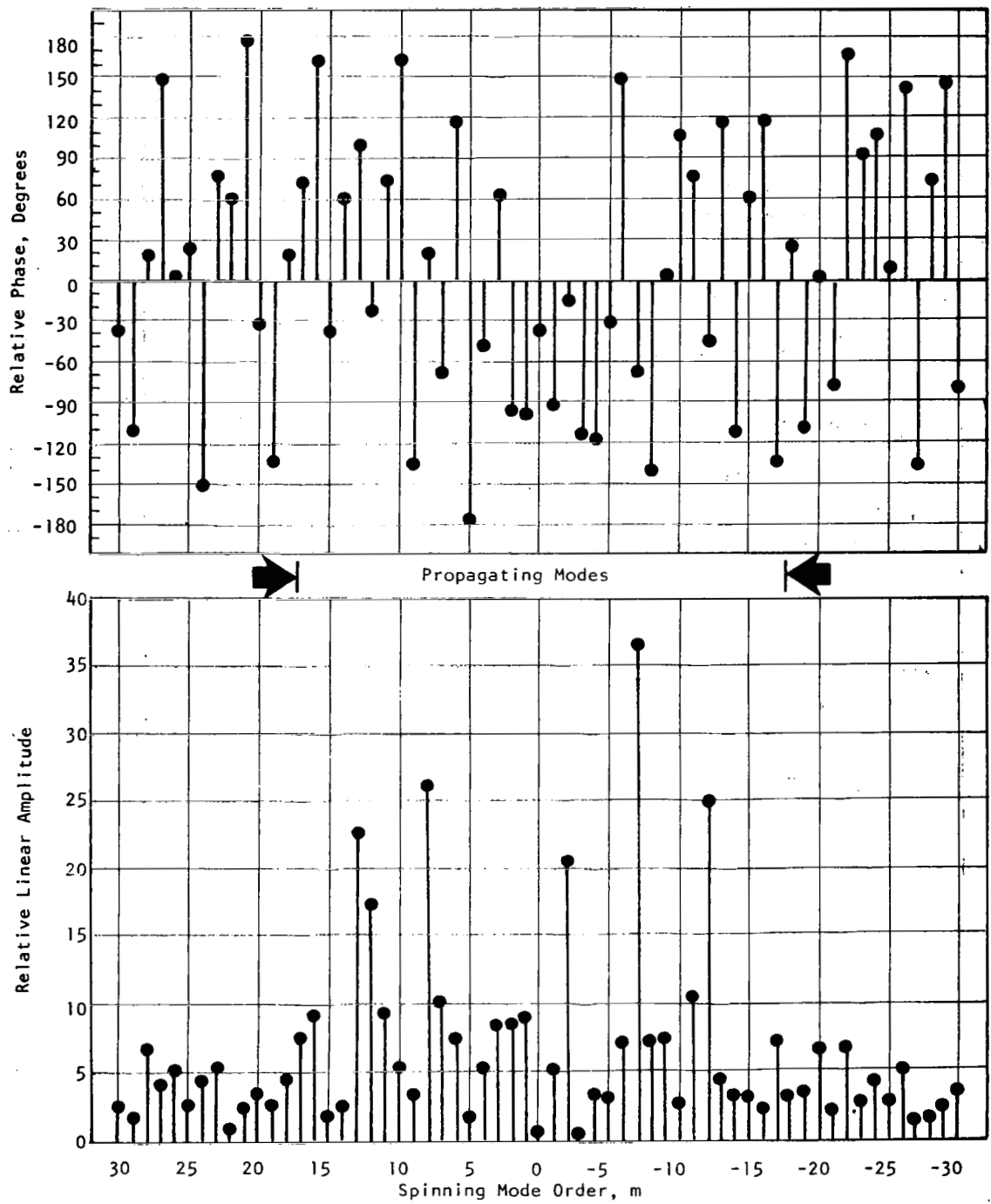


Figure 23. Measured Spinning Mode Content for 44% Speed, 6920 Hz, Second Harmonic.

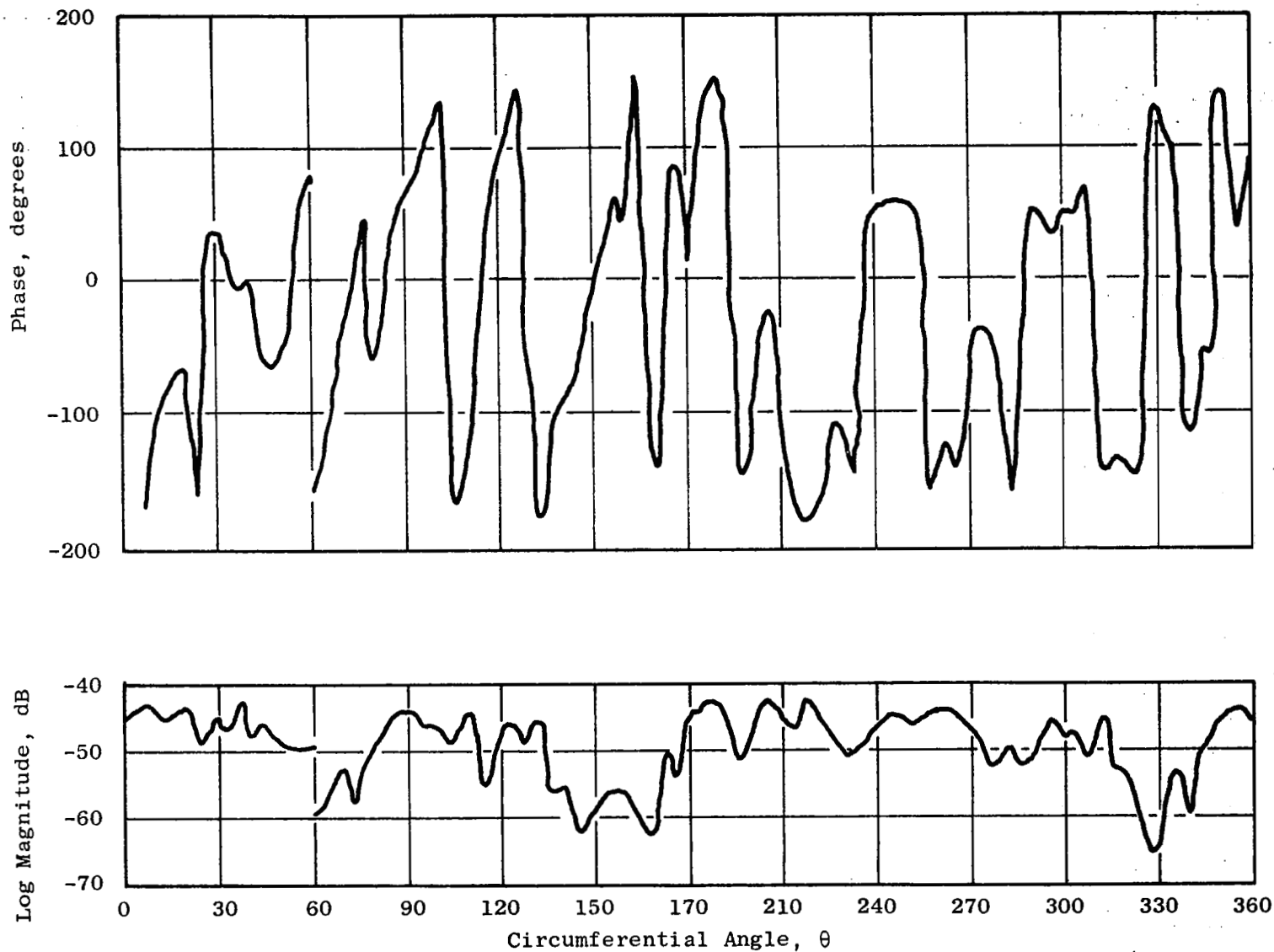


Figure 24. Complex Pressure Profile from 40 Hz Bandwidth Cross Spectrum, 79% Speed, 6120 Hz, Blade Passing Frequency, Hardwall Configuration.

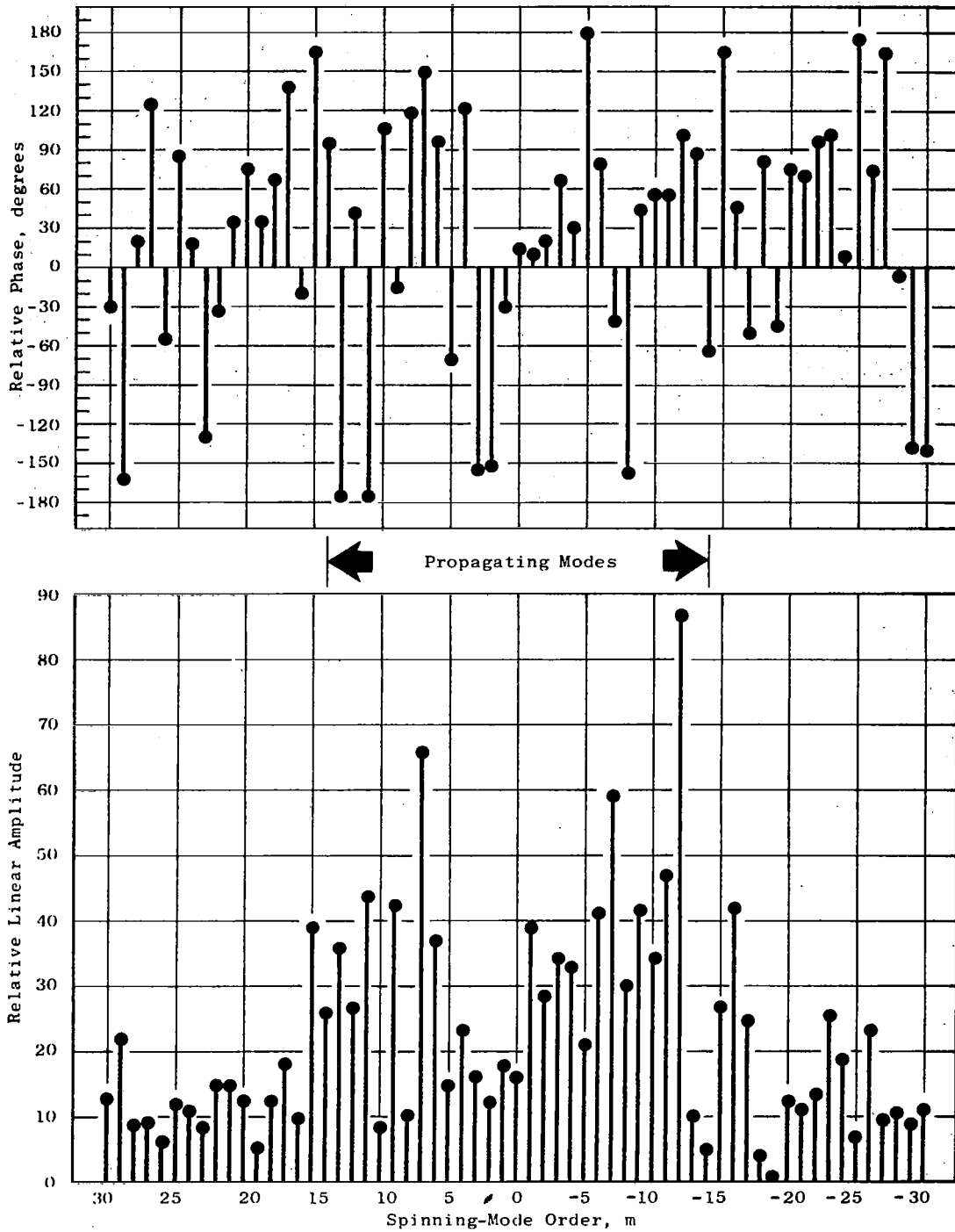


Figure 25. Measured Spinning-Mode Content for 79% Speed, 6120 Hz, Blade Passing Frequency.

$$m = nB \pm kV$$

where

m = spinning-mode order

n = harmonic number

B = number of blades

k = arbitrary positive or negative integer

V = number of vanes

In addition to the spinning modes which are predicted, account must be taken of those modes which are cut-on and cut-off, that is, which propagate unattenuated or decay exponentially in a hardwalled duct. At the blade passing frequency first harmonic ($n = 1$), the following spinning-mode orders (less than 30) would be predicted:

a) Rotor/OGV Interaction

$$V = 26, m = -7$$

b) Upstream-Strut-Rotor Interaction

$$V = 5, m = 29, 24, 14, 9, 4, -1, -6, -11, -16, -21, -26$$

At the second harmonic of blade passing frequency ($n = 2$), the following orders would be predicted:

a) $V = 26, m = 12, -14$

b) $V = 5, m = 28, 23, 18, 13, 8, 3, -2, -7, -12, -17, -22, -27$

The possibility that the acoustic wave may be scattered by the upstream struts into other modes is not taken into account by the Tyler-Sofrin analysis.

In the modal expansion of the blade passing frequency at 44% speed (Figure 21), it is seen that the +8, +4, and -7 order spinning modes predominate. The -1, +3, and -6 modes are also in evidence. The $m = -7, -6, -1,$ and +4 modes are predicted by interaction theory, but the +8 and +3 modes are not. Thus, all the lower order modes predicted to be present up through the eighth order are present. The $m = +9$ mode is predicted, but this mode should be cut-off.

The modal amplitudes measured for the second harmonic at 44% speed, (Figure 23) are dominated by the -7 and +8 order spinning modes; these are predicted. Other predicted modes which are present at relatively low levels are the +3, -14, -17, and +18 order modes (cut-off occurs between $m = 17$ and $m = 18$). Unpredicted modes which make significant contributions are the $m = \pm 6,$ and ± 11 order modes.

The modal expansion for blade passing frequency at 79% speed (Figure 87) shows the signal is clearly dominated by the unexpected $m = -12$ spinning mode. The ± 7 modes are strongly in evidence, but only the -7 is expected, indicating possible scattering by the struts. Similar behavior occurs for the ± 6 , ± 9 , and ± 11 order modes. The $m = -1$ and $+16$ order modes are predicted, and contribute at somewhat subdued levels. Orders above the sixteenth are cut-off.

In general, the above comparison shows some evidence of modes present which are not predicted by interaction theory, and also evidence of scattering by the struts. The measurement indicates that modes which are cut-off have decayed sufficiently to contribute very little to the pattern.

6.1.2 Repeatability

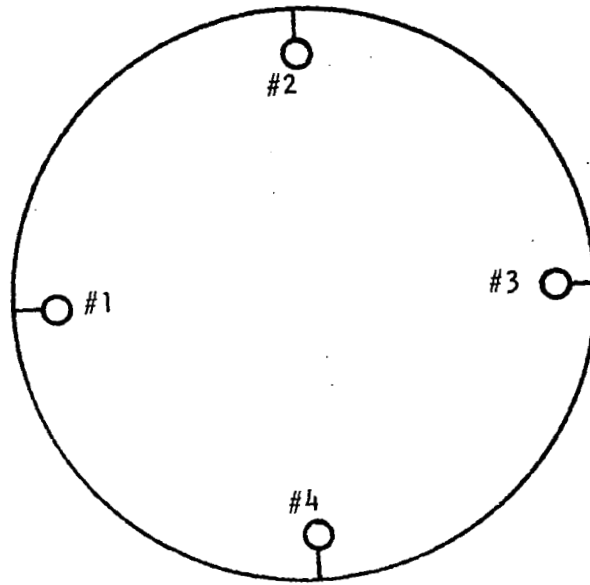
The mode-probe tests on the hardwall configuration were accomplished with one of the four rotating-probe elements inoperable. This required the probe to be rotated through an angle of 180° to obtain data over the full 360° arc. Two of the 90° segments were covered twice by different probes, as shown in Figure 26. The redundant data from the regions covered by two different probes were reduced and compared to the original data for a number of cases.

Figure 27 shows a particular case of the comparison between data measured by two different probes over the same arc, in the 44% speed blade passing frequency case. It is noted that both the magnitude and phase curves agree in general pattern, although differences as high as 10 dB in magnitude and up to 180 degrees in phase occur for certain angles. Similar results are obtained at 79% BPF and 44% second harmonic.

Examination of the modal measurement data acquired at 89% speed in the hardwall duct indicated a lack of data repeatability (see Reference 14). In this case, the rotor tip speed is supersonic, and it is suspected that the frequency modulation between BPF and the MPT's cause the generation mechanism to be non-stationary, as far as the modal measurement method is concerned. Low signal-to-noise-ratio tape recorder problems were encountered for the modal measurements taken in the treated configurations, so that this data was not analyzed in detail.

There is also a question of whether the mode-probe rakes might have affected the data. This question was investigated by Posey(15): using the mode probe apparatus in the configuration shown in Figure 28, a signal enhancement procedure was applied to the signal from a wall-mounted microphone as the mode probe was traversed circumferentially in discrete steps over an arc of 270° ; the variation in signal magnitude (up to 10 dB) and phase (up to 80 degrees) at the wall-mounted microphone as the mode probe changes position indicates, as shown in Figure 29, that there could have been an effect by the probe rakes on the acoustic field.

Physical Probe Locations



Probe Coverage

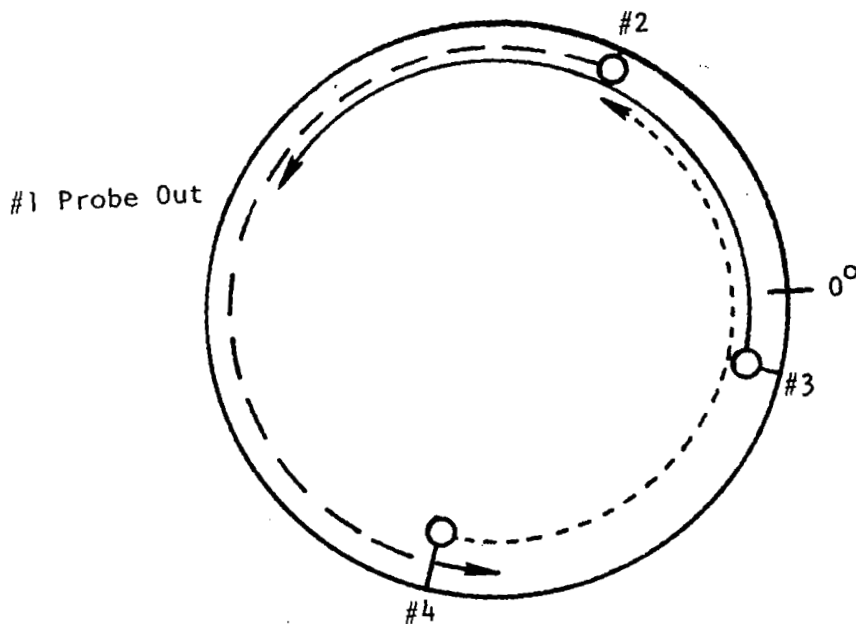


Figure 26. Explanation of Mode Probe Data Redundancy.

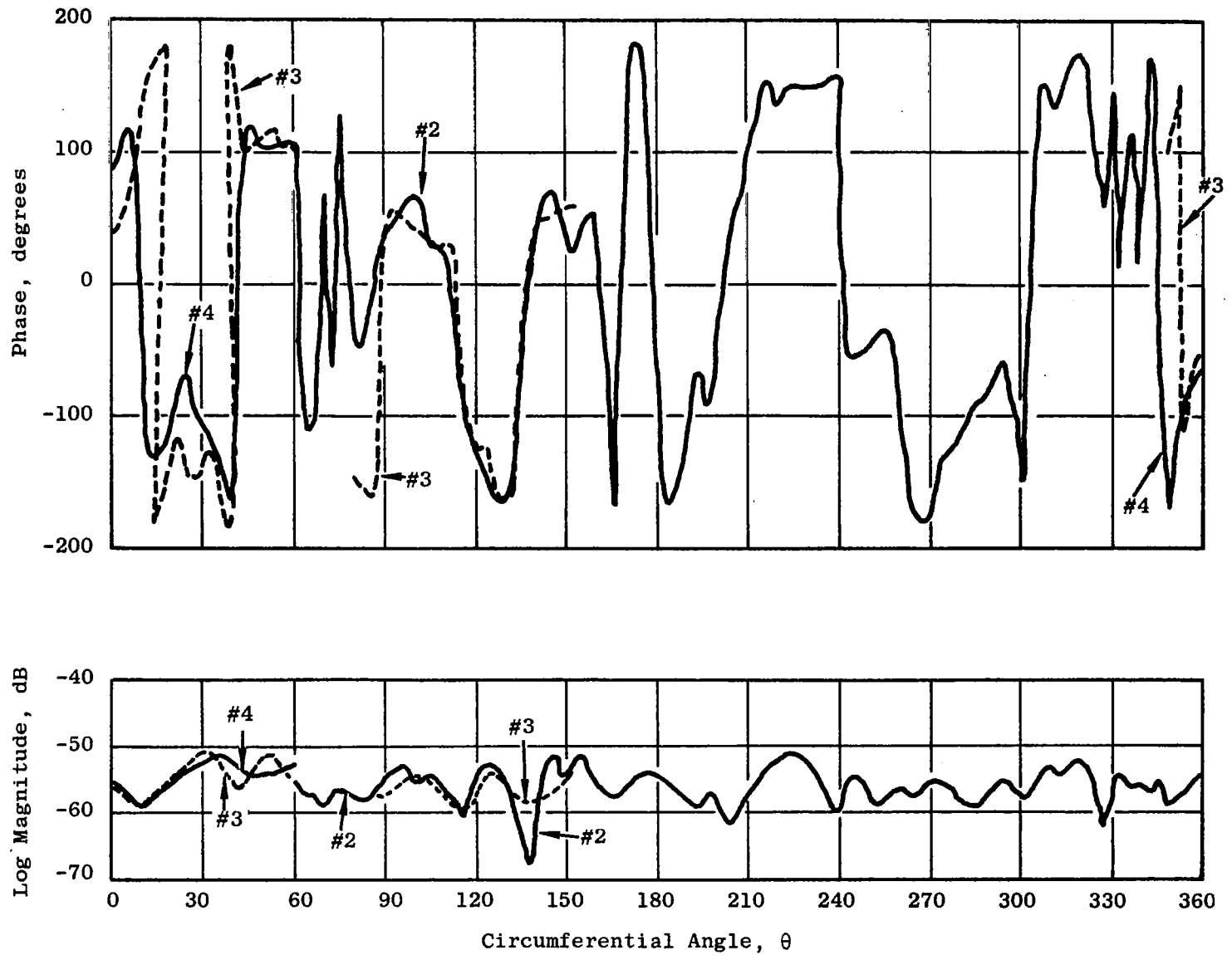


Figure 27. Complex Pressure Profile from 40 Hz Bandwidth Cross Spectrum, 44% Speed, 3440 Hz, Blade Passing Frequency, Hardwall Configuration, Comparing Repeatability of Data Acquired with Two Different Probes Over Same Arc.

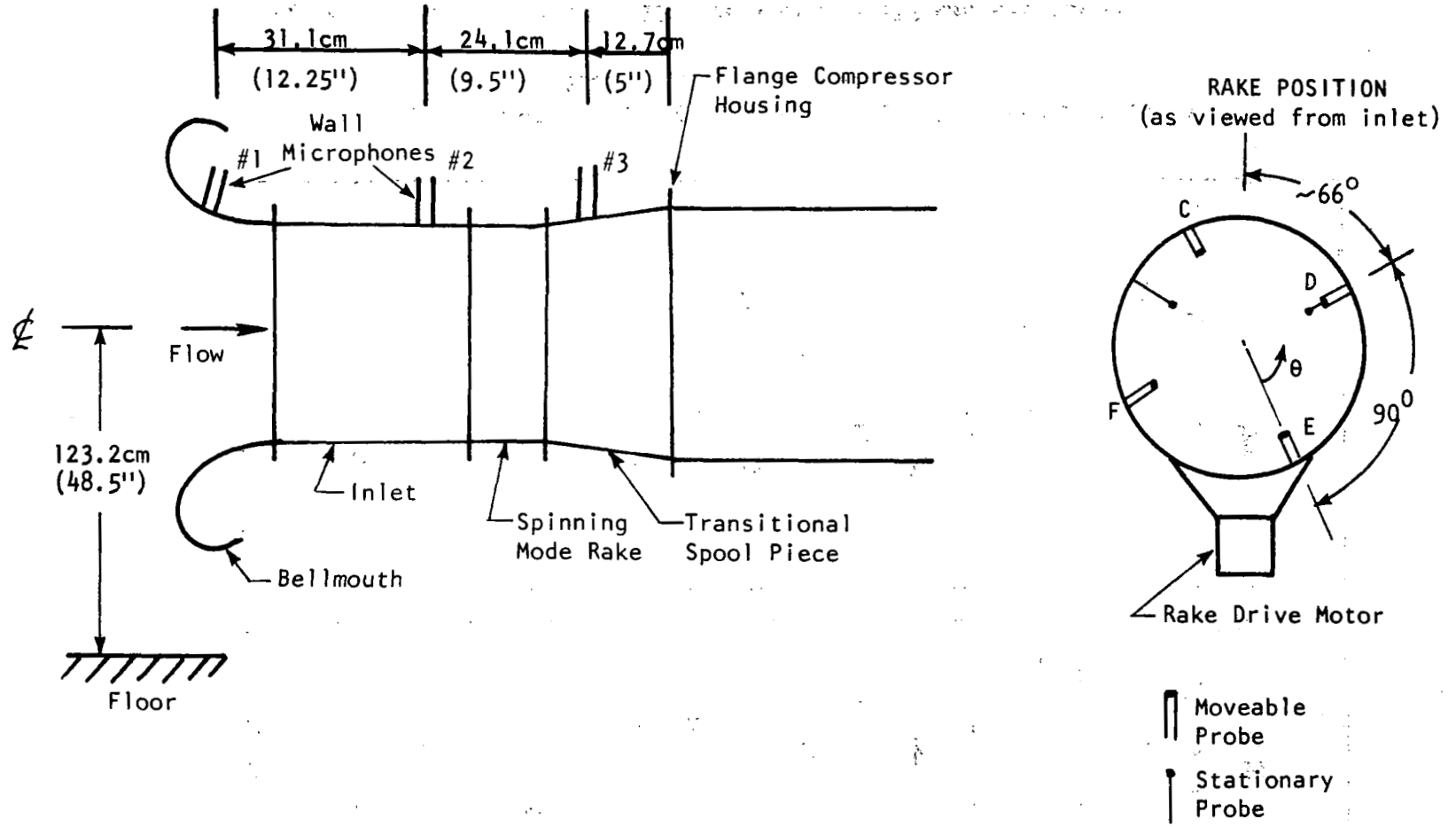


Figure 28. Inlet and Mode Probe Configuration for Test of Effects of Probe Position.

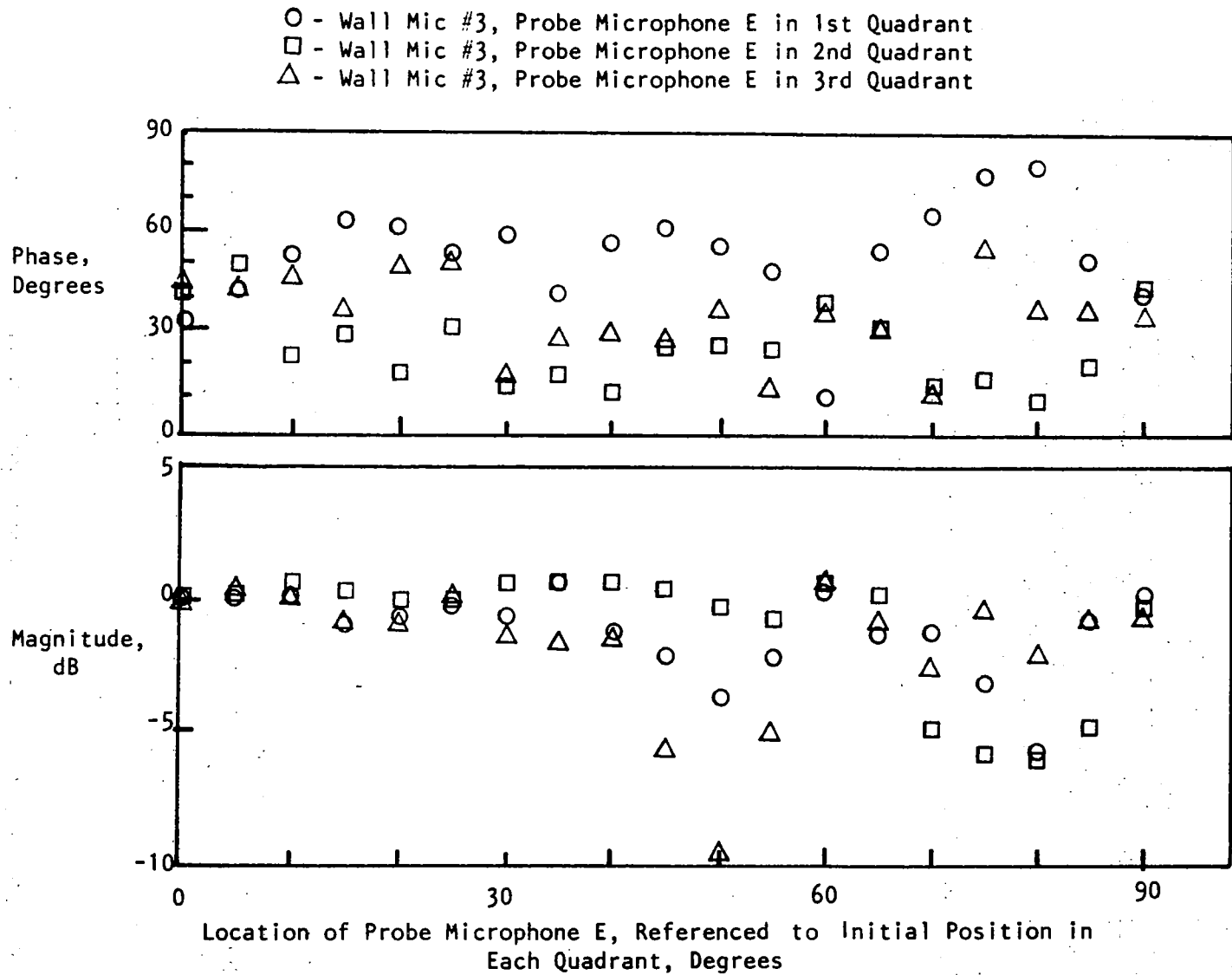


Figure 29. Variation of Wall Microphone #3 BPF Cross-Spectrum as a Function of Spinning Mode Probe Azimuthal Position.

A more extensive series of tests is required before definite conclusions can be drawn about the repeatability of the in-duct, immersed probe method of modal measurement. Attention should be paid not only to the repeatability of the complex pressure profile (cross-spectra) itself, but also to the variation in expanded spinning mode content, and how this variation affects predicted suppression results.

6.2 CYLINDRICAL INLET

Comparisons of the suppressions obtained with the treatment configurations defined in Table III are presented in Figures 30 to 32; the phased-treatment inlet suppressions (relative to the hardwall baseline) are summarized on the basis of: (1) blade passing frequency PWL, (2) OASPL at 50°, and (3) OAPWL. None of the phased-treatment combinations excels at all speeds, but three consistently produced less suppression than the other combinations: these were No. 5 (DEF), No. 6 (FED) (the configurations with low resistance liners) and No. 12 (AAH), the only configuration with only two softwall liners. Most of the remaining phased-treatment combinations produced equally good suppression and, on the basis of OASPL and OAPWL, produced more suppression than the single-phase configuration No. 2 (AAA). As would be expected, the single-phase liner (designed for the 1/3 octave band containing blade passing frequency over the vehicle speed range from 74% to 89%) provided more suppression of the blade passing tone. The phased combinations, with the exception of No. 17 and No. 18, had only one of the three panels tuned to the BPF. As defined by any of these three measures, panel order had no significant effect upon the suppression.

6.2.1 Basic Experimental Data

Six of the phased-treatment combinations generally performed equally well; these were: No. 4 (CBA), No. 8 (CAB), No. 9 (ABF), No. 10 (BAF), No. 11 (AAF), and No. 13 (AAC). Of these, No. 8 was selected as a representative phased liner combination for the comparisons discussed in the following paragraphs.

The 1/3 octave sound-power-level spectra for the hardwall, the single phase, and a representative phased (No. 8) configurations at the 74% fan speed are presented in Figure 33. The suppression attained with the single-phase liner at this speed for the four 1/3 octave bands immediately below the BPF band was between 8 and 9 dB, and 9.5 dB at BPF. The maximum suppression measured for the phased liner, on the other hand, was 15 dB, occurring six 1/3 octave bands below BPF, while about 7 dB reduction of the BPF power level was attained. The large reduction of low frequency noise with phased treatment occurred at all angles. Slightly more suppression was achieved with the single-phase treatment at BPF than with the phased treatment, but the loss was modest considering that the single-phase design was tuned solely to BPF, while the multi-phase design had only one of three liners tuned to BPF.

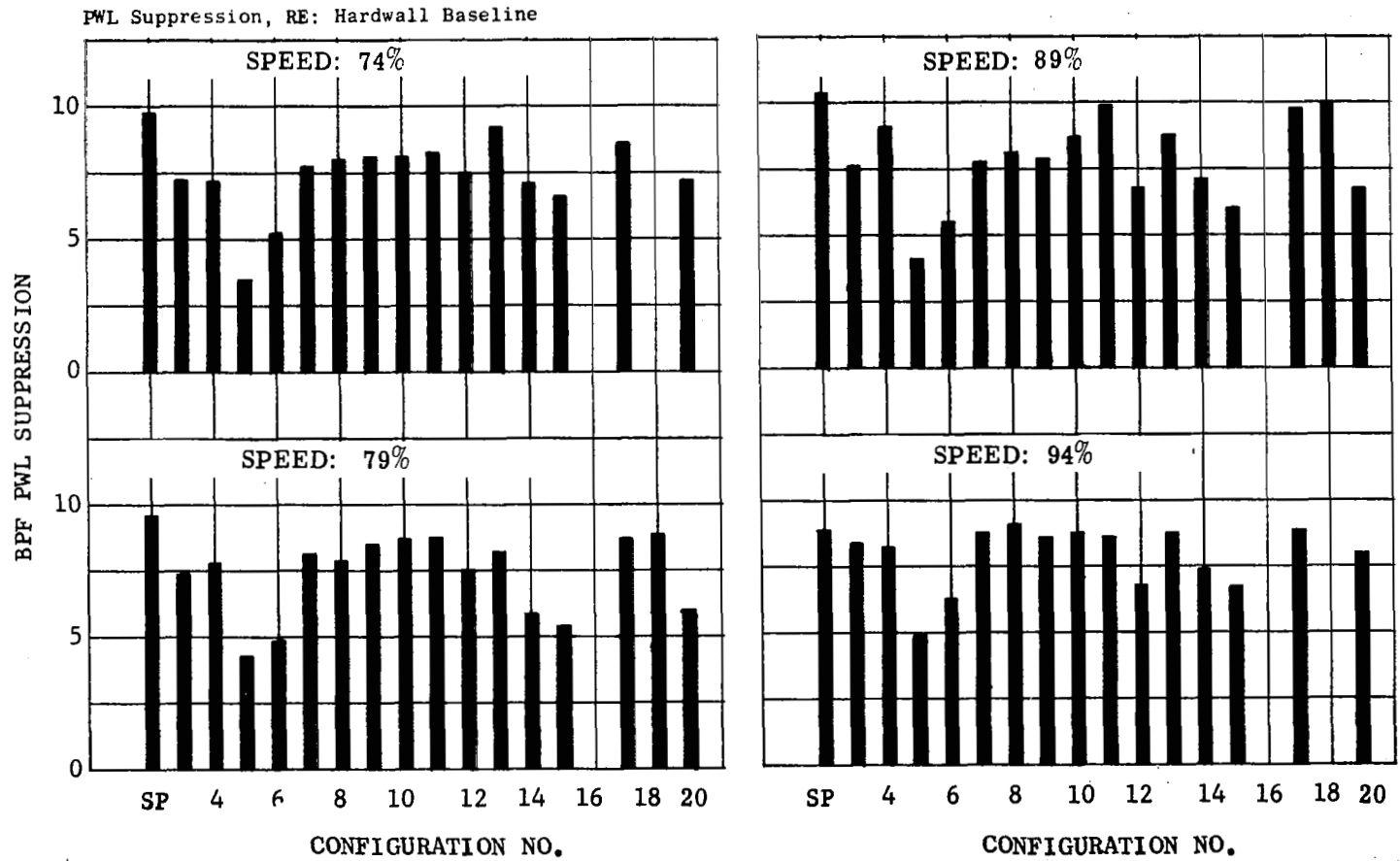


Figure 30. Summary of Phased-Treatment Blade Passing Frequency PWL Suppression at Four Fan Speeds:

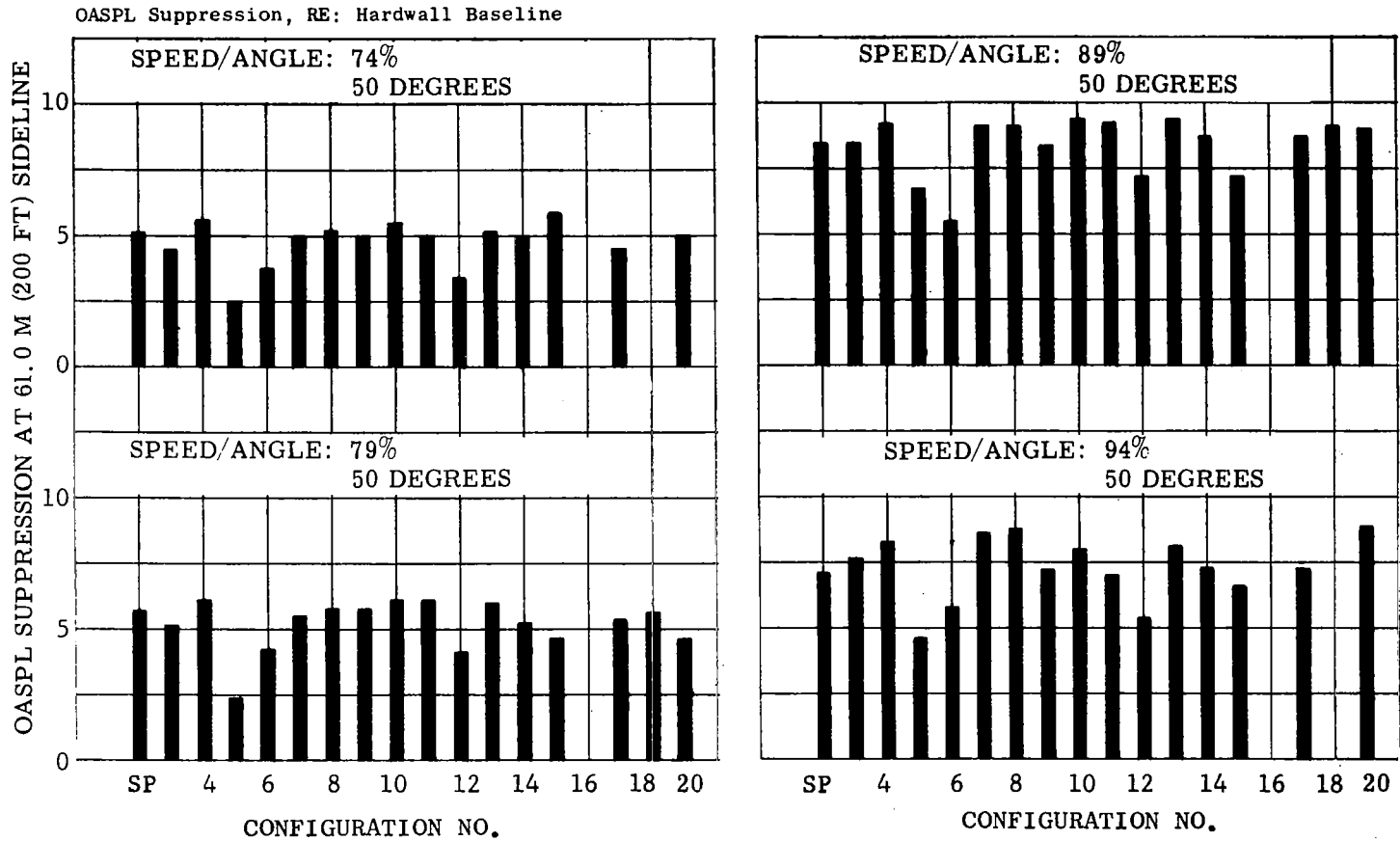


Figure 31. Summary of Phased-Treatment 50° OASPL Suppression at Four Fan Speeds.

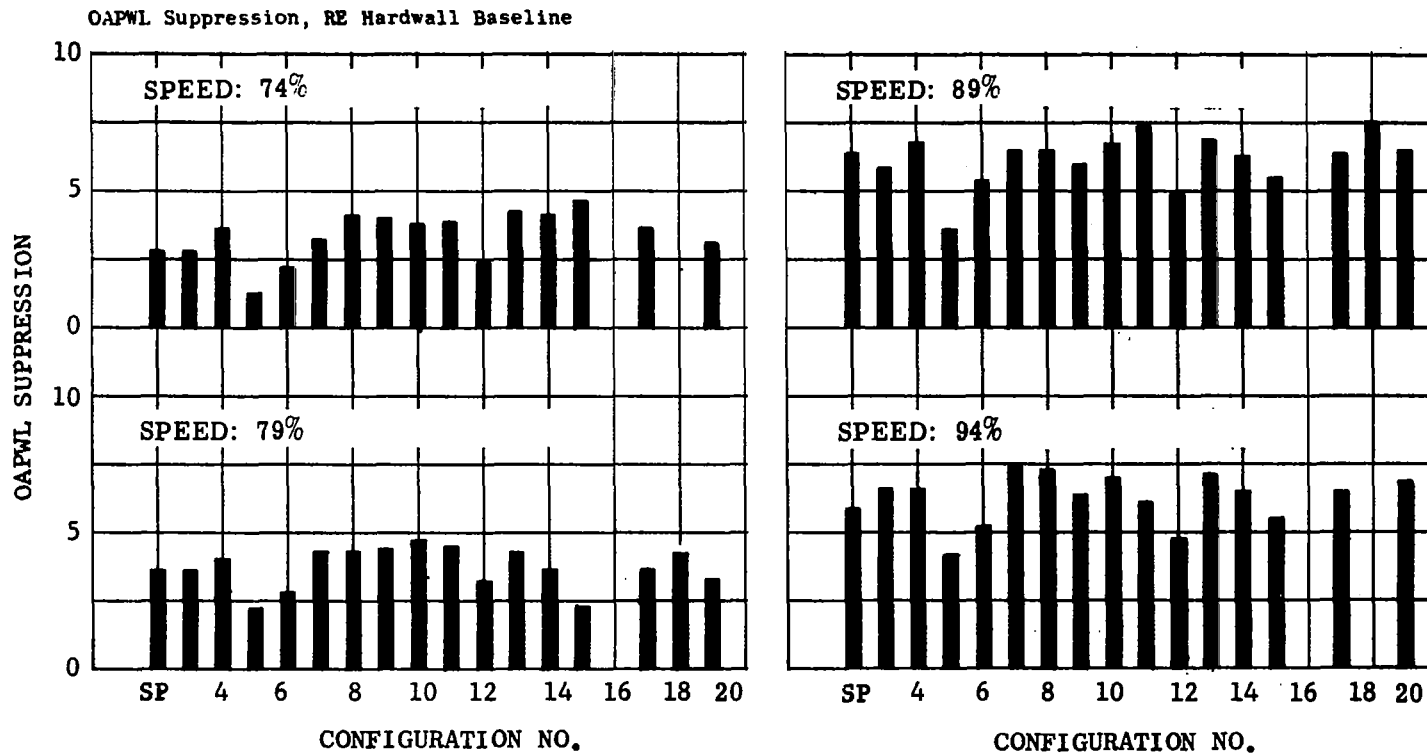


Figure 32. Summary of Phased-Treatment OAPWL Suppression at Four Fan Speeds.

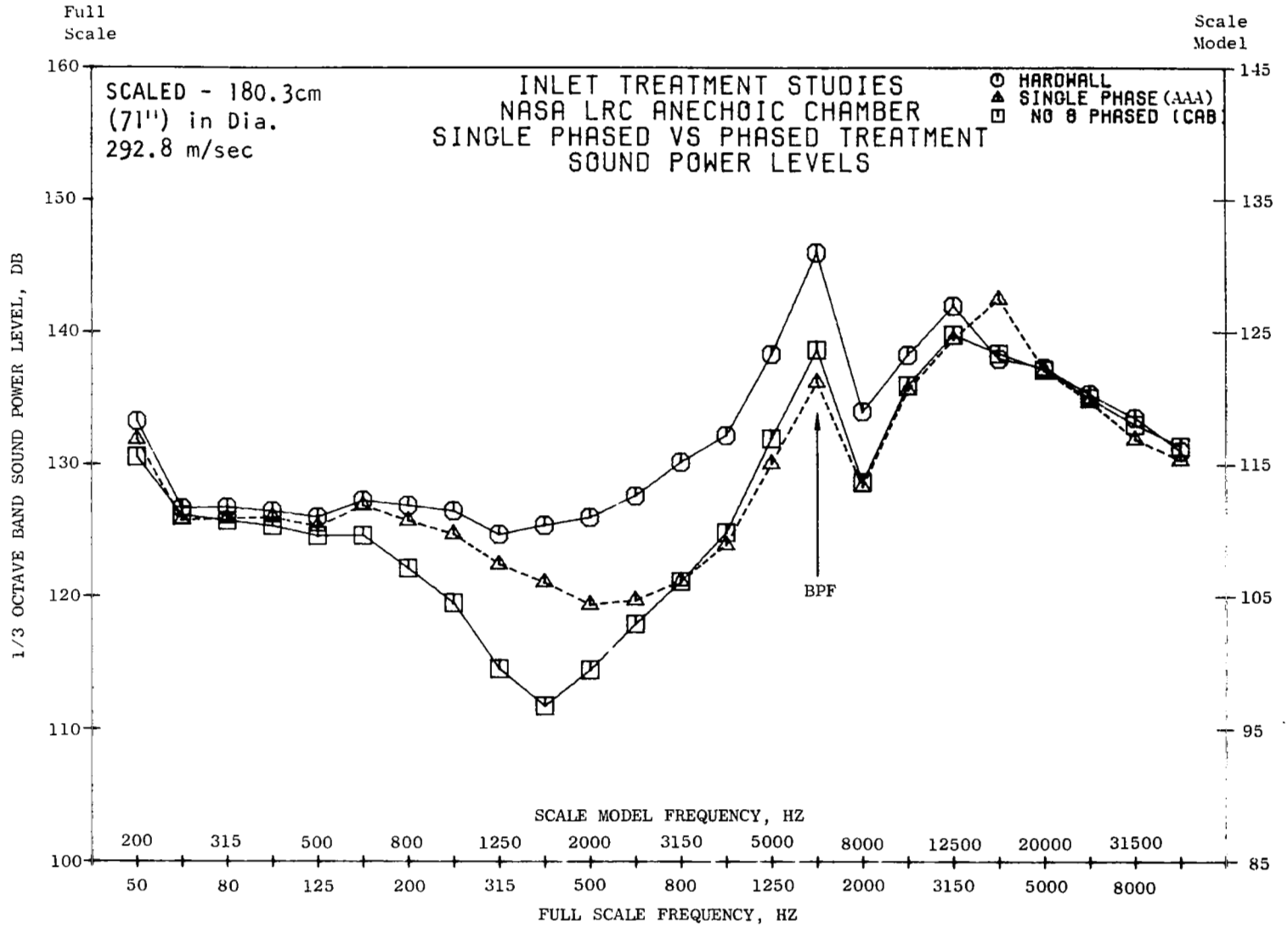


Figure 33. Representative Phased-Treatment Sound Power Level at 74% N_{FC}.

The Perceived Noise Levels were largely controlled by the second harmonic and adjacent bands. Particularly significant for the single-phase treatment was the band immediately above the second harmonic, in which the power level was about 5 dB above the levels of the other two configurations. The increased OASPL's (Figure 34) and PNL's (Figure 35) for the single phase, from 60° to 80°, were due to the high noise levels in this one band. At all of the more-forward angles the OASPL and PNL for the two treated configurations were nearly the same. The maximum levels for both the hardwall and the phased (No. 8) configurations occurred at 50°. Reductions of 5.2 dB OASPL and about 4 PNdB relative to the hardwall were measured at this angle.

A comparison of the hardwall and the single-phase narrowband (50 Hz bandwidth) spectra at 50° is presented in Figure 36. At frequencies up to and including the second harmonic, the uniform treatment has produced substantial suppression. However, between the second and third harmonics, the broadband level of the single-phase configuration has increased above that of the hardwall, and an unidentified tone is present. Although the cause is unknown, several important characteristics of the increased noise were determined from additional narrowband results. First, the frequency of the tone increased as the fan speed increased; in fact, the frequency of the tone between 44% and 79% fan speed appeared to increase linearly with the velocity of the flow over the treatment. Second, the phenomena were observed whenever two "A" panels were installed in adjacent positions. An additional observation was that, at the high frequencies in question, the 1/3-octave levels were based primarily on the level of the broadband noise, not the tone. The noise increase thus appears to be due to some unique geometric properties of the "A" inlet liners.

The sound power spectra at 89% fan speed are presented in Figure 37. Multiple-pure-tones (buzzsaw noise) dominate the spectra at this speed. Large power level reductions were achieved through the MPT-dominated frequencies with both treatment configurations. Phased treatment produced more low-frequency suppression, relative to the single-phase, at this speed similar to the behavior observed at lower speeds. A maximum 1/3 octave reduction of 15.5 dB was attained with uniform treatment in the 800* Hz band while a maximum of 18 dB was achieved in the 630* Hz band with the typical phased treatment. The BPF was reduced by just over 8 dB with phased treatment, about 2 dB less than with uniform treatment. The lower OASPL (Figure 38) and PNL (Figure 39) values for the phased treatment are due to the differences observed in the 4000* Hz and 5000* Hz bands. At 50° 8.5 dB OASPL and 6 PNdB reduction were achieved with the phased treatment.

In summary, the effects of the phased treatment relative to uniform treatment, as tested in this program, were: (1) the phased treatment provided substantially more suppression, 10 dB PWL or more, in the low frequency range (peaking in the vicinity of D/λ of 1.1 to 1.4); and, (2)

*Full-scale frequency.

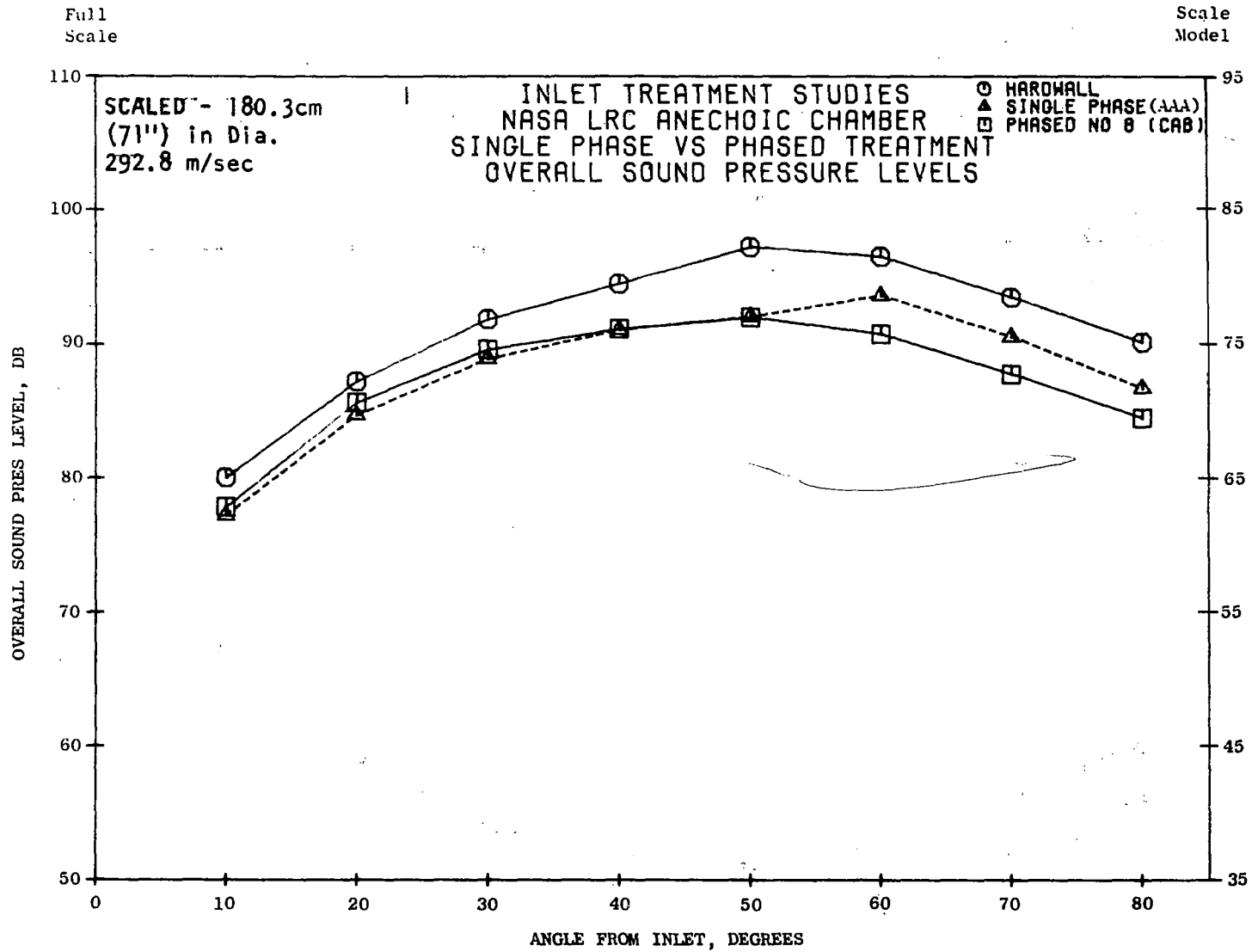


Figure 34. Representative Phased-Treatment OASPL Directivity at 74% NFC.

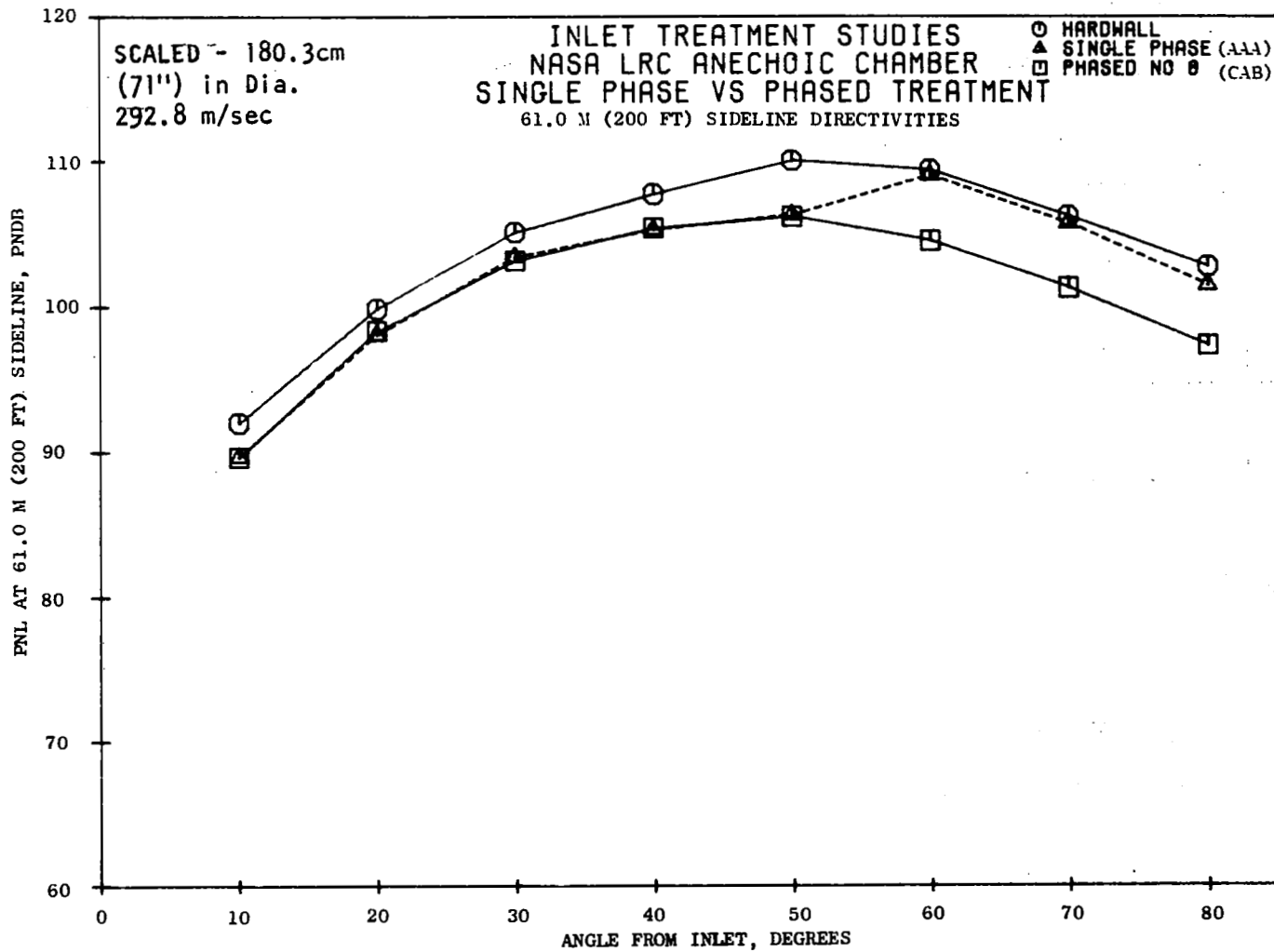


Figure 35. Representative Phased-Treatment PNL Directivity at 74% NFC.

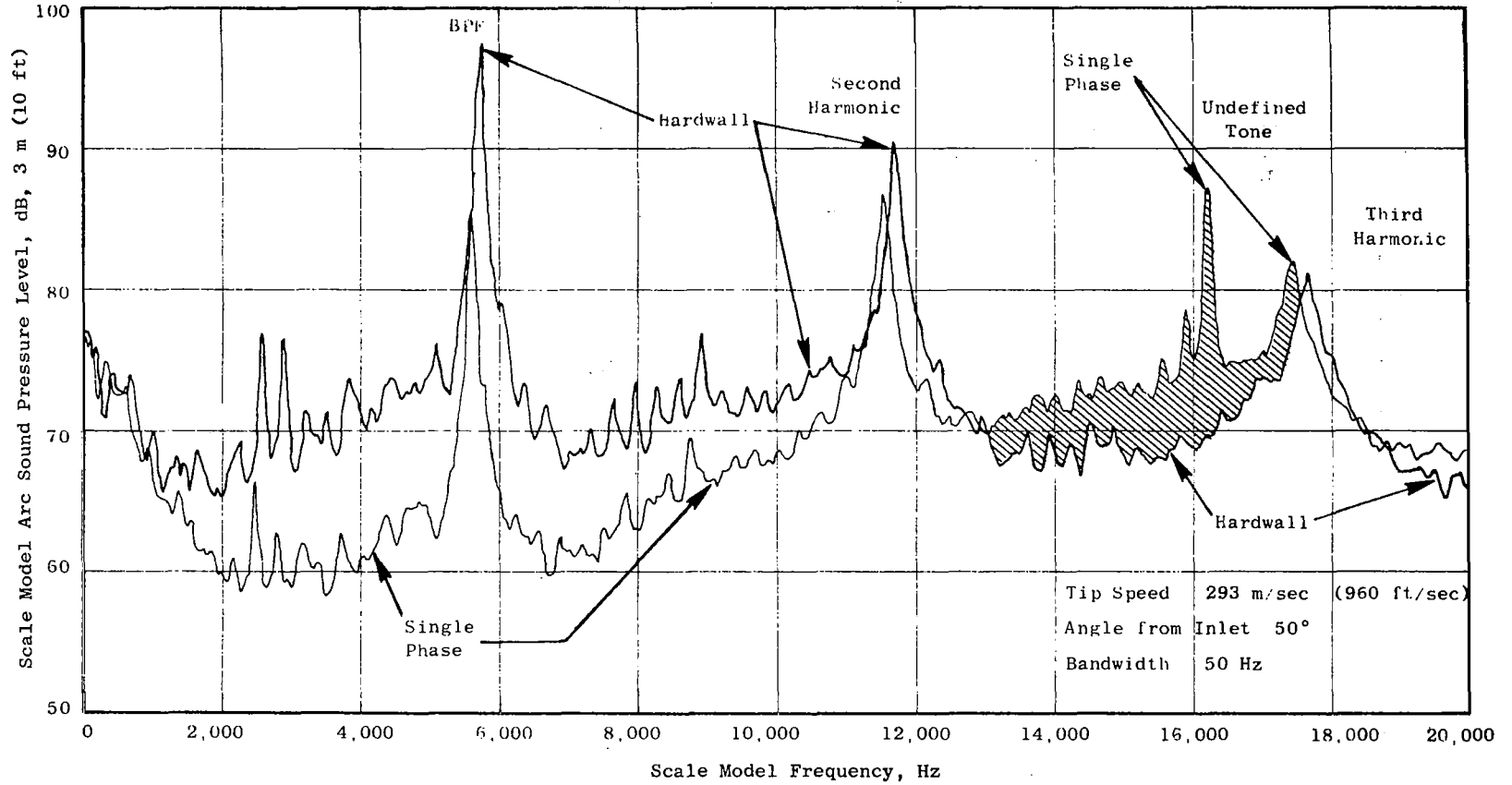


Figure 36. Comparison of Single-Phase and Hardwall 50° Far-Field Narrowband at 74% N_{FC} .

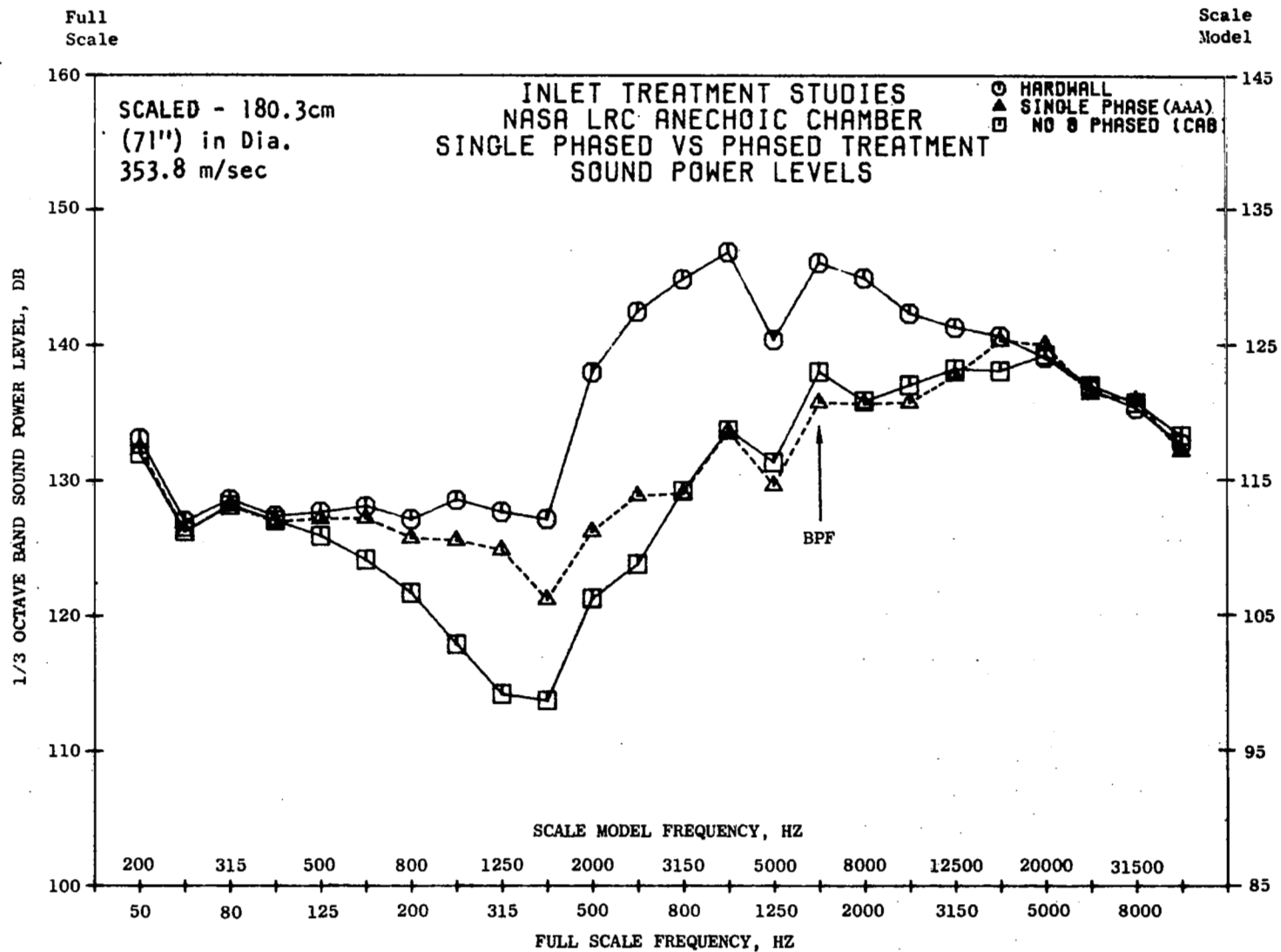


Figure 37. Representative Phased-Treatment Sound Power Level at 89% N_{FC}.

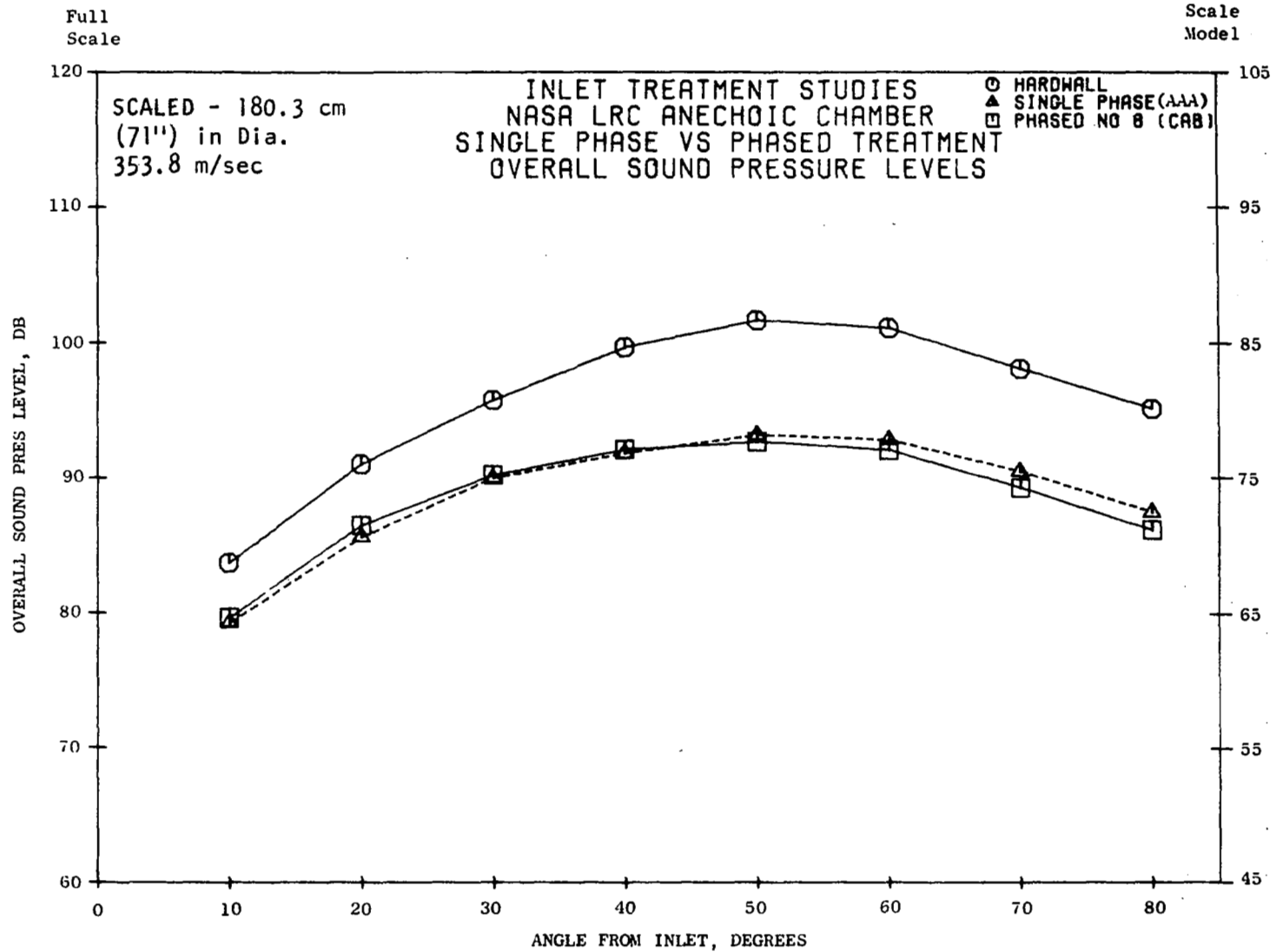


Figure 38. Representative Phased-Treatment OASPL Directivity at 89% N_{FC} .

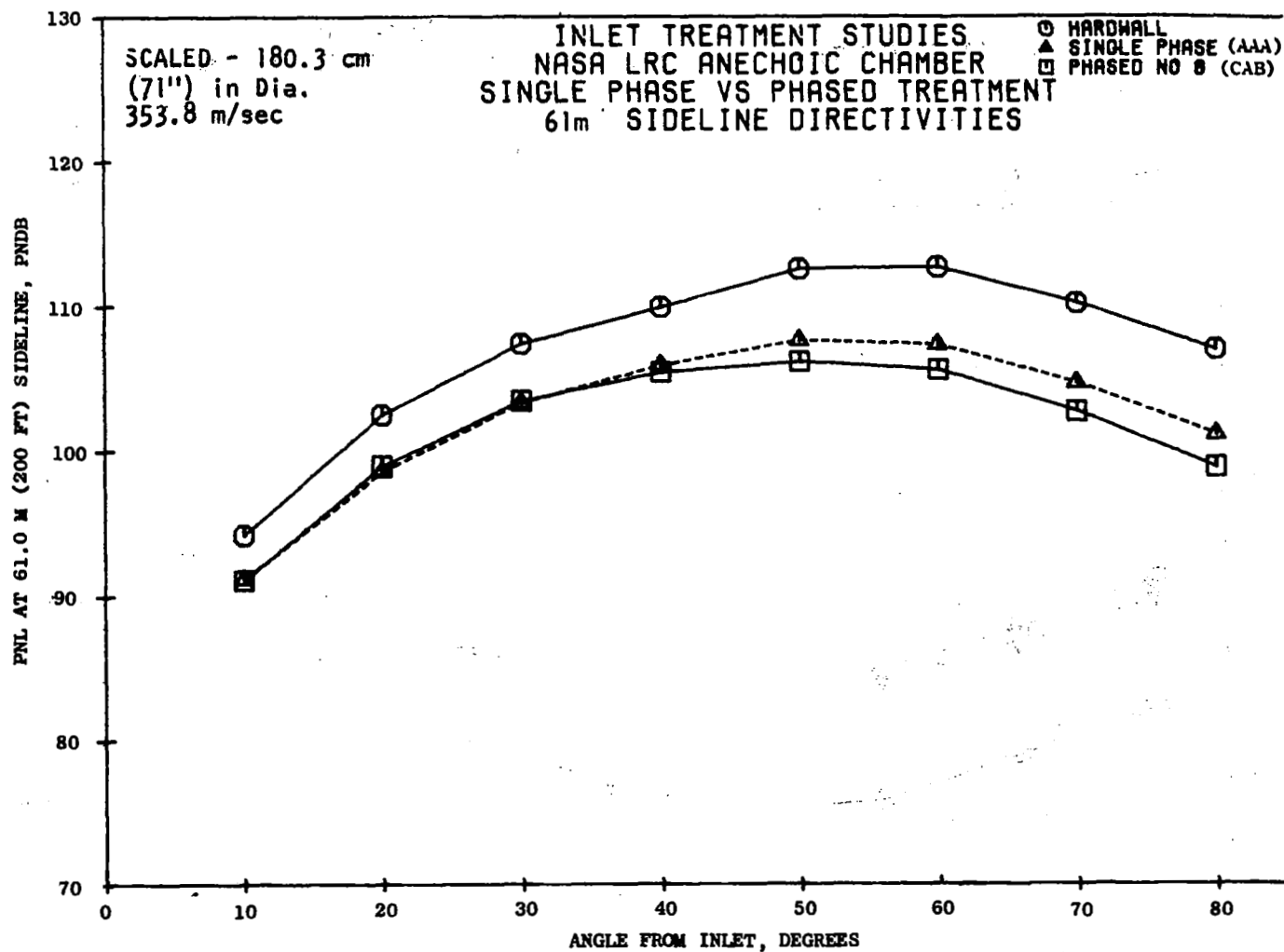


Figure 39. Representative Phased-Treatment PNL Directivity
 at 89% N_{FC} .

although two of the three liners tuned to the blade passing frequency were replaced with liners tuned to lower frequencies, the loss of suppression in the BPF 1/3 octave band was generally less than 20% (i.e., a loss generally less than 2 dB out of 10).

The effect upon 1/3 octave sound power spectra as a result of changing the liner faceplate porosity from 10% to 25% in all three panels is shown in Figure 40 for 74% rpm and in Figure 41 for 89% rpm; these data are for configurations No. 3 (ABC) of 10% porosity and No. 5 (DEF) of 25% porosity, both of which are ramped in thickness with the thickest piece adjacent to the rotor. The figures show that at both speeds, greater suppression was obtained with the lower porosity; this advantage extended over almost the entire frequency range of interest. Similar results were obtained when the sequence of the panel thicknesses was reversed as in Configuration 4 (CBA) and 8 (FED). With regard to the 1/3 octave band containing BPF, Table VII summarized the results for these configurations at 74, 79, 89, and 94% rpm. The table shows that the benefit from the lower porosity case occurs consistently at all speeds and regardless of whether the panel cavity depth was ramped with the thicker end toward the rotor, or vice-versa.

When only one of the three panels was changed from 10 to 25% porosity, the change in suppression was smaller (as might be expected), and it was now inconsistent; sometimes more suppression was obtained and sometimes less, even though the changes were small: this is shown quantitatively in Table VIII. The gain occurred only when the change was made in the thickest panel and when this panel was closest to the rotor.

6.2.2 Comparison of Results With Predictions

The computer program, ACTAMD, was used to predict suppression using the in-duct modal measurements as defined in Section 6.1.2 to specify the source characteristics. Since the modal measurement was made at only one radius, it was necessary to make an assumption with regard to the content at the source plane, namely that only the least attenuated radial mode was present. The source plane was taken to be in the hardwall section directly downstream of the treatment. Additional assumptions were that the spinning mode content was unaffected by the presence of duct treatment and that the effects of reflected waves were negligible. The first-radial-mode-only assumption simplified the application of the modal measurement, since the measured value could be applied directly to one mode, rather than distributing the energy in some fashion among several modes. In the next section, the results of a sensitivity study provides some insight into the effects of participation of higher order radial modes. The predictions for the treated duct confirmed the assumptions that the amplitude of backward traveling waves at the source plane were small.

In addition to the modal inputs to the program, it is necessary to provide the acoustic impedance of the treatment at the wall; the data presented in Section 5.1.4 was used. The results are calculated at discrete

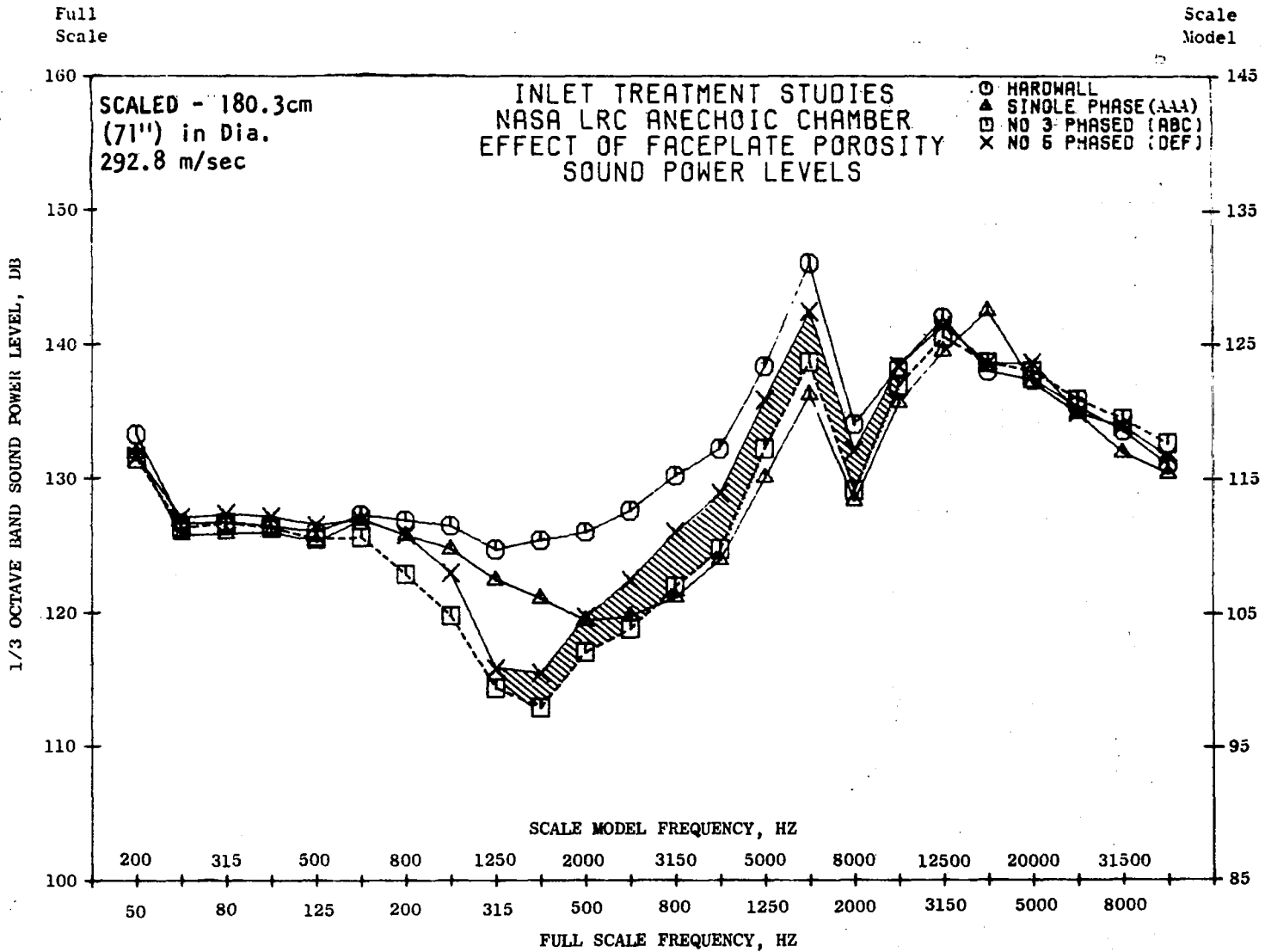


Figure 40. Sound Power Level Spectra for Four Cylinder Inlet Configurations, 74% of Design Speed.

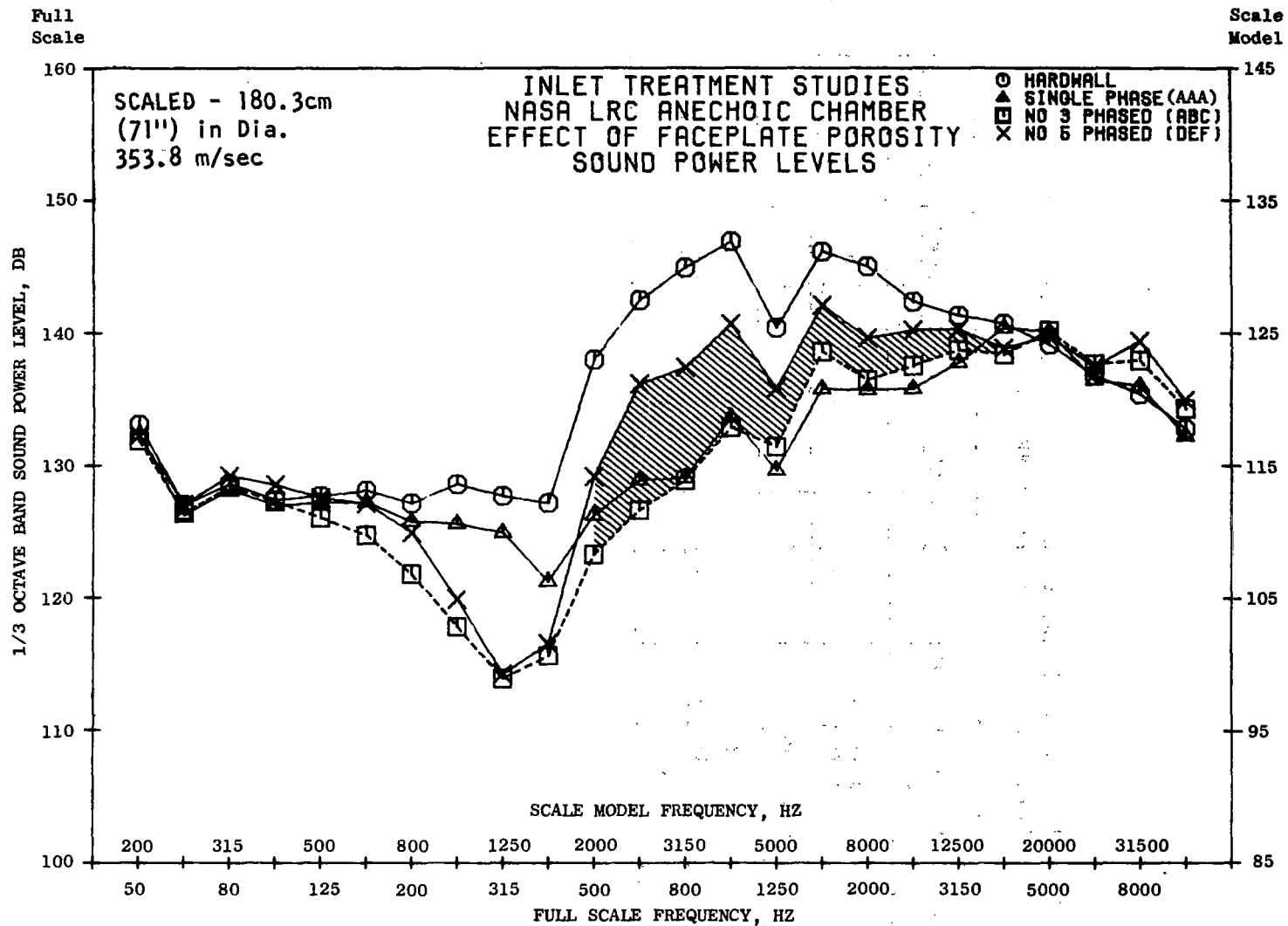


Figure 41. Sound Power Level Spectra for Four Cylindrical Inlet Configurations, 89% of Design Speed.

Table VII. Effect of Changing Porosity in All Panels: One-Third Octave PWL Suppression at BPF, dB.

Porosity %	Configuration No. (Panel)	Percent of Design Speed, % N_{FC}			
		74	79	89	94
10	3 (ABC)	7.3	7.4	7.6	8.4
25	<u>5 (DEF)</u>	<u>3.5</u>	<u>4.3</u>	<u>4.1</u>	<u>4.9</u>
	Difference	3.8	3.1	3.5	3.5
10	4 (CBA)	7.2	7.8	9.1	8.2
25	<u>8 (FED)</u>	<u>5.2</u>	<u>4.9</u>	<u>5.5</u>	<u>6.3</u>
	Difference	2.0	2.9	3.6	1.9

Table VIII. Effect of Changing Porosity in One Panel Only: One-Third Octave PWL Suppression at BPF, dB.

Porosity for Panel X/Y/Z (%)	Configuration No. (Panel)	Percent of Design Speed, %N _F _C			
		74	79	89	94
10/10/10 25/10/10	7 (BAC)	7.7	8.1	7.8	8.8
	<u>14 (EAC)</u>	<u>7.1</u>	<u>5.9</u>	<u>7.1</u>	<u>7.4</u>
	Difference	0.6	2.2	0.7	1.4
10/10/10 10/25/10	3 (ABC)	7.3	7.4	7.6	8.4
	<u>15 (AEC)</u>	<u>6.6</u>	<u>5.4</u>	<u>6.0</u>	<u>6.7</u>
	Difference	0.7	2.0	1.6	1.7
10/10/10 10/10/25	8 (CAB)	8.0	7.9	8.1	9.1
	<u>20 (CAE)</u>	<u>7.2</u>	<u>6.0</u>	<u>6.8</u>	<u>8.0</u>
	Difference	0.8	1.9	1.3	1.1
10/10/10 10/10/25	13 (AAC)	9.2	8.2	8.8	8.8
	<u>11 (AAF)</u>	<u>8.3</u>	<u>8.8</u>	<u>9.9</u>	<u>8.6</u>
	Difference	0.9	-0.6	-1.1	0.2
10/10/10 10/10/25	7 (BAC)	7.7	8.1	7.8	8.8
	<u>10 (BAF)</u>	<u>8.1</u>	<u>8.7</u>	<u>8.7</u>	<u>8.8</u>
	Difference	-0.4	-0.6	-0.9	0
10/10/10 10/10/25	3 (ABC)	7.3	7.4	7.6	8.4
	<u>9 (ABF)</u>	<u>8.1</u>	<u>8.5</u>	<u>7.9</u>	<u>8.6</u>
	Difference	-0.8	-1.1	-0.3	-0.2

frequencies, using the continuity of particle displacement boundary condition assumption.

The analysis was exercised for all treatment configurations which were tested, but numerical problems were encountered. Table IX summarizes those configurations which were calculated successfully and those which were unsuccessful (at least for one spinning-mode order). Note that all those treatment configurations having low resistance faceplates were unsuccessful.

The unsuccessful cases were traced to a problem with the occurrence of "double eigenvalues" (two eigenvalues with exactly the same value) as determined by the eigenvalue-search algorithm of the program. These double-eigenvalues occur when the program, starting from two different hardwall roots as initial estimates, follows integration convergence paths which lead to the same final value. The nature of this problem is more easily understood from examination of the complex mapping between the eigenvalue and wall admittance (Reference 16). The occurrence of a double-eigenvalue results in a division by zero at a future point in the calculation, which aborts the run.

The discrete frequency predictions for all treatment configurations which could be calculated successfully have been evaluated relative to measured far-field 1/3-octave data for three cases: 44% speed BPF, 44% speed second harmonic, and 79% speed BPF. Data for the 44% speed BPF are presented in Figure 42; the second harmonic data at 44% speed are presented in Figure 43; and, the BPF data at 79% speed are shown in Figure 44. The measured data show ± 1 dB variation, based on an estimate of the approximate variation of the noise for the hardwall configurations.

At 44% speed blade passing frequency (Figure 42) the agreement for treatment Configurations ABC, CAJ, and AAC is within the measurement accuracy. Configurations AAA and AAH are overpredicted by about 50%.

For both the 44% second harmonic (Figure 43) and the 79% blade passing frequency (Figure 44) cases, there is a general trend toward underprediction of the measured results. Based on the sensitivity study which follows, the most plausible explanation for this underprediction is the neglect of higher-order radial modes in the source definition. In both cases, there is some indication that the analytical program correlates with the suppression trend of the treatment configurations, although the differences among the measured values for these cases is not great. Unfortunately, the low resistance liner configurations, which did show significant differences in measured suppression values, could not be calculated due to numerical difficulties.

The data indicate that the simplifying assumptions in the analysis must be removed. In particular, the sensitivity study in the following section indicates that more complete radial mode information is required to achieve significant improvements. Also, it is possible that the effects of boundary layers must be incorporated to achieve satisfactory results.

Table IX. Occurrence of Double Eigenvalues in Suppression Prediction Calculations.

Configuration	Treatment Panel Designation	44% BPF	44% 2nd Harm.	79% BPF
2	AAA			
3	ABC			
4	CBA			
5	DEF	DEV	DEV	DEV
6	FED	DEV	DEV	DEV
7	BAC			
8	CAB	DEV		
9	ABF	DEV	DEV	DEV
10	BAF	DEV	DEV	DEV
11	AAF	DEV	DEV	DEV
12	AAH			
13	AAC			
14	EAC	DEV	DEV	DEV
15	AEC	DEV	DEV	DEV
17	AAB	DEV		

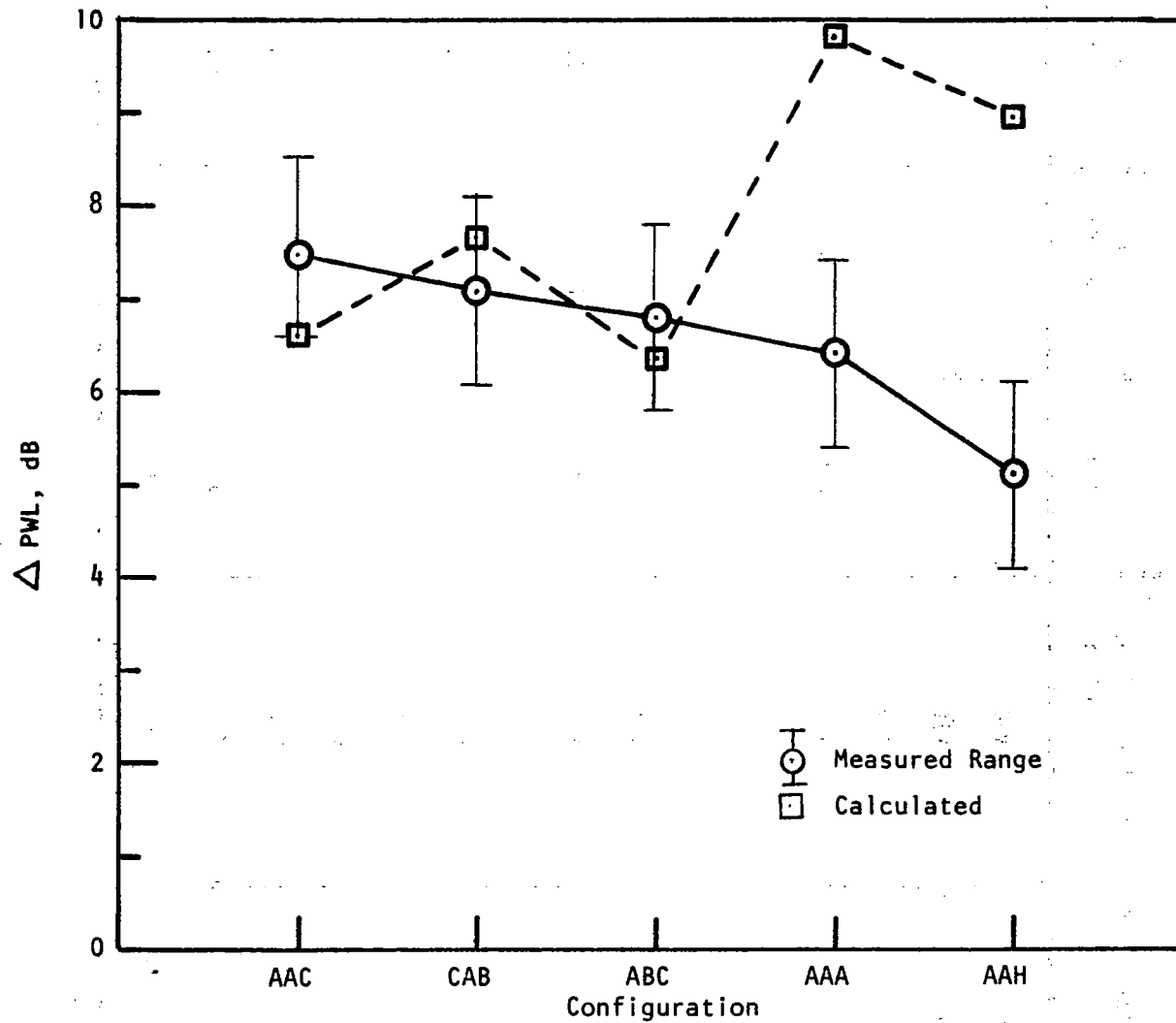


Figure 42. Comparison of Measured and PredictedSuppressions, 44% Speed, Blade Passing Frequency.

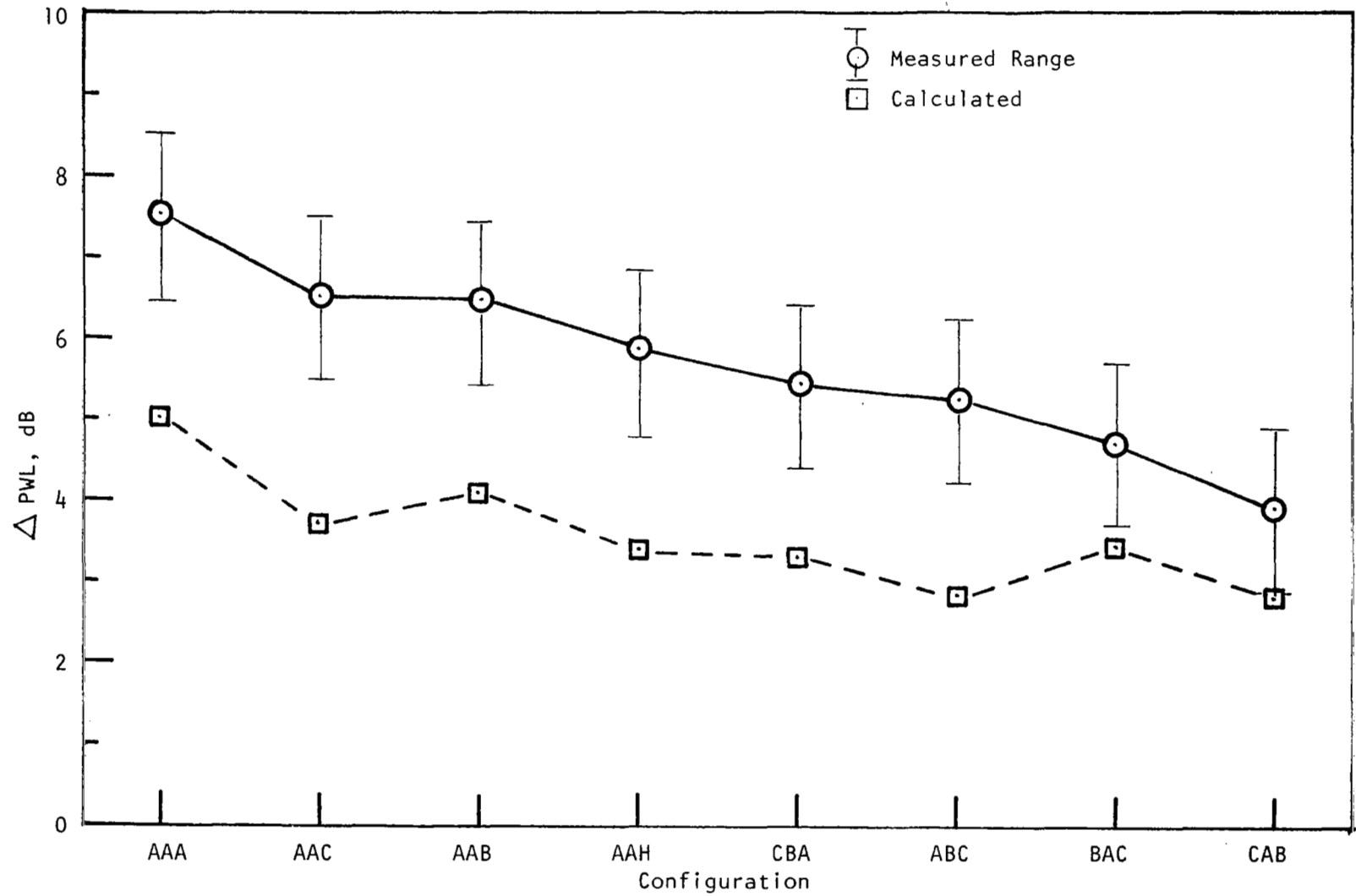


Figure 43. Comparison of Measured and PredictedSuppressions, 44% Speed, Second Harmonic.

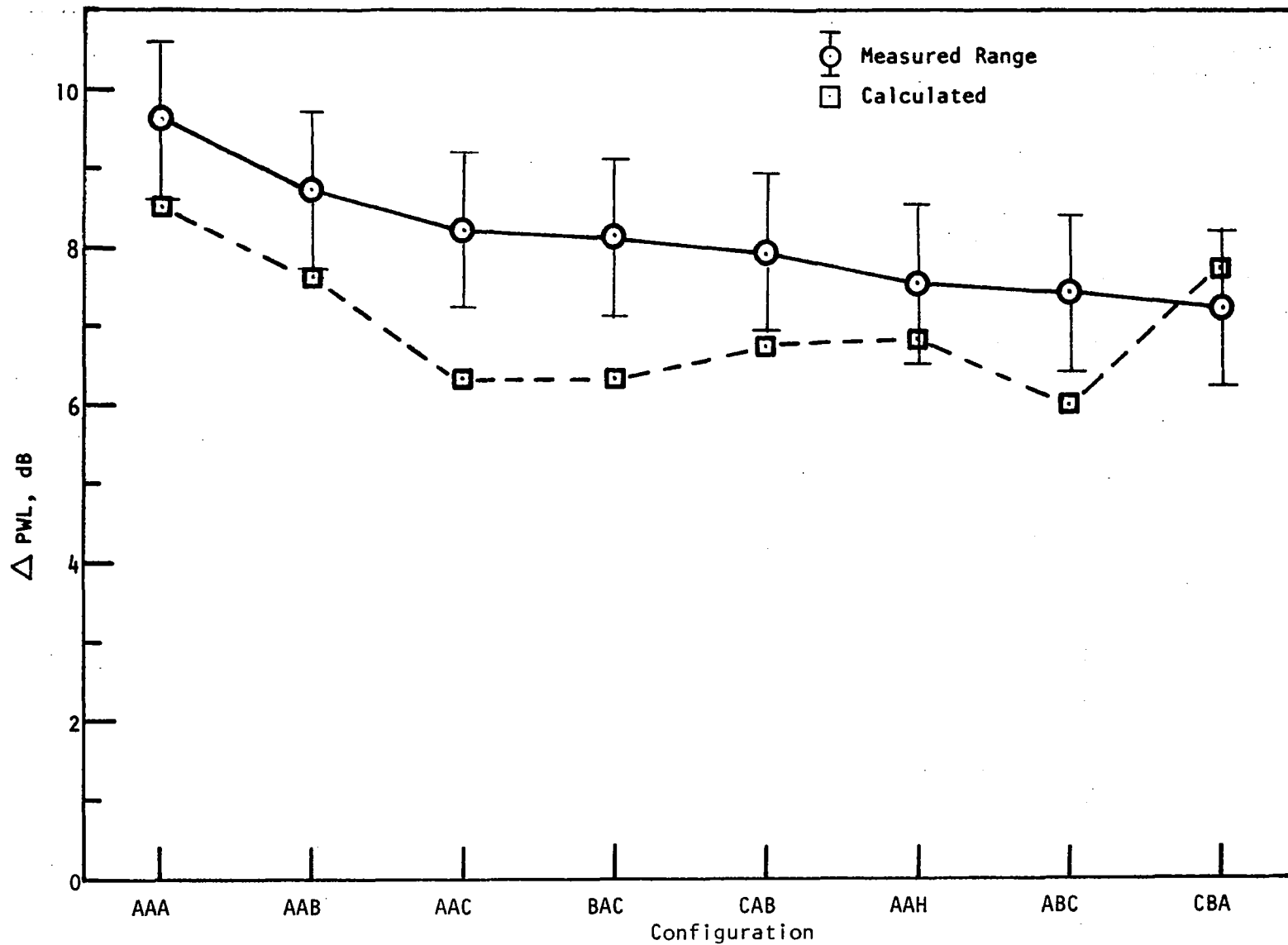


Figure 44. Comparison of Measured and PredictedSuppressions, 79% Speed, Blade Passing Frequency.

6.2.3 Sensitivity Studies

The analytical program was used to study the sensitivity of the predicted suppression to the resistance of the liners and to the effects of radial-mode content.

Figures 45 and 46 are plots of the variation of suppression with liner resistance for the single-phase configuration (AAA) at 44% speed for the blade passing frequency and second harmonic, respectively. The suppression curve for the second harmonic passes through the measured value of suppression at a resistance of about 1.24 ρc . (It should be noted that a preliminary modal measurement result was used for this calculation, such that the mode weighting differ somewhat from the final values used for the correlation of measurement and theory, but the suppression trends should be unaffected by the spinning mode weighting variation.)

The data in both Figures 45 and 46 indicate that the suppression could be increased by using higher resistance. (The relative "flatness" of the curve at 3440 Hz (Figure 45) compared to 6920 Hz (Figure 46) is a result of the fact that the reactance at 3440 Hz is further from the optimum value than it is at 6920 Hz).

The suppression for the BPF at 79% speedcase was calculated using a number of different radial-mode content assumptions, in order to determine the sensitivity of the suppression to radial-mode content. The calculations were made using a nominal impedance value of $Z/\rho c = 1.2 - 0.7i$ for the single phase (AAA) treatment configuration.

The first assumption is that only the lowest order radial mode for each spinning-mode order is present at the input plane to the treatment (softwall source-plane assumption). The spinning modes are weighted by the preliminary modal measurement results. The second assumption is that the lowest order radial mode only is present in a hardwall source plane adjacent to the first treatment section. This hardwall mode redistributes into three radial modes at the input plane of the treated section. Generally, large energy flux mismatches occurred at the source plane. The third assumption was the same as the second except that the hardwall mode was redistributed into five softwall radial modes for each spinning mode. This decreased the energy mismatch by providing better convergence. The fourth assumption was to give the first six radial modes for each spinning mode an equal weighting of 1.0 + 0.0i. The spinning modes were not weighted by modal measurement in this case.

The results of the calculations, including suppressions for each spinning mode order, are presented in Table X. The hardwall source case with improved convergence provides an exact match to the measured suppression value. However, the sensitivity to radial mode content, as well as the sensitivity to relative phasing between the modes, suggests that this agreement is somewhat fortuitous, and, in general, without experimental information as to radial mode content, the agreement could be expected to be no better than roughly ± 3 dB.

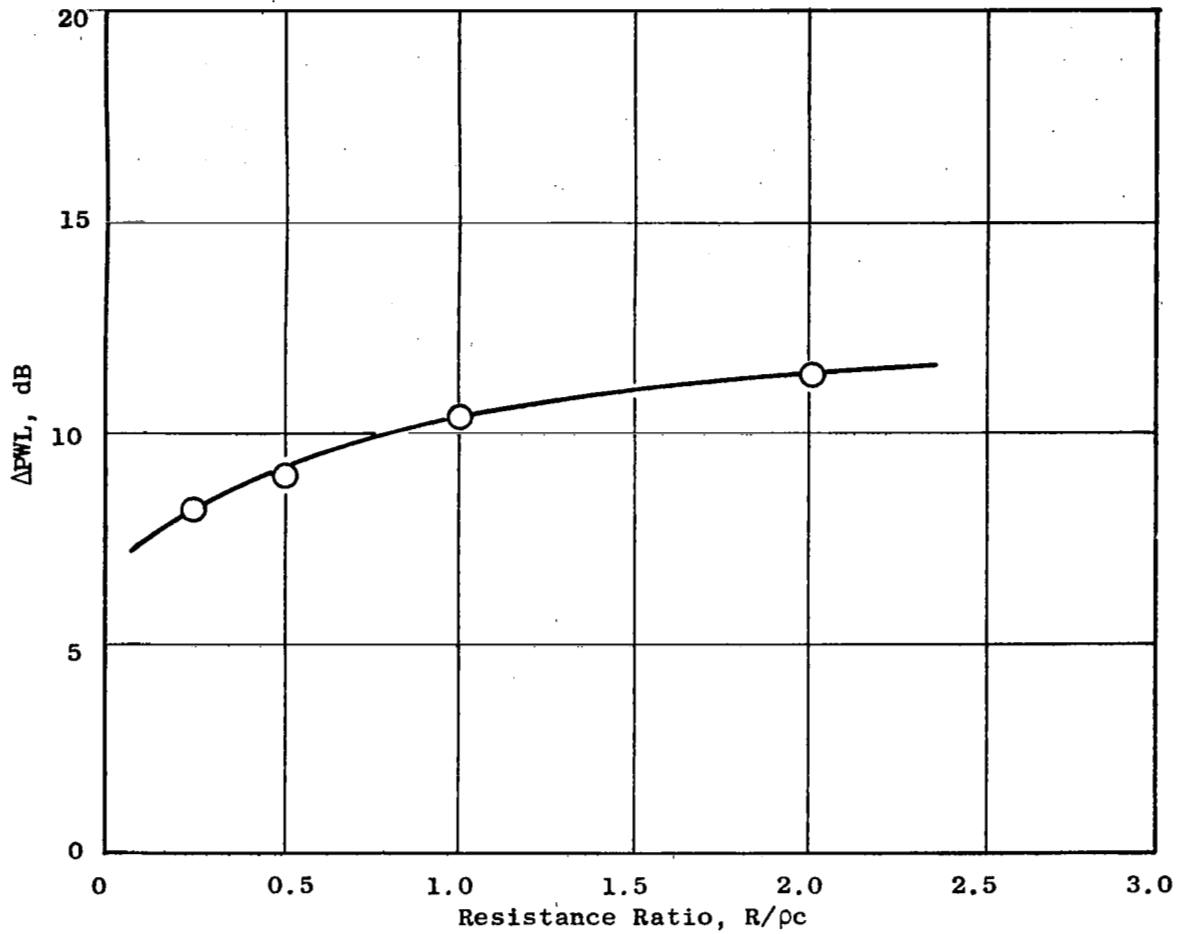


Figure 45. Predicted Suppression of Configuration AAA, 44% Speed, 3440 Hz, as a Function of Liner Resistance.

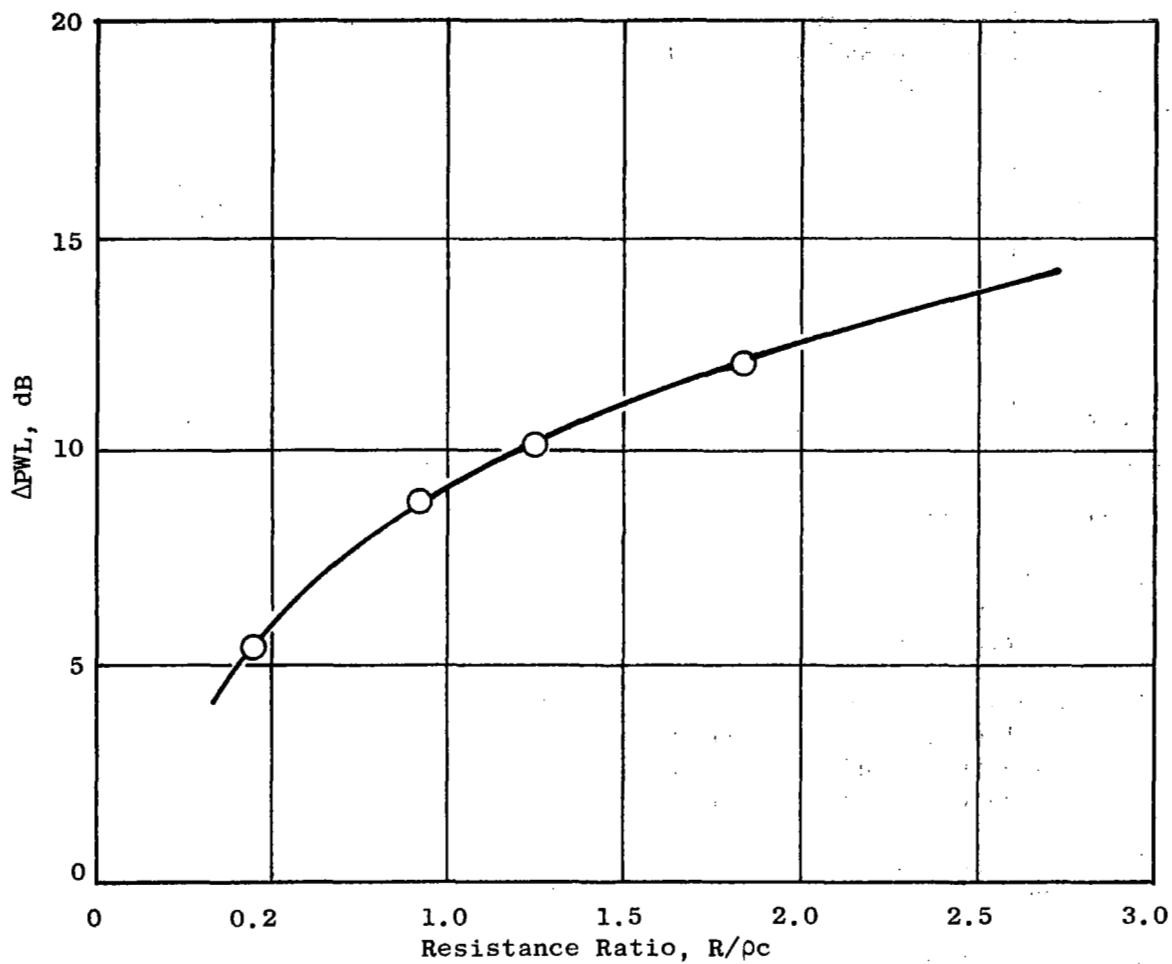


Figure 46. Predicted Suppression of Configuration AAA, 44% Speed, 6920 Hz, as a Function of Liner Resistance.

Table X. Effect of Radial-Mode Content.

• Single-Phase Treatment $\eta = 5.4$ $L/H = 1.0$

m	Number of Cut-on Radial Modes	<u>ΔPWL, dB</u>			
		1	2	3	4
1	5	- 0.7	- 6.7	- 3.3	?
4	4	- 3.3	- 9.0	- 5.8	-10.2
5	4	- 4.6	-10.1	- 7.2	-12.6
6	3	- 6.4	-10.9	- 8.4	-15.6
7	3	- 8.7	-13.1	-10.0	-17.3
9	2	-16.4	-18.9	-18.1	-25.3
11	2	-35.9	-35.1	-34.7	-44.1
<u>12</u>	1	<u>-65.8</u>	<u>-66.4</u>	<u>-66.3</u>	<u>-74.1</u>
Overall		- 7.2 dB	-11.7 dB	- 9.2 dB	-15 dB

Radial-Mode Assumptions:

- 1 Only lowest order radial mode for each spinning-mode order present at input to treated section. Spinning modes weighted by modal measurement.
- 2 Lowest order radial mode for each spinning-mode order in hard-wall section, weighted by modal measurement. Redistributes into three radial modes at input to softwall. Large energy mismatch at source plane.
- 3 Same as 2 but redistributes into five radial modes, improving source-plane mismatch.
- 4 First six radial modes given equal weighting of 1.0. Spinning modes not weighted by modal measurement.

The overall suppression calculated in each case for comparison with measurement is based on contributions from a fairly large number of spinning modes, each with some assumed but unknown radial mode content. The number of cut-on radial modes at a given frequency for each spinning mode decreases as spinning mode order increases. Table XI lists the number of cut-on radial modes for the dominant spinning mode orders for the 44% speed, second harmonic and the 79% speed, blade passing frequency cases. The difficulty arises in trying to infer the particular weighting and relative phase of the radial modes from the measurement at a single radius, two inches from the wall in the twelve inch diameter duct. Since the amount each mode participates at the measurement radius will be weighted by the amplitude of its mode shape at that radius, it is of interest to examine plots of the mode shapes for various spinning mode orders.

Figure 47 shows the shapes of the first five radial modes for $m=1$, the shapes of the first three modes for $m=7$, and the shapes of the first two modes for $m=12$. Very little can be inferred from the $m=1$ radial mode shapes, other than the fact that any participation by the fifth order mode would not show up at the measurement radius, since it is near a null at that point. For $m=7$ and $m=12$, however, it is interesting to note that the amplitude of the first mode at the measurement radius is very much less than the second, so that the measured participation at that point was probably due to the participation of the second order mode. The participation of the first order mode, which is very likely to be present, is, therefore, difficult to infer from the measurement at this one immersion, requiring at least a second measurement nearer to the wall. In any case, examination of the mode shapes for spinning mode orders greater than about six indicates that the modal measurements obtained at the two inch immersion were most likely to be dominated by the second order radial modes, and gave little information about the participation of the lowest order radial modes.

If nothing else, the above arguments, coupled with the underprediction of suppression for the two higher frequency cases, imply that it might have been more realistic to include higher order radial modes in the source characteristics for those spinning modes above spinning mode order 4 (roughly) which have at least two radial modes cut on. To check this hypothesis, a series of calculations were performed for the 44% speed second harmonic and 79% speed blade passing frequency cases under the following set of assumptions:

- 1) The ratio of the modal amplitudes for the first and second radial modes was determined such that equal energy was contained in each mode.
- 2) The sum of the amplitudes of the first two radial modes was set equal to the measured modal amplitude for each spinning mode of concern, assuming zero relative phase.

These assumptions were applied to the $m = 6, 7, 8, 11,$ and 12 modes in the 44% speed case, and the $m = 6, 7, 9,$ and 11 modes in the 79% speed case. The results of the calculation are presented in Figures 48 and 49.

Table XI. Number of Cut-On Radial Modes for Dominant Spinning Mode Orders.

44% Speed Second Harmonic f = 6920 Hz, Mach 0.2		79% Speed Blade-Passing Frequency f = 6120 Hz, Mach 0.35	
<u>Spinning Mode Order</u>	<u>Number of Cut-On Radial Modes</u>	<u>Spinning Mode Order</u>	<u>Number of Cut-On Radial Modes</u>
1	6	1	6
4	4	2	6
6	3	6	4
7	3	7	3
9	2	8	3
11	2	11	2
12	1	12	2
15	1	13	1

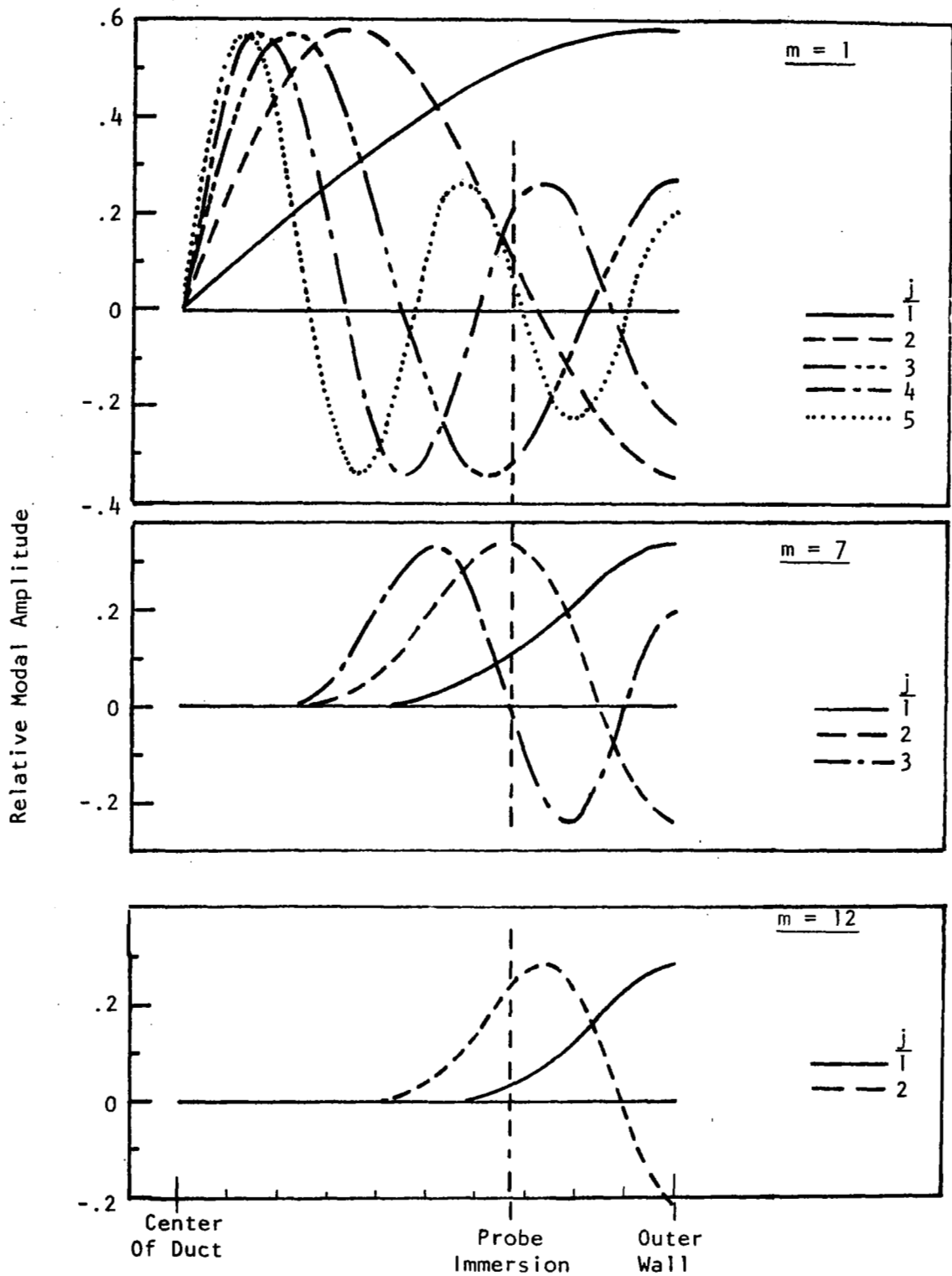


Figure 47. Radial Mode Shapes for Spinning Mode Orders $m = 1, 7,$ and $12.$

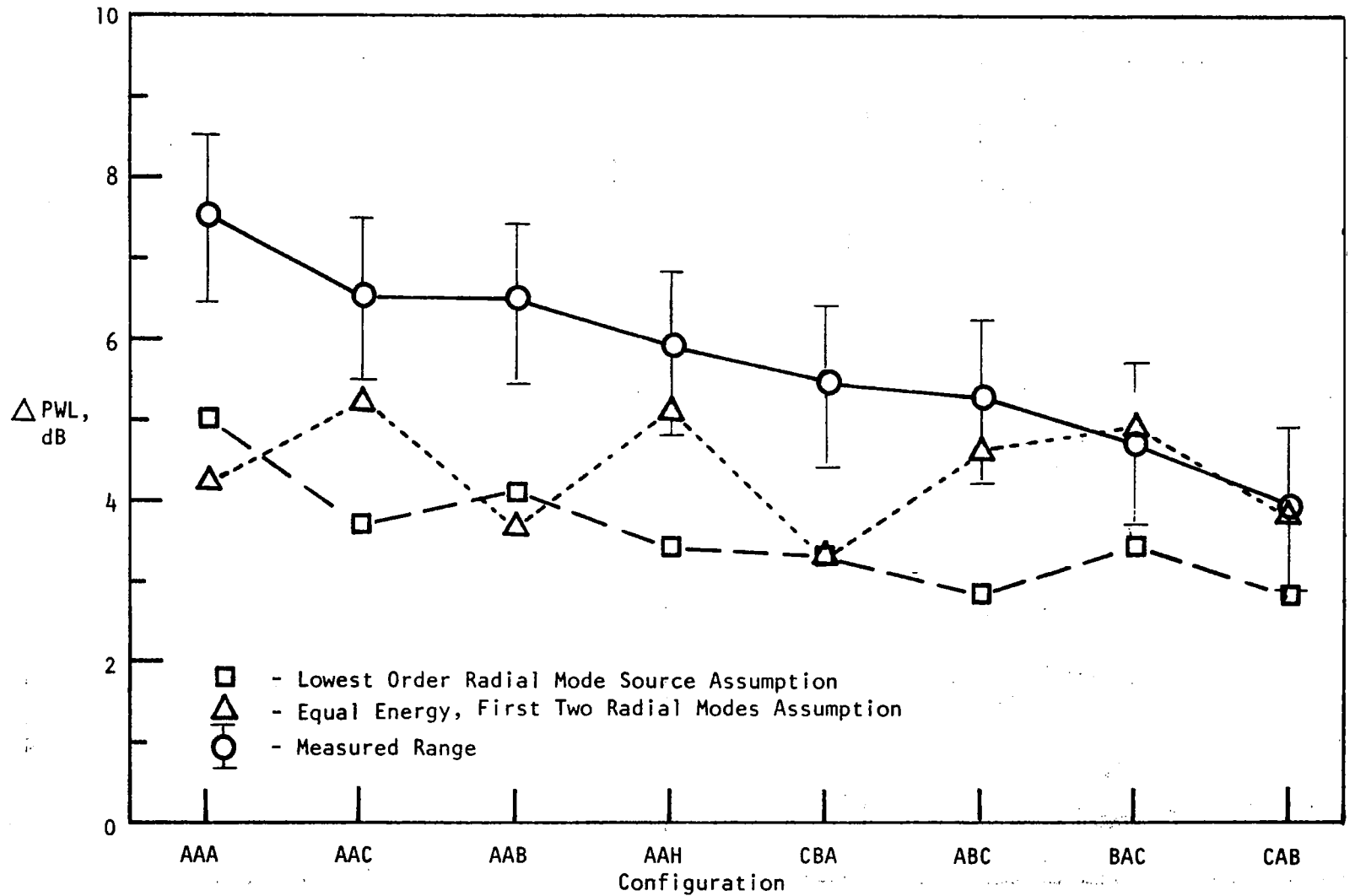


Figure 48. Comparison of Measured and Predicted Suppression for Two Different Modal Source Assumptions, 44% Speed, Second Harmonic.

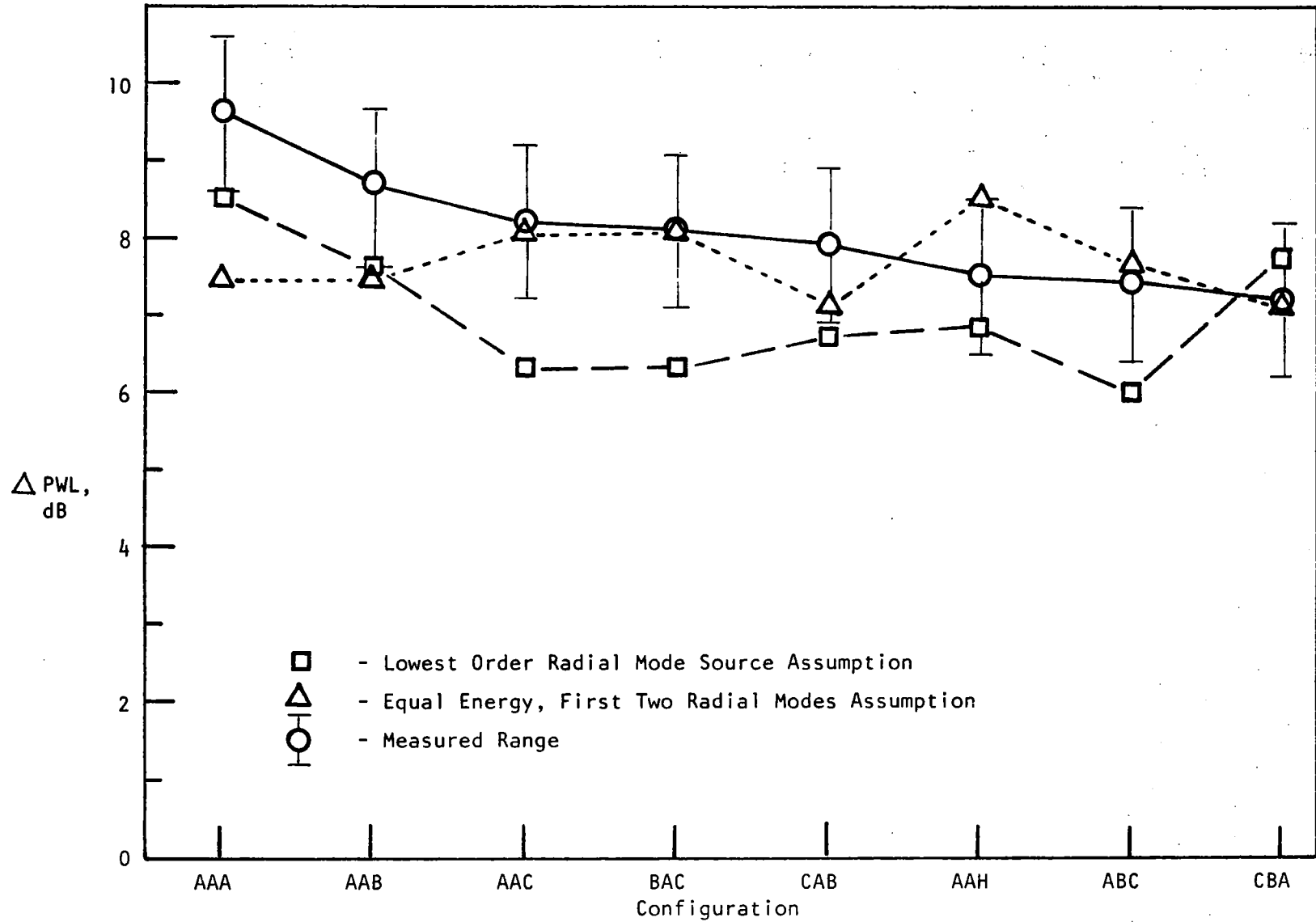


Figure 49. Comparison of Measured and Predicted Suppression for Two Different Modal Source Assumptions, 79% Speed, BPF.

In the 44% speed case, the modified source assumption increased the predicted suppression in all cases except treatment Configurations AAA, CBA, and AAB. Detailed examination of the computer runs indicates that the increases in suppression can be attributed primarily to a redistribution into higher order radial modes for the various spinning mode orders at the interface between the hardwall source plane and the entrance plane at the first liner segment. For the three configurations which were not improved by the new modal assumption, it was found that, in general, the different source profile did not cause a redistribution into higher order modes into the liner than the lowest order mode only cases. One anomaly is that the modified source assumption causes the AAH Configuration to predict higher than the AAA Configuration. The cause of this effect is the relative phase shift that occurs between the first two radial modes in the source along the hardwall segment between the hardwall source plane and the entrance to the first treatment segment. The source profile changes (with no attenuation) along this length in such a manner that a very advantageous redistribution into higher order modes occurs when the wave reaches the treatment. This indicates the importance, not only of the relative weighting among radial modes at the source, but also the relative phasing among the modes.

Results at 79% speed are similar, where again all configurations show increased suppression predictions except AAA, CBA, and AAB. Figure 50 shows a comparison of the (redistributed) modal content for the $m=6$ spinning mode for Configurations AAA and AAH for the equal energy and least attenuated mode source assumptions at the entrance to the first treated section. The higher order radial mode content can be correlated directly with the suppression trends for these configurations. Similar results are found for the $m=7$ and $m=9$ spinning modes.

6.3 HIGH MACH INLET

Acoustic data for the four High Mach inlets defined in Table IV, together with the hardwall cylindrical inlet as a baseline reference, are presented and discussed in this section. The data include 1/3 octave band PWL spectra for the test vehicle as-tested ("scale model") and as scaled to a representative "full scale" size (see Section 5.4); also, it includes the 61 m (200 ft) sideline PNL versus farfield angle for the full scale vehicle size. In addition, acoustic data from probe measurements of the accelerating inlet and the single-phase hybrid inlet are presented to assess the relative roles of flow Mach number and acoustic treatment on the suppression achieved by each mechanism. Aerodynamic performance data for the high Mach inlets are also summarized.

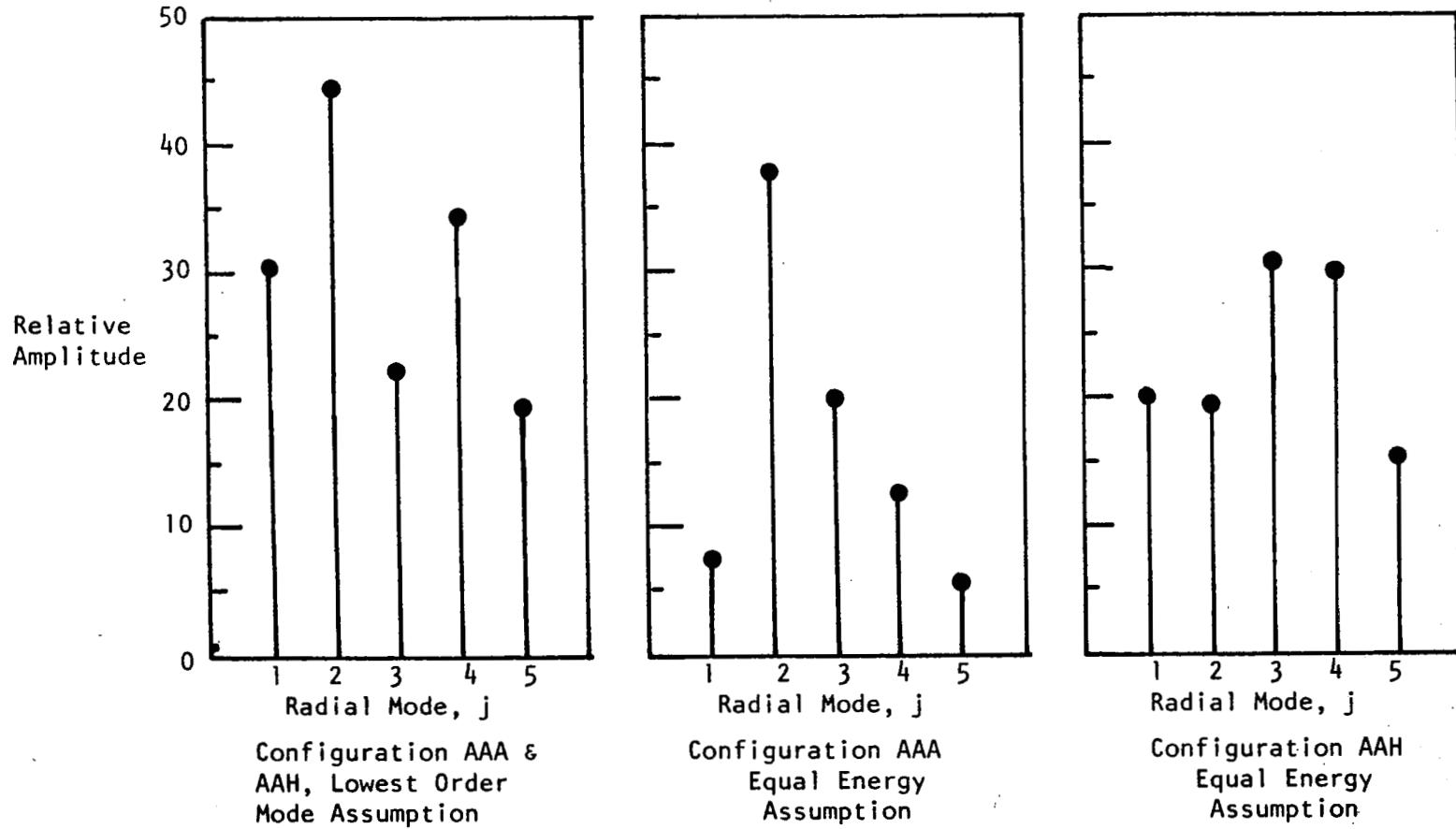


Figure 50. Modal Participation at Entrance to Treated Section (Plane 2), Sixth Order Spinning Mode, 79% Speed, Blade Passing Frequency.

6.3.1 Acoustic Data

One-Third Octave Band PWL Spectra

The effect of vehicle rpm upon the PWL spectra are shown in Figures 51, 52, and 53 for 79, 89, and 94% of design speed, respectively. The data for the accelerating and cylindrical hardwall inlets are essentially the same at the lowest (79%) speed point where the throat Mach number of the accelerating inlet was only 0.60 (versus 0.36 for the cylindrical inlet). At the design point of 89% rpm, the throat Mach number, which has increased to 0.72 (versus 0.40 for the cylindrical inlet), is sufficient to provide 3 to 5 dB reduction in radiated noise over the entire spectrum. At the 94% speed point, the throat Mach number of 0.79 (versus 0.42 for the cylindrical inlet) is adequate to provide between 10 and 15 dB reduction over most of the spectrum.

The addition of the treatment, whether single-phase or multi-phase, provided additional suppression at all these speed points. Again, as with the treated cylindrical inlet (see Section 6.2.1), the characteristic suppressions are such that the multi-phase treatment provides more suppression in the lower end of the frequency range than the single-phase, with only small loss in suppression at BPF - even though only one of the three liners (rather than all three) was tuned for BPF.

61 m (200 ft) Sideline PNL versus Farfield Angle

The 61 m (200 ft) sideline perceived noise levels for these inlets, after scaling to 180 cm (71 in.) size, are presented in Figures 54, 55, and 56 for the same three speed points. Note that the PNL values for the inlets with treatment are, at each speed point, all essentially the same; this is the consequence of the fact that the "full scale" 1/3 octave spectra after being Noy weighted⁽¹⁹⁾, are dominated by the frequency bands above BPF. The differences in PNL values for the hardwall inlets, cylindrical versus accelerating, dramatically indicate the benefit of the suppression achieved by high subsonic-flow Mach number, per se: very little difference occurs at 79% speed; about 6 PNdB advantage occurs at 89%, and this increases to more than 14 PNdB at 94% speed. In this speed range, between 3 to 5 PNdB more suppression occurs with the addition of treatment. On a PNL basis, no benefit is seen as a result of the multiphase treatment relative to the single phase; this is a consequence of the fact that the lower frequency range, where the multiphase treatment showed improved suppression (as indicated in Figures 51 through 53), is de-emphasized by the Noy weighting involved in the PNL calculation.

The data in Figure 57 show the variation of maximum 61 m (200 ft) sideline PNL as a function of vehicle operating speed from 74% through 97.5%. Again, data for five inlets are presented, but this time a treated cylindrical inlet (multiphase treatment configuration CAE) has been substituted for a hybrid (configuration CAB), since the data in the prior three

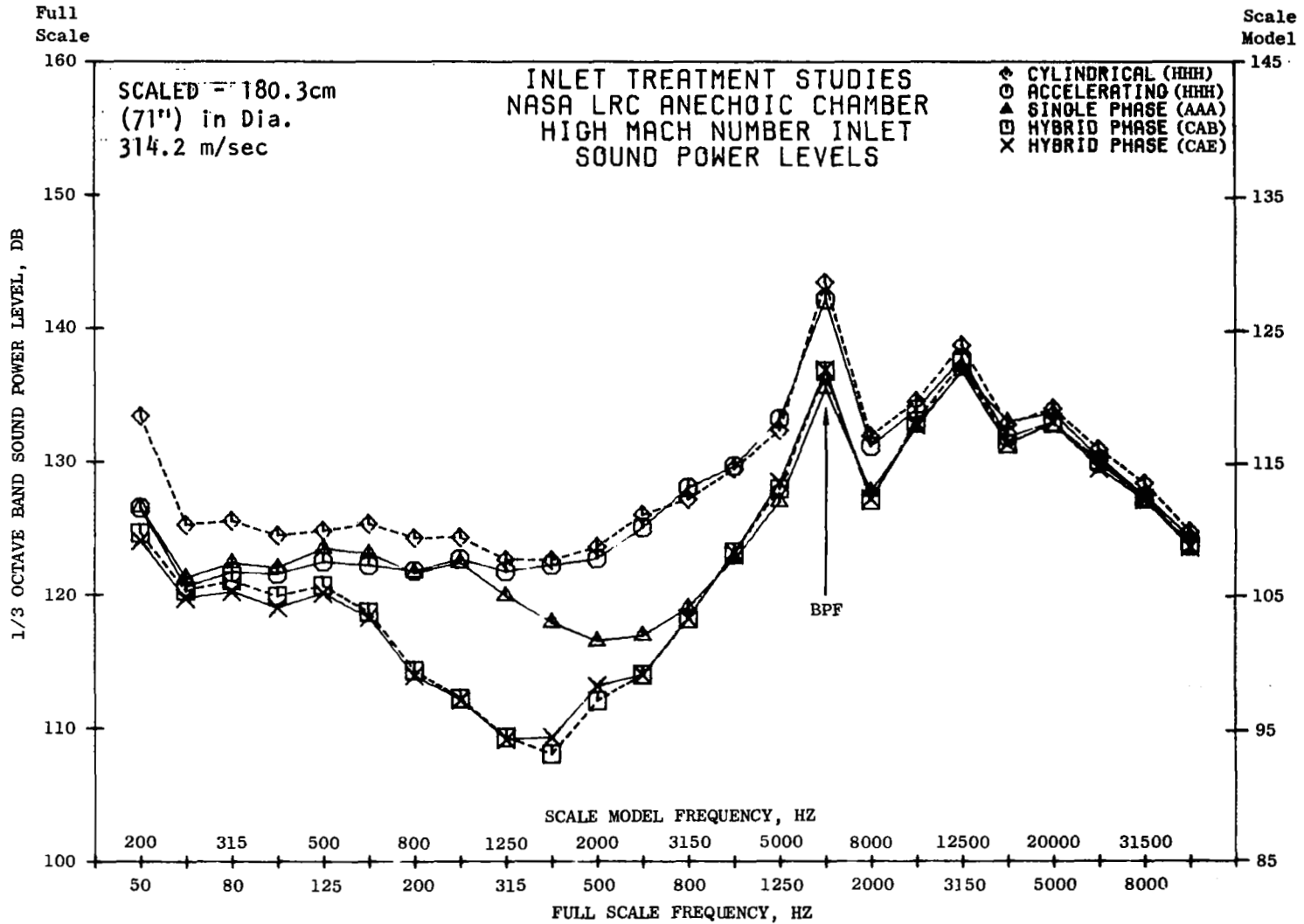


Figure 51. One-Third Octave Band PWL Spectra for Five Inlet Configurations, 79% of Design Speed, $M_{TH} = 0.60$.

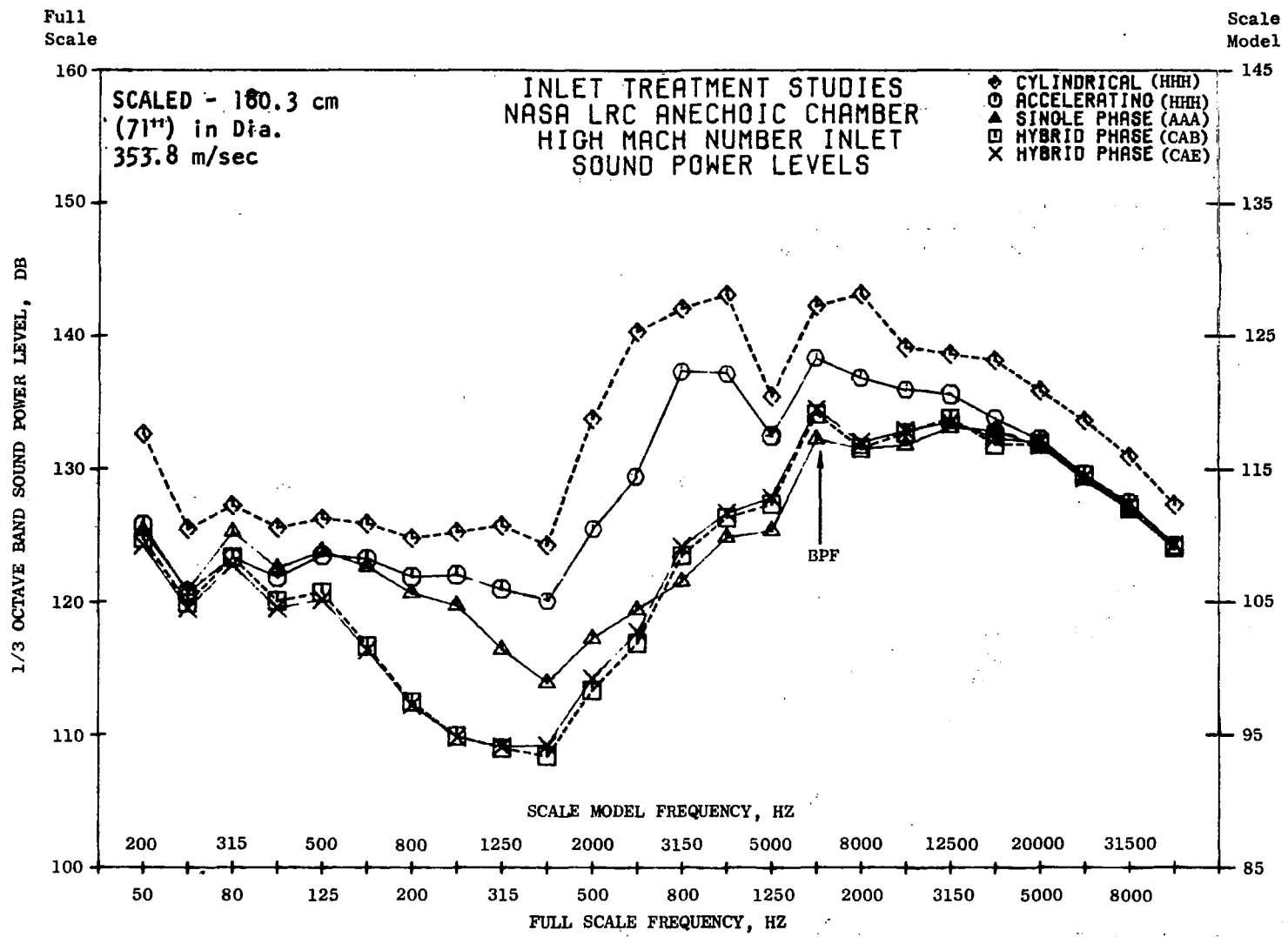


Figure 52. One-Third Octave Band PWL Spectra for Five Inlet Configurations, 89% of Design Speed, $M_{TH} = 0.72$.

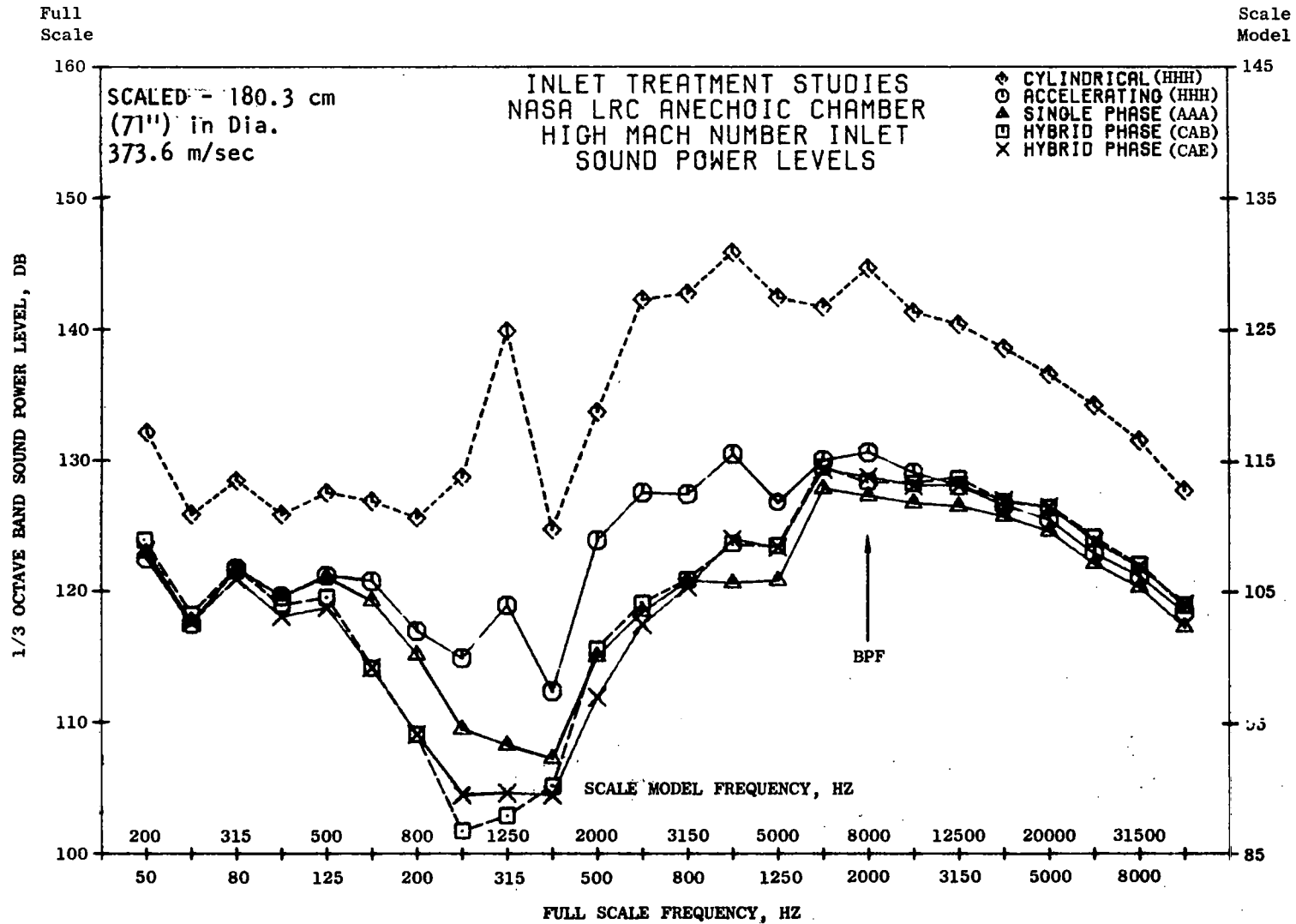


Figure 53. One-Third Octave Band PWL Spectra for Five Inlet Configurations, 94% of Design Speed, $M_{TH} = 0.79$.

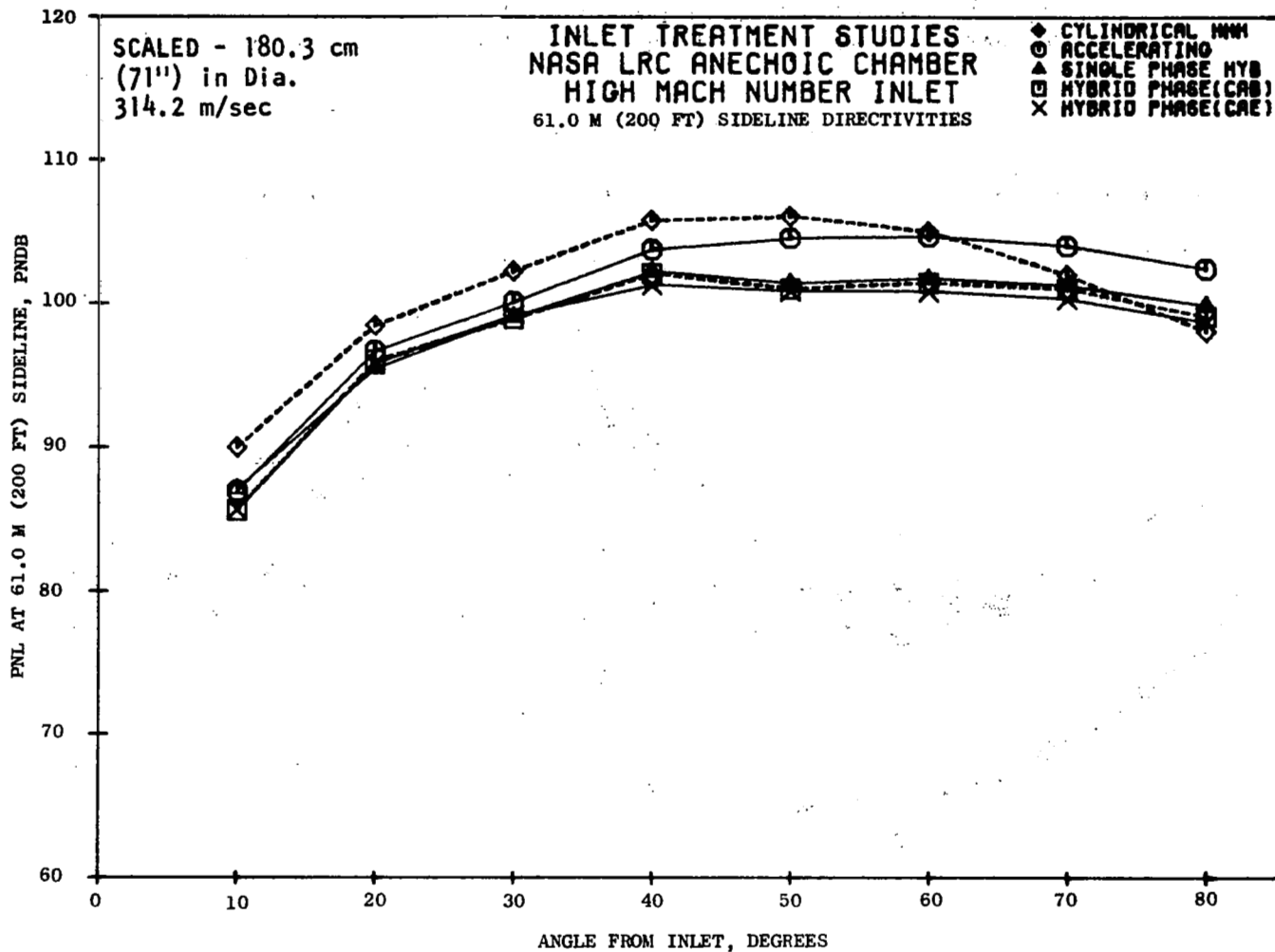


Figure 54. High Mach Number Inlet, PNL Directivities at 79% N_{fC} ($M_{TH} = 0.60$) for Five Inlet Configurations.

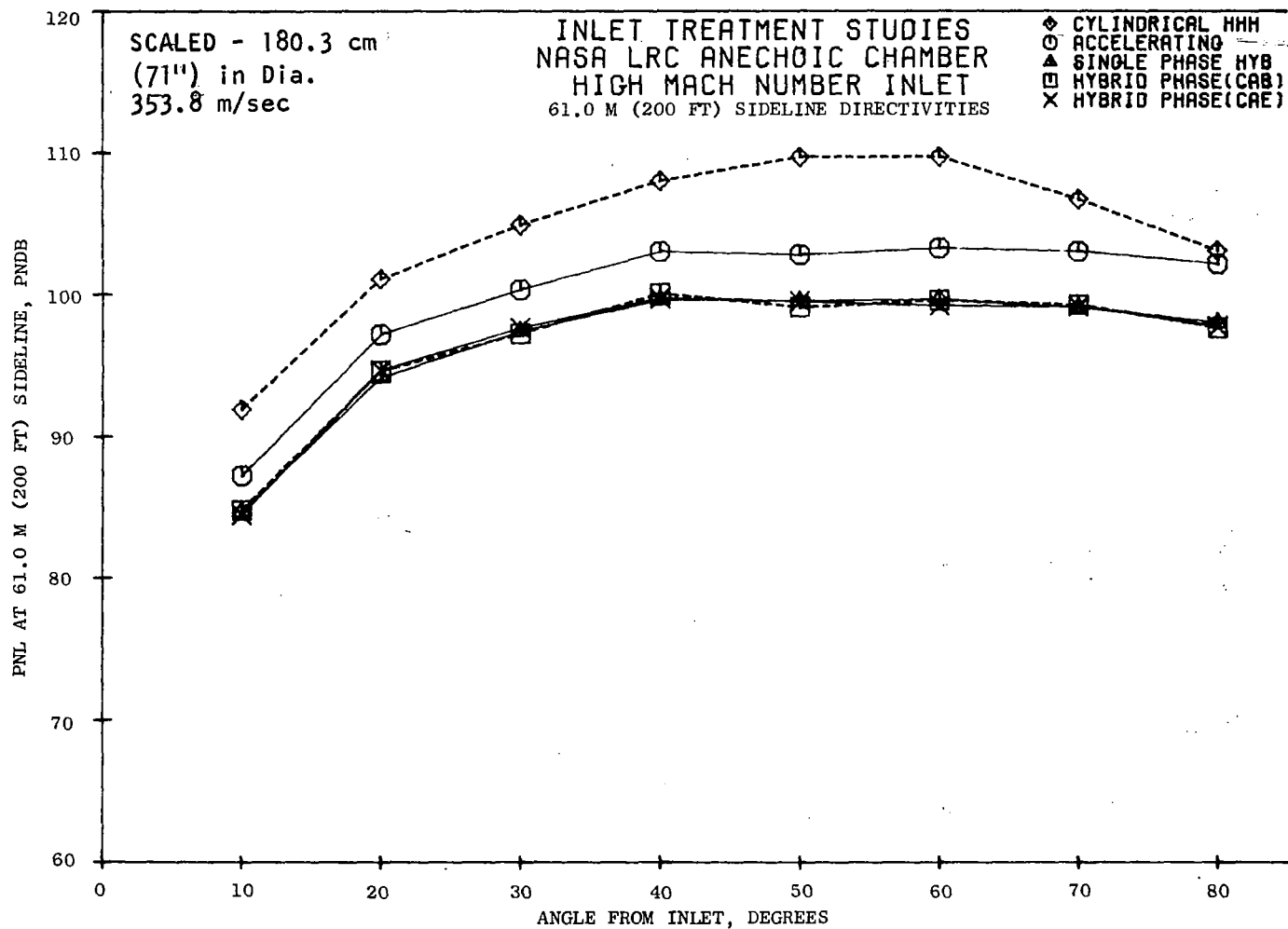


Figure 55. High Mach Number Inlet, PNL Directivities at 89% N_{FC}
($M_{TH} = 0.72$) for Five Inlet Configurations.

CR-2882

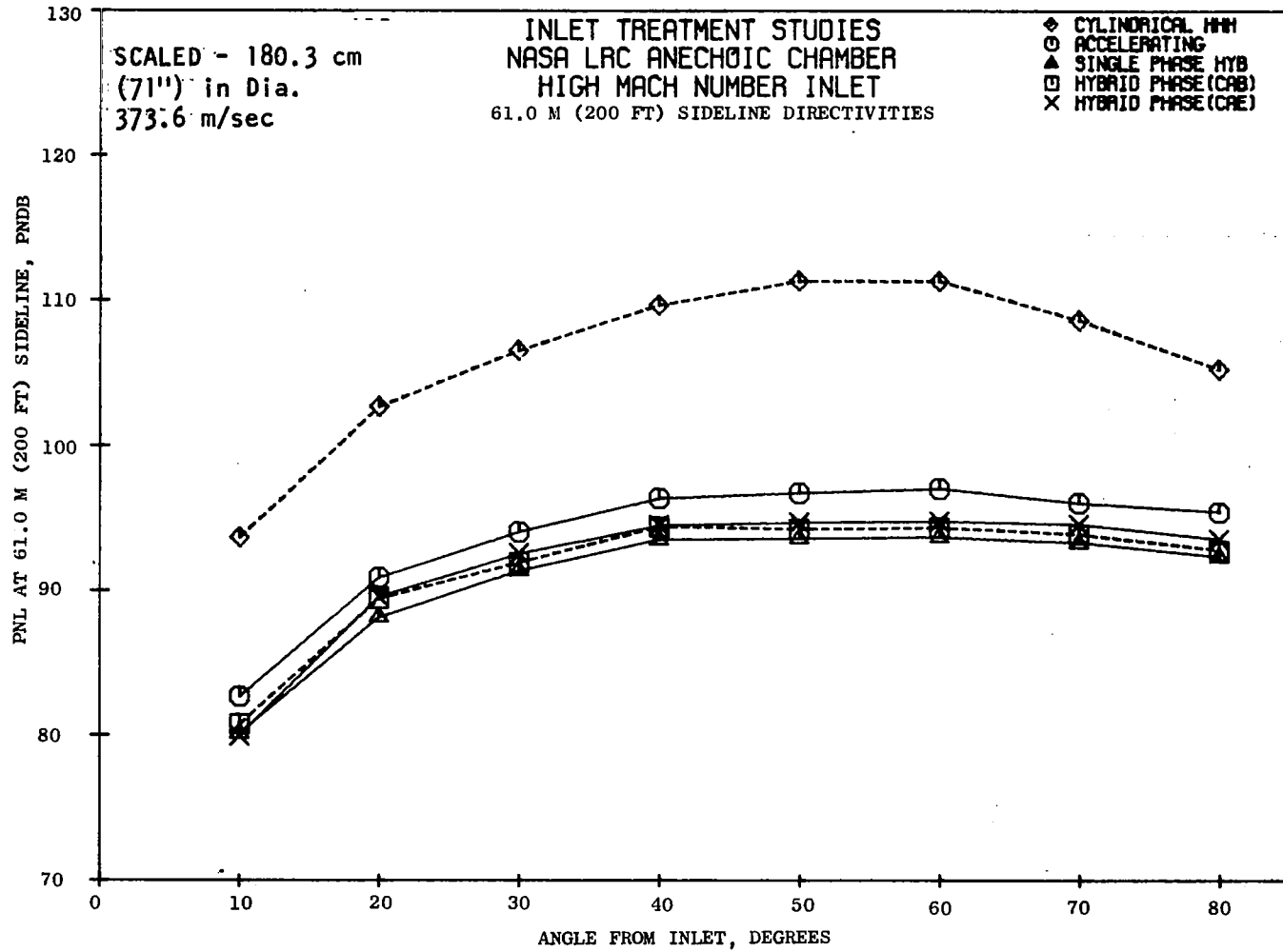


Figure 56. High Mach Number Inlet, PNL Directivities at 94% NF_C ($M_{TH} = 0.79$) for Five Inlet Configurations.

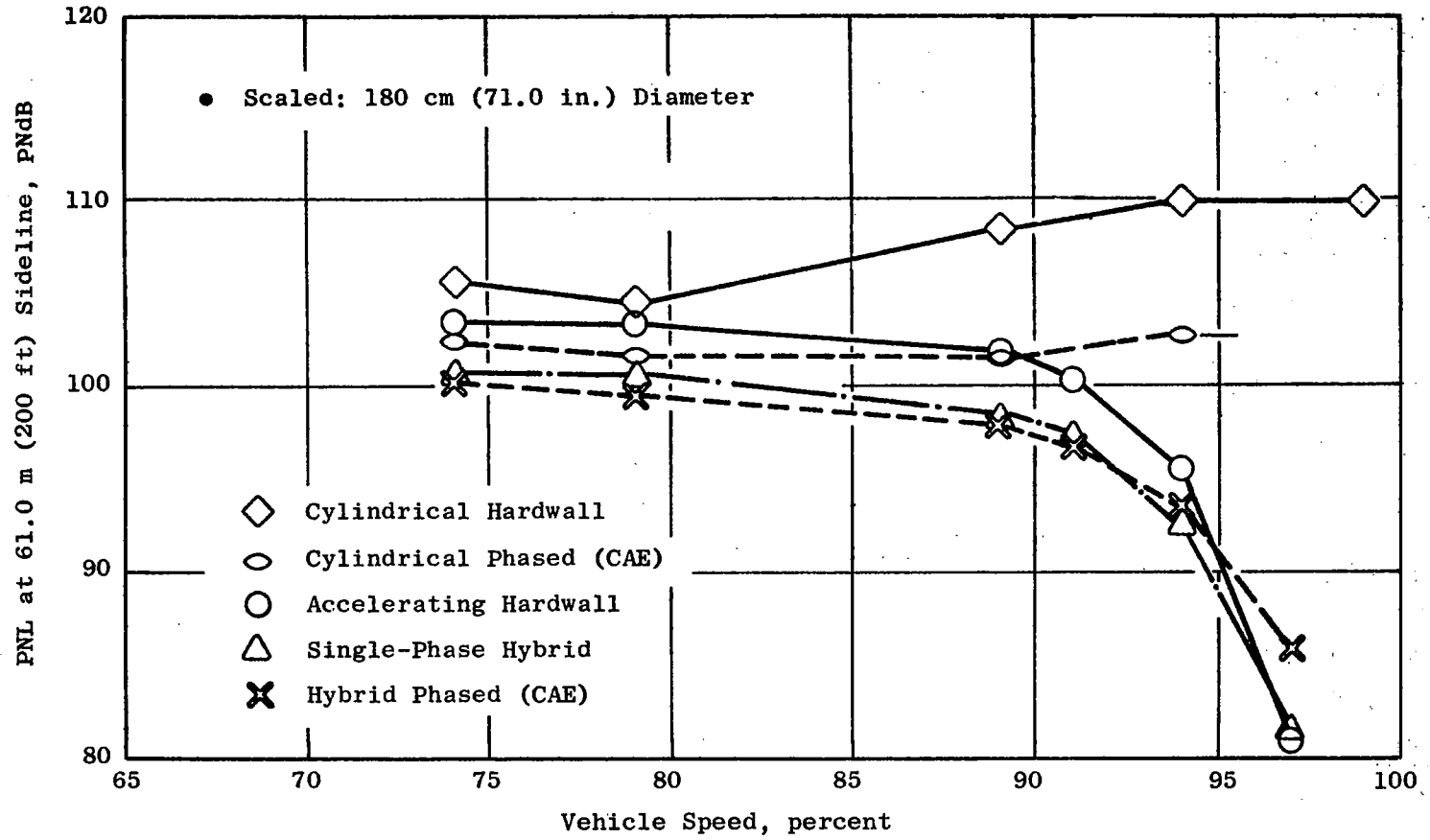


Figure 57. Maximum Perceived Noise Versus Vehicle Speed.

figures show the multiphase hybrid configurations CAB and CAE to be equivalent; thus, the data in Figure 57 show: (a) the effect of multiphase treatment configuration CAE, per se, without acceleration effects (i.e., in the cylindrical inlet); (b) the effect of the same treatment configuration in an accelerating inlet; and (c) the effect of high subsonic-flow Mach number, per se, without treatment effects (i.e., the cylindrical versus accelerating hardwall inlets). These data show the following:

- o The multiphase treatment CAE without acceleration effects increases in effectiveness with increasing vehicle speed, going from about 3 to more than 7 PNdB in the range from 74% to 94% rpm.
- o When this same treatment design is used in the high Mach inlet, there is essentially the same suppression over the lower end of the speed range, but it decreases with higher speeds until, at 97.5% of design speed, the treated inlet provides less suppression than the hardwall accelerating inlet. Except at this highest speed point, nevertheless, the treatment provided additional suppression, and at 94% speed the total due to both effects is about 17 PNdB.
- o The suppression of the accelerating inlet due to flow effects alone is significant above 79% of design speed (0.6 average throat Mach number) and is nearly 30 PNdB at 97.5% speed (0.83 average throat Mach number); this suggests that a choked inlet condition was rapidly being approached.

The perceived noise suppression achieved with this accelerating inlet is compared in Figure 58 to similar suppressions attained with other inlets. In all cases the data have been derived from model results measured in anechoic chambers which have been scaled to typical turbofan sizes. Two sets of data were from the NASA-LRC vehicle with different high Mach number inlets (2), while the remaining of data were from tests at General Electric's Corporate Research and Development Center anechoic chamber (unpublished). These results indicate that the current accelerating hardwall-inlet configuration produced comparable suppression levels relative to inlets which have been tested previously.

In-Duct Acoustic Probe Data

The acoustic results show that the suppression achieved independently with duct treatment and with accelerated flow are not linearly additive when combined in a hybrid inlet. This is consistent with prior experience at the General Electric Company (2,3); before this inlet treatment study, the difference had been ascribed to reduced treatment effectiveness due to higher flow rates over the treatment and/or increase in the source noise level resulting from the change in inlet geometry. This experimental program provided the opportunity to examine the suppression mechanism associated with hybrid inlets and to determine the relative amount of

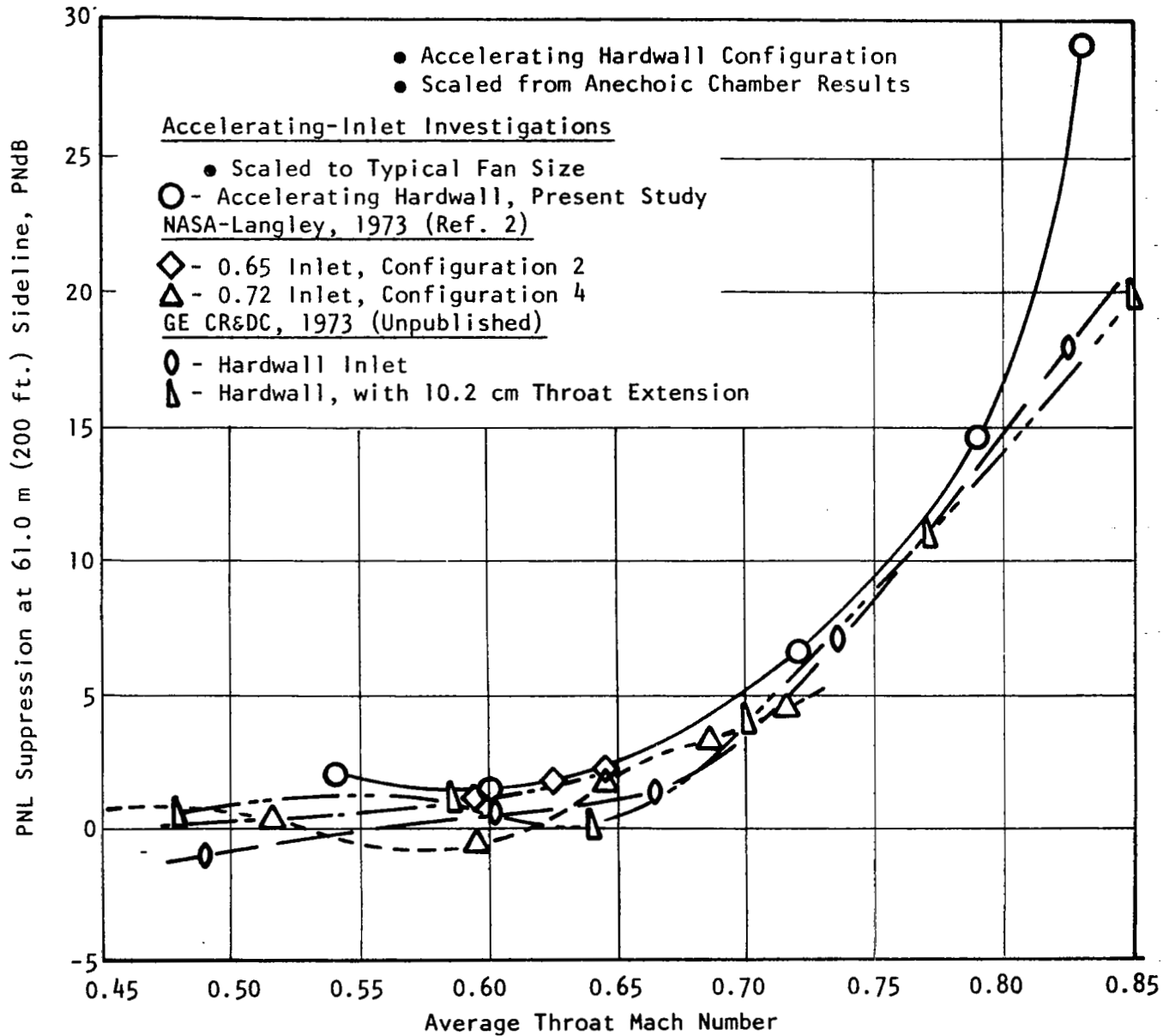


Figure 58. Comparison of PNL Suppression with Other Representative High Mach Number Inlet Results.

reduction attained through the treatment and throat region of the high Mach number inlet.

Acoustic probe measurements were taken at three positions in the inlet. The first was just forward of the inlet plane; the second was just downstream of the inlet throat; and the third was downstream of the treatment section, as shown in Figure 59. Probe narrowband results are presented in this figure for the single-phase hybrid configuration at a throat Mach number of 0.72. These spectra were measured near the outer wall, approximately along a streamline. The results indicate that the multiple pure tones and blade passing fundamental were substantially reduced as the sound waves propagated through the treatment section. At the measuring station upstream of the throat, all of the multiple pure tones and the BPF tone have been eliminated, and the high frequency broadband levels significantly reduced.

At each of these axial positions, data were recorded with the probes at a number of immersions (5 to 7) and sound power levels of the blade passing tone were estimated by integration of the sound pressure levels across the duct. Differences between probe pairs are summarized in the table in Figure 60 for the accelerating hardwall and single-phase hybrid configurations at three throat Mach numbers. The quantities listed for each configuration are the differences in estimated tone power level between the two stations indicated. That is, that listed under "Source to Bellmouth" is the total change in BPF power level as a consequence of the combined attenuation from high subsonic flow Mach number and from the acoustic treatment if present; that listed under "Source to Throat" is the change attributable primarily to the treatment when it is installed; and, that listed under "Throat to Bellmouth" is the change in power level attributable primarily to the flow Mach number effect. Actually, these measurements do not separate each effect rigorously, and some flow-effect attenuation is involved in the probe data from the throat location. Nevertheless, such data from these principal locations is indicative of the relative roles of flow-effect and of treatment in the overall attenuation. Bearing these qualifications in mind, the following points are of interest:

- o The "Source to Bellmouth" data show the hybrid inlet to provide more reduction than the hardwall accelerating inlet at all three speeds, so the treatment is clearly effective to some degree. However, from these data alone, the relative roles of the two attenuation mechanisms are undefined.
- o The "Source to Throat" data show that the attenuation of the hybrid inlet in this section increases with increasing speed, while that of the hardwall accelerating inlet varies from an apparent amplification of 3.7 dB (74% speed) to an attenuation of 7.1 dB (94% speed) even though there was no treatment in this region. This behavior for the hardwall case is believed to be a combination of two probable effects: (a) a longitudinal standing wave as a result of the interaction of two or more different

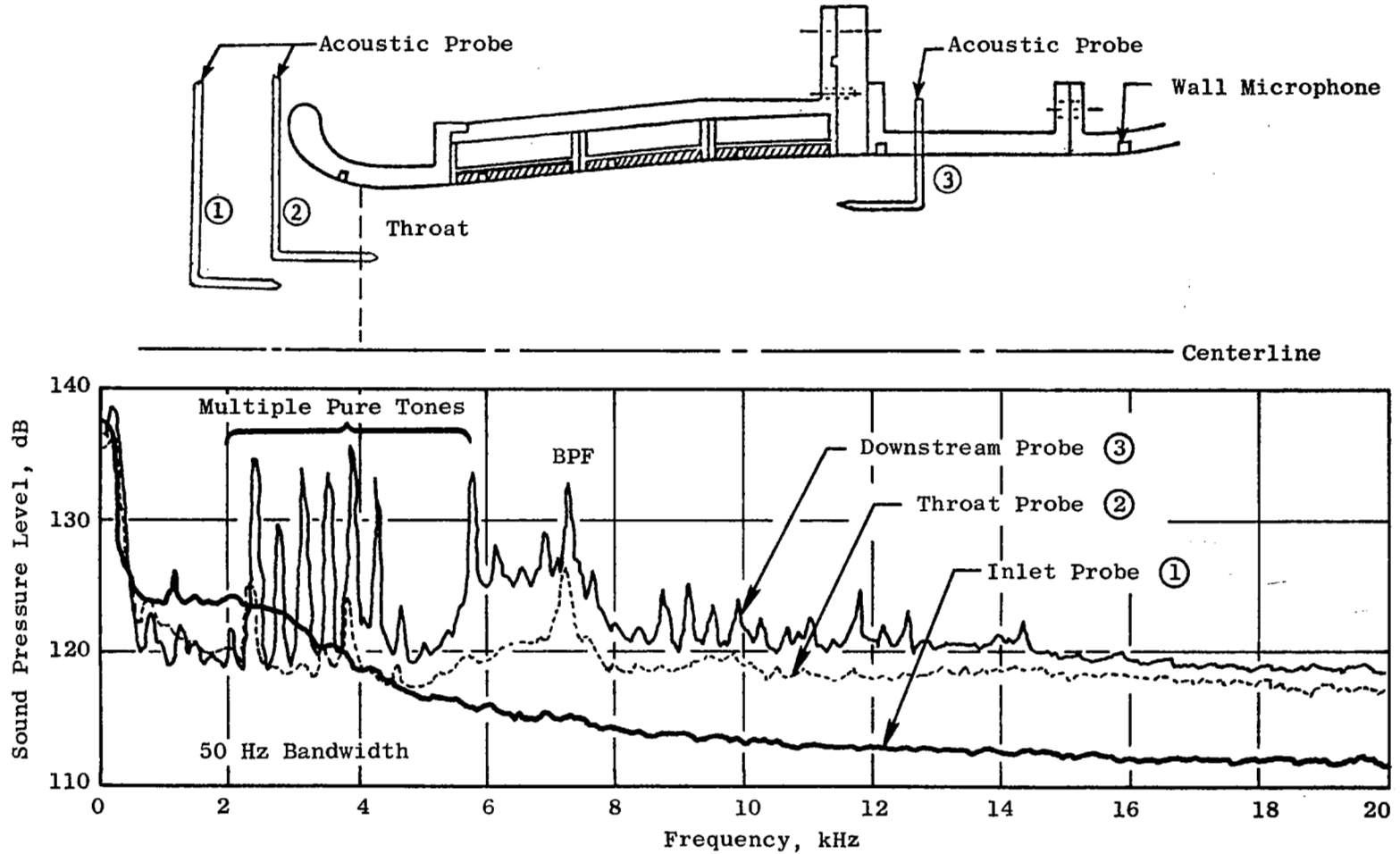
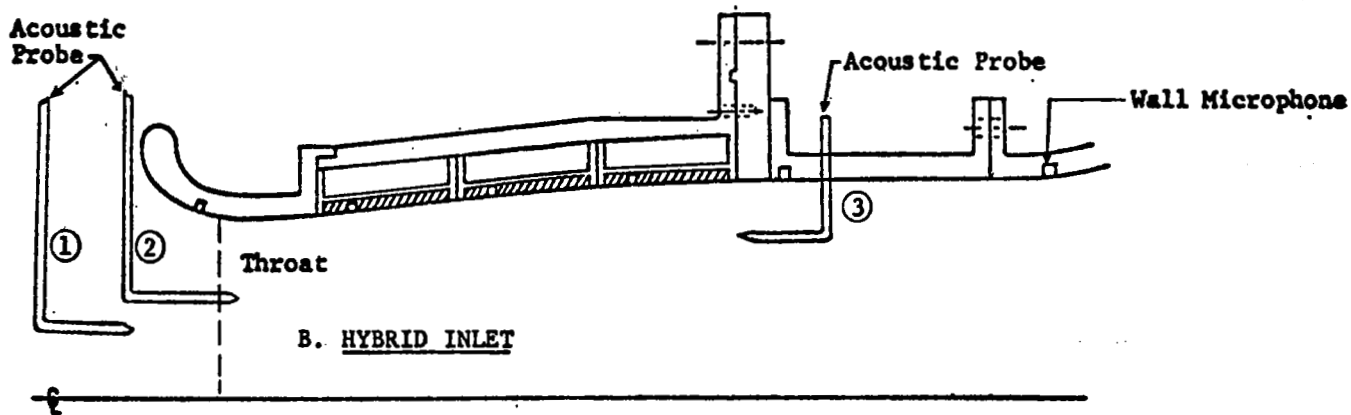


Figure 59. In-Duct Acoustic Probe Results at 89% N_{FC} ($M_{TH} = 0.72$) for Configuration 22 (Single Phase Treatment) as Measured Near the Wall).



Percent Speed	Throat Mach Number	Configuration	Change in BPF Power Level, dB		
			Source to Bellmouth ($L_{W3} - L_{W1}$)	Source to Throat ($L_{W3} - L_{W2}$)	Throat to Bellmouth ($L_{W2} - L_{W1}$)
74%	0.54	Hybrid, Single Phase	7.8	8.4	-0.6
		Accelerating Hardwall	2.6	-3.7	6.3
		Treatment Effect	5.2	12.1	-6.9
89%	0.72	Hybrid, Single Phase	23.3	12.0	11.3
		Accelerating Hardwall	14.7	0	14.7
		Treatment Effect	8.6	12.0	-3.4
94%	0.79	Hybrid, Single Phase	27.0	19.1	7.9
		Accelerating Hardwall	23.8	7.1	16.7
		Treatment Effect	3.2	12.0	-8.8

Figure 60. BPF Tone Suppression Based on Probe Results for High Mach Number Inlet.

spinning modes (likely to be more important at the lowest speed setting), and (b) some flow-effect attenuation having already taken place by the time the throat probe is reached (likely to be more important at the highest speed setting). If these effects took place in both type inlets by a relatively equal amount at each speed setting, then the fact that the attenuation of the hybrid inlet relative to the accelerating inlet remains constant in this section (12 dB), independent of the speed, is indicative that the attenuation due to the treatment, per se, has remained constant and has not been degraded by the increasing Mach number.

- o The "Throat to Bellmouth" data indicates that an appreciable portion of the attenuation takes place in this section on the accelerating inlet; however, when there is treatment (the hybrid), the amount of attenuation in this section due to flow effects is reduced a significant amount.

The fact that probe results indicated a reduction of the blade passing tone power level of 12 dB through the treatment section at each speed could be a coincidence, for the frequency of the tone increased with fan speed; however, other evidence also indicates that the tone reduction was constant over this speed range. One such set of data consists of duct measurements by means of flush-mounted microphones: the levels of the BPF tone on the wall of the single phase hybrid configuration are presented in Figure 61 for the three speeds; these data indicate that about 10 dB reduction occurred for each speed point between measurement positions 2 and 3. Also, probe data from the single phase cylindrical inlet, providing directly corresponding information as in Figure 60, showed 13 dB suppression by the treatment at the 89% speed point; this is within 1 dB of that deduced for the treatment in the high Mach inlet. Finally, the indication that the suppression of the BPF tone was the same, even though the frequency was changing with speed, is supported by the data for the single phase cylindrical inlet presented in Figure 30 for each of these speeds.

Thus, rather than coincidence, the accumulated data indicate blade passing tone suppression through the treatment section remained approximately unchanged as flow was accelerated, contrary to previous belief. Further, less reduction of the tone power level was achieved by acceleration of the flow through the throat when the tone had already been reduced by acoustic treatment downstream of the throat. Nevertheless, generally more total suppression was achieved with a hybrid inlet, due to the coupled effects of treatment suppression and acceleration suppression.

It might be postulated that, as the sound wave propagates through a treated section of duct, sound energy in the higher order modes is reduced, i.e., the sound energy most readily absorbed. The characteristics of the sound waves as they enter the accelerated flow region are now quite different from the characteristics of the sound waves entering the same region of the hardwall, high Mach number inlet. Although inlet flow characteristics are unchanged for the throat region, the acceleration suppression mechanism

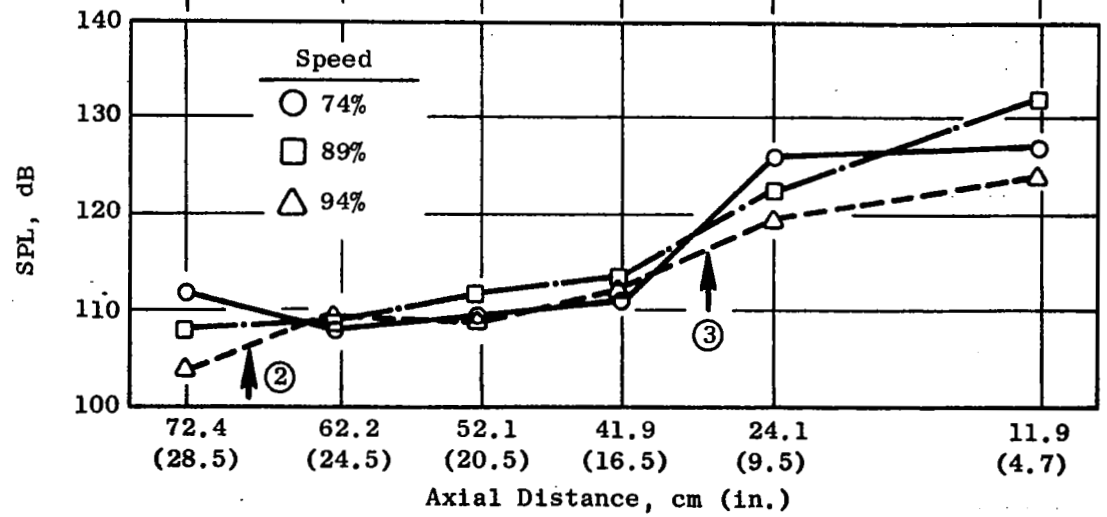
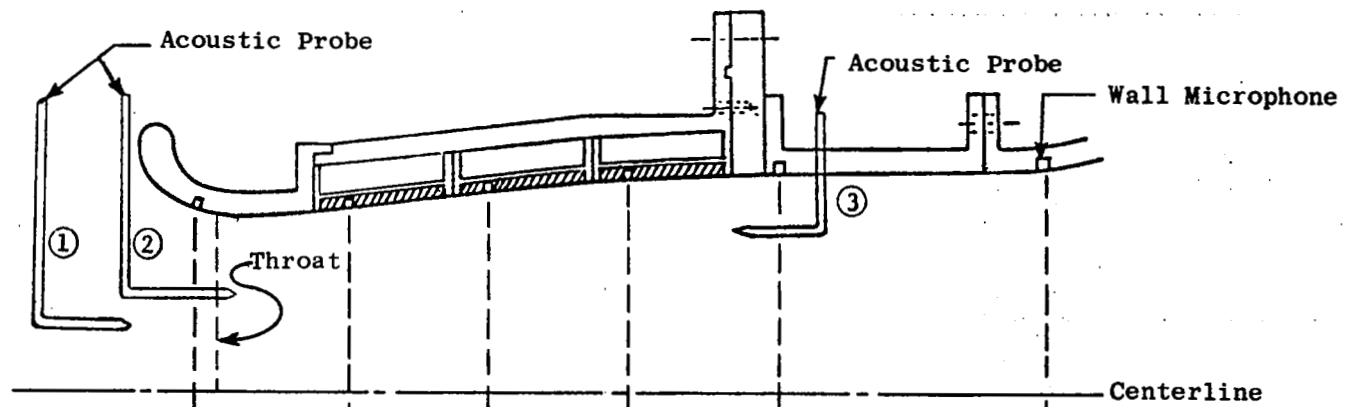


Figure 61. BPF Sound Pressure Levels on the Wall of the Single Phase Hybrid for Three Speed Settings.

is working on sound waves with quite different characteristics, and less additional reduction of the propagating sound energy is attained for the sound waves with the lower order mode energy content.

6.3.2 Aerodynamic Performance of High Mach Inlet

The axial distribution of the wall Mach number is presented in Figure 62 for the accelerating hardwall configuration. Similar measurements with essentially identical results were made for the single phase hybrid configuration. The inlet generally operated as designed. The flow along the wall was accelerated sharply from the leading edge of the inlet lip to a point just upstream of the geometric throat. The flow was then rapidly diffused between this point and the treatment section; the diffusion continued through the treatment section at a slower rate, reaching a relatively constant wall Mach number in the downstream portion of this section.

The data indicated that the flow became supercritical in the vicinity of the throat at the highest speed. This suggests that local shocks may have existed at this fan speed. Further, the wall Mach number distributions indicated that the inlet operated without separation.

A key nondimensional parameter used to evaluate inlet aerodynamic performances is the recovery factor. Recovery is defined as the average total pressure from the rake divided by the barometric pressure. Calculated recovery factors are shown for both the accelerating hardwall and single-phase hybrid configurations in Figure 63 as a function of average throat Mach number. Both configurations exhibited good recovery characteristics up to a throat Mach number of 0.8.

In summary, the inlet flow was accelerated to an average throat Mach number of 0.8 without separation, and with high recovery. These performance characteristics show that the noise suppression attained by accelerating the flow to average throat Mach numbers of 0.72 to 0.79 was achieved without significantly compromising aerodynamic performance.

6.4 INLET TURBULENCE AND ASSOCIATED NOISE FOR THIS EXPERIMENTAL TEST CONFIGURATION

The experimental results for inlet turbulence measurements and associated noise levels for this test set-up with and without an inlet screen are presented and discussed in this section for the cylindrical, accelerating, and single-phase hybrid inlets.

Published information on the nature of the noise generated by the turbulence-rotor interaction mechanism^(2,3,18) suggests:

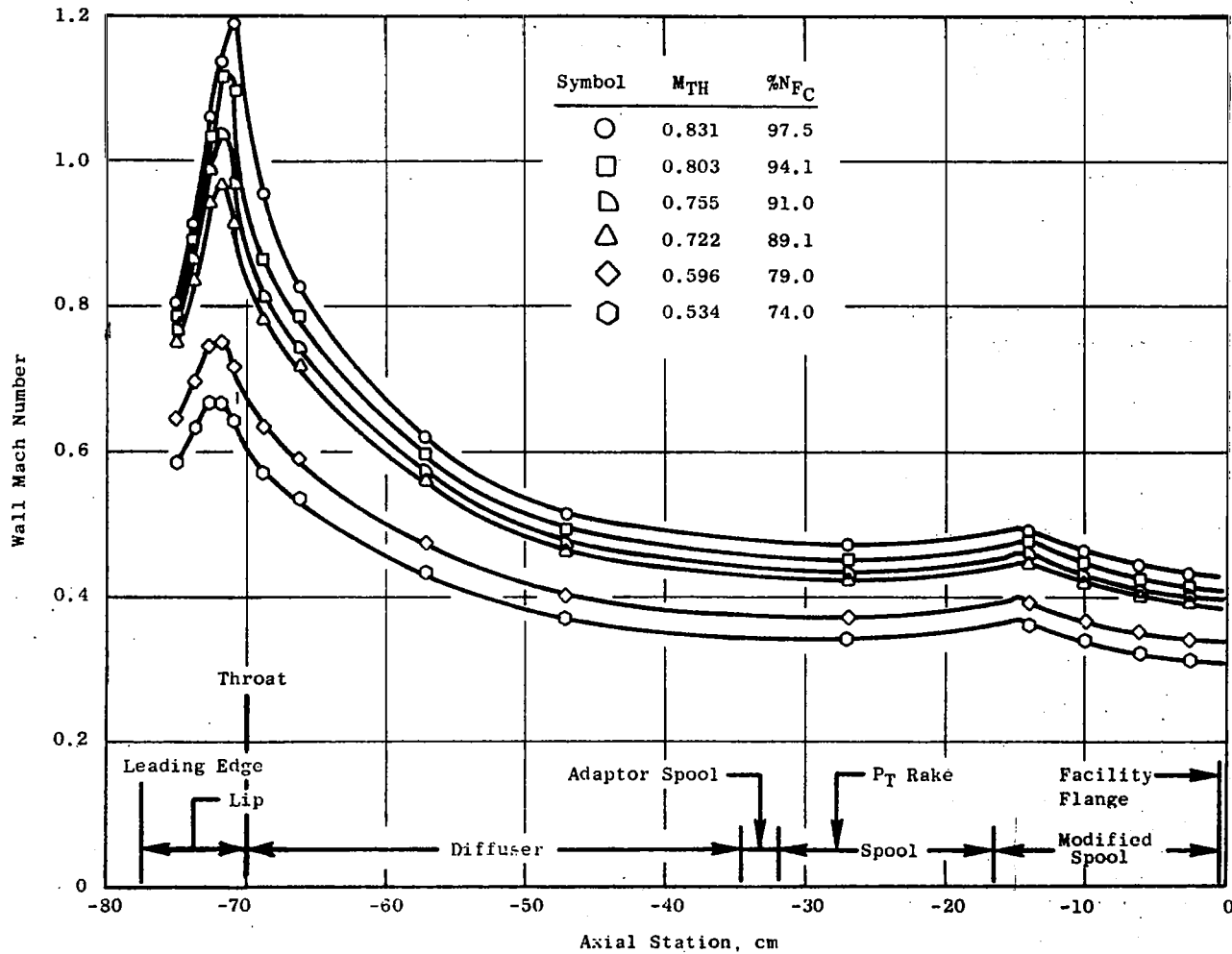


Figure 62. Wall Mach Number Distributions for the Accelerating-Hardwall Inlet.

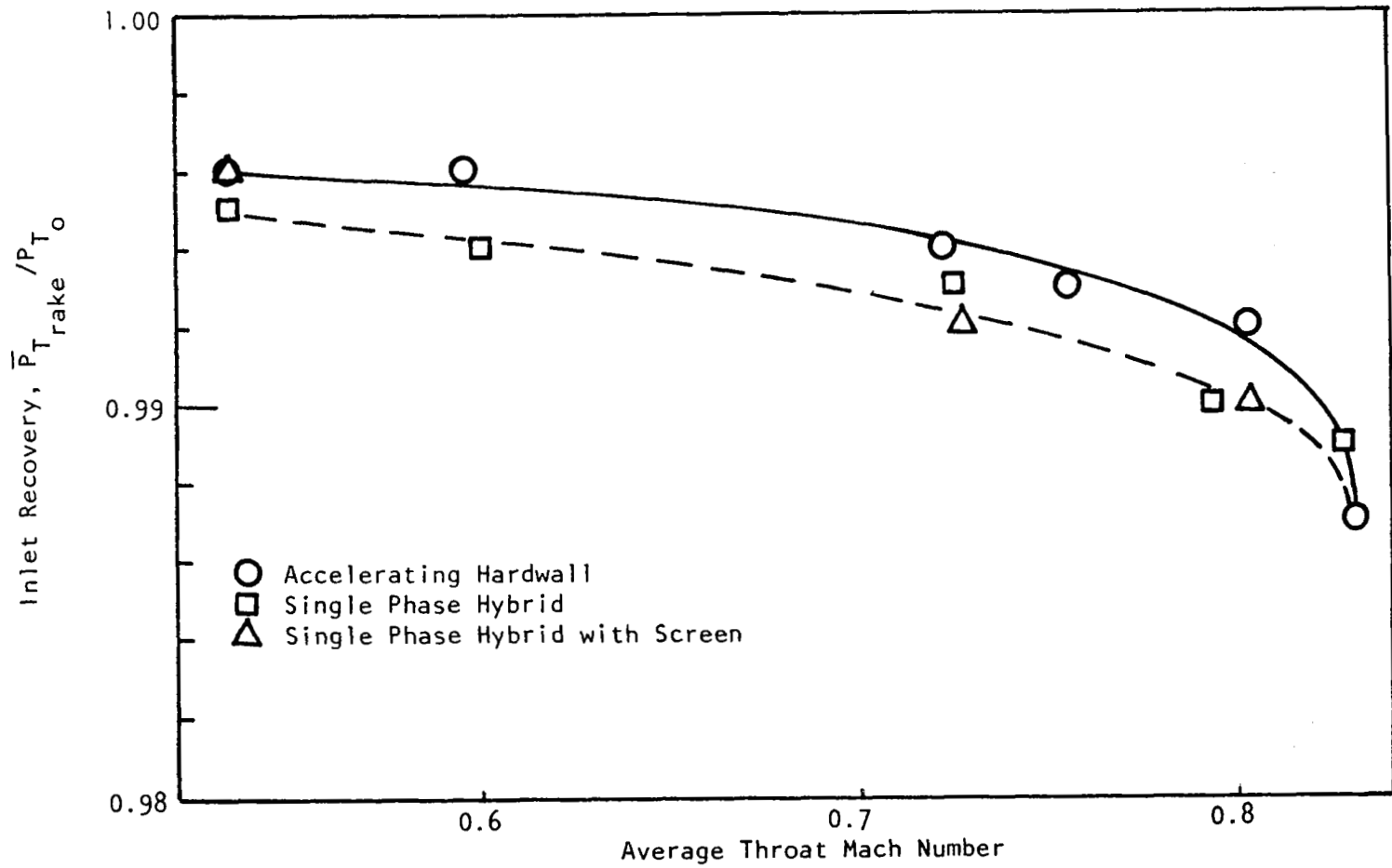


Figure 63. High Mach Number Inlet Recovery.

- o The axial length of turbulent cells plays a large part in determining the extent to which the noise is concentrated at blade passing frequency and its harmonics, long eddys appear to the rotor as a quasi steady-state distortion giving rise to strong tonal content; shorter eddys produce more broadband noise.
- o The intensity level of the turbulence determines the amount of the noise increase.

Therefore, the three most basic quantities of interest experimentally are the integral-length scale in the axial direction and the two components of unsteady velocity, axial and circumferential. These data were obtained at 74%, 89%, and 94% of rotor design speed, at which the rotor tip speeds were subsonic (0.86 Mach No.), transonic (1.04 Mach No.), and supersonic (1.10 Mach No.); thus, the two higher speeds involved rotor-alone noise associated with Mach waves on the blades as well as the ordinary turbulence-rotor interaction noise.

6.4.1 Turbulence Data

The data for the axial integral-length scale of the inlet turbulence for the three inlets are presented in Figure 64 for the case without the inlet screen and in Figure 65 with the screen. These data are for the 74% and 89% speed points; the 94% speed point data, not shown, was essentially the same as for the 89% case. The data show that without the screen, the length scale of the turbulence was greater for the High Mach inlet (both accelerating and hybrid) than for the cylindrical inlet, but when the screen was added, both type inlets were essentially the same. This was the result of a reduction of the length scale for the High Mach inlet; essentially no change occurred for the cylindrical inlet. The treatment in the High Mach inlet, as might be expected, had no appreciable effect.

In all cases the length scale is large, being in the range of 5 to 60 meters or 15 to 180 fan diameters. This axial scale of turbulence is such that, according to Pickett's⁽³⁾ analysis, the predicted effect on the rotor noise generation should be primarily on BPF and harmonic tone levels. In fact, the analysis indicates that for this vehicle an axial eddy length of only three meters would cause noise at BPF and harmonics, and any increase in axial scale would produce no increase in tone discreteness.

The associated mean-velocity profiles, as determined by the DC component of the hot-wire probe, are given in Figures 66, 67, and 68 for each inlet with and without the inlet screen including the cylindrical, accelerating, and hybrid inlets, respectively. The inlet screen had no significant effect upon the shape of the velocity profiles, but it did reduce the mean velocity a small amount.

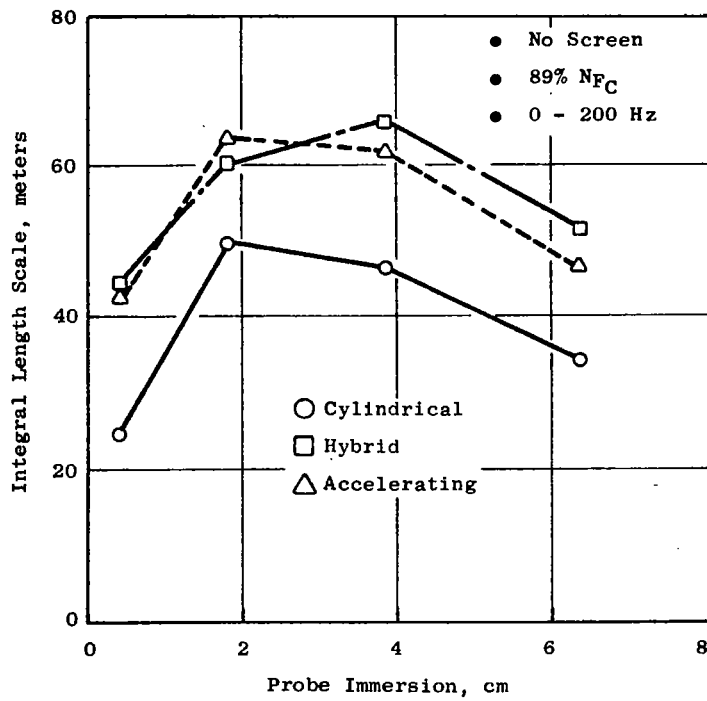
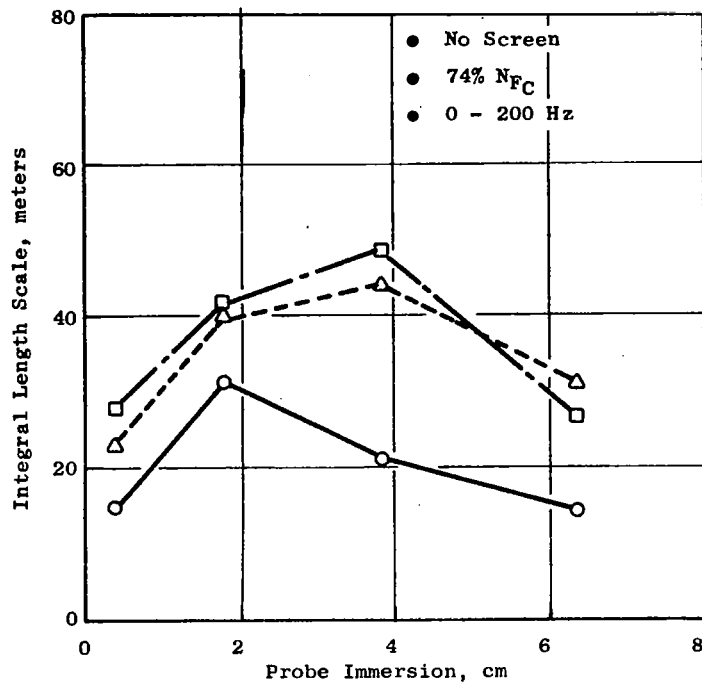


Figure 64. Axial Turbulence Integral-Length Scale, Three Inlets, 74% and 89% N_{FC} , without Screen.

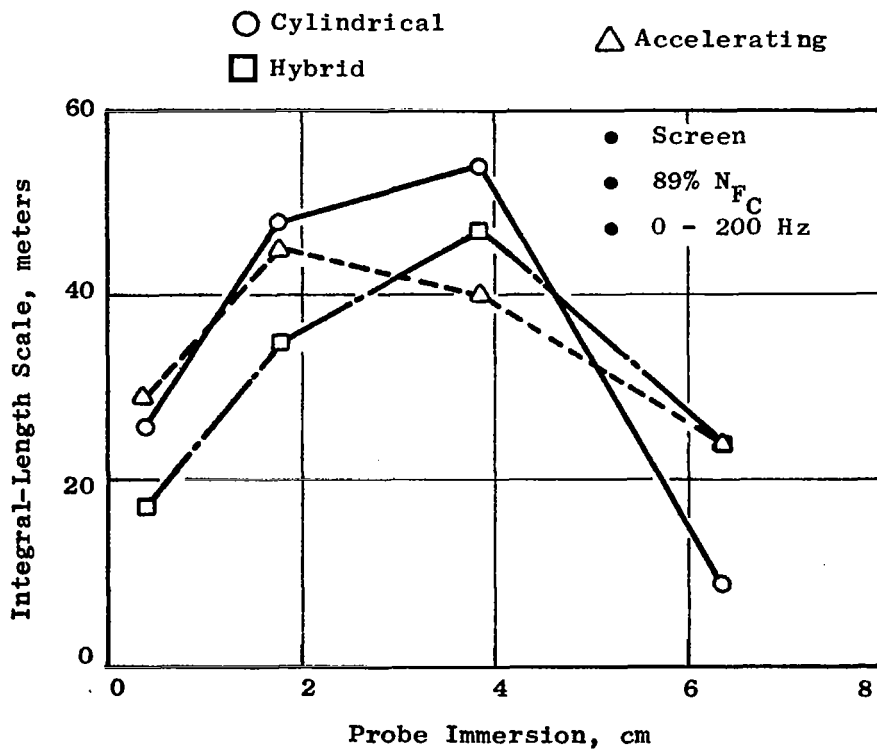
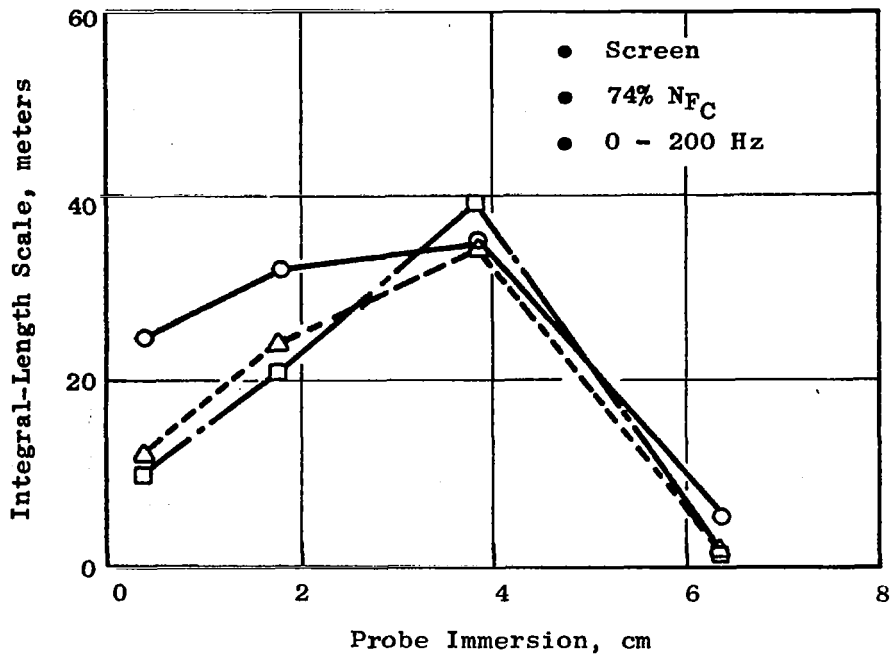


Figure 65. Axial Turbulence Integral-Length Scale, Three Inlets, 74% and 89% N_{FC} , with Screen.

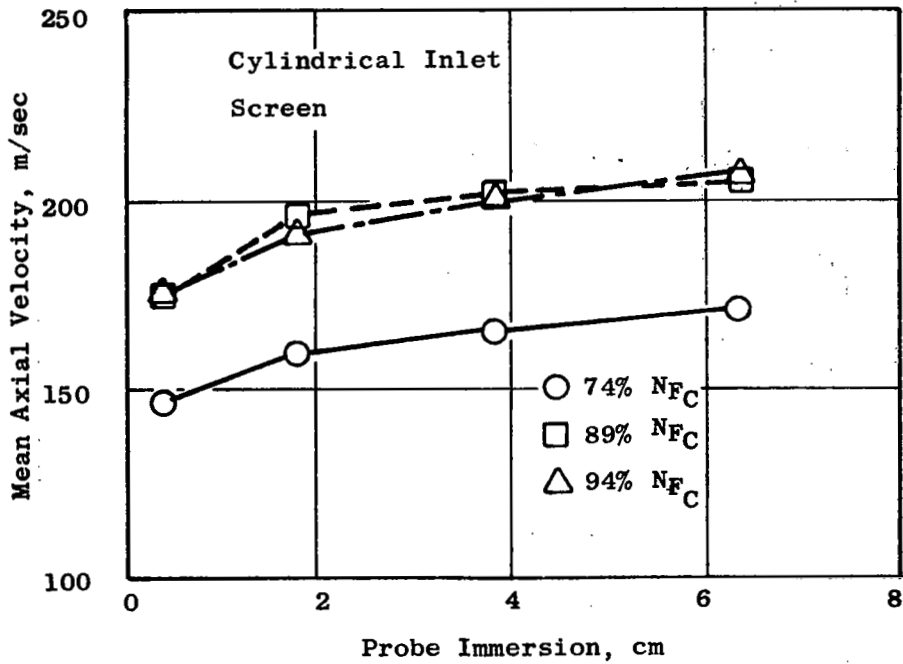
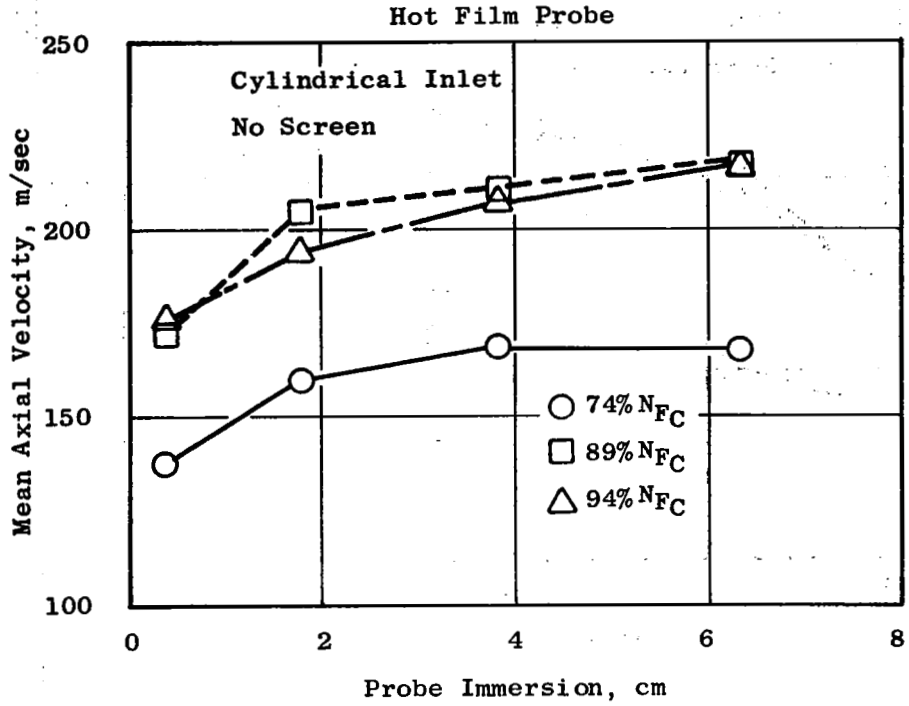


Figure 66. Mean-Velocity Profiles, Cylindrical Inlet.

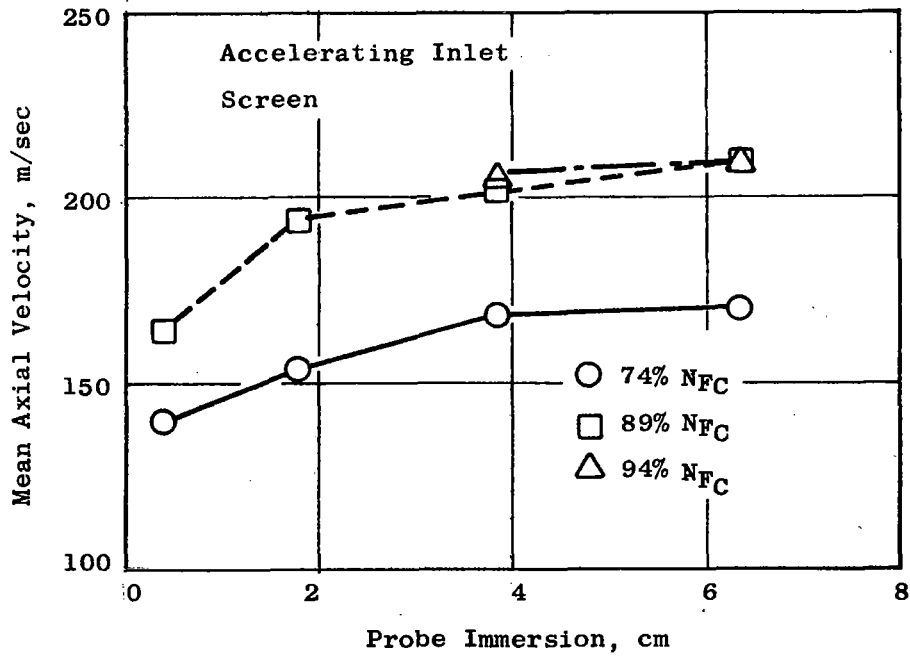
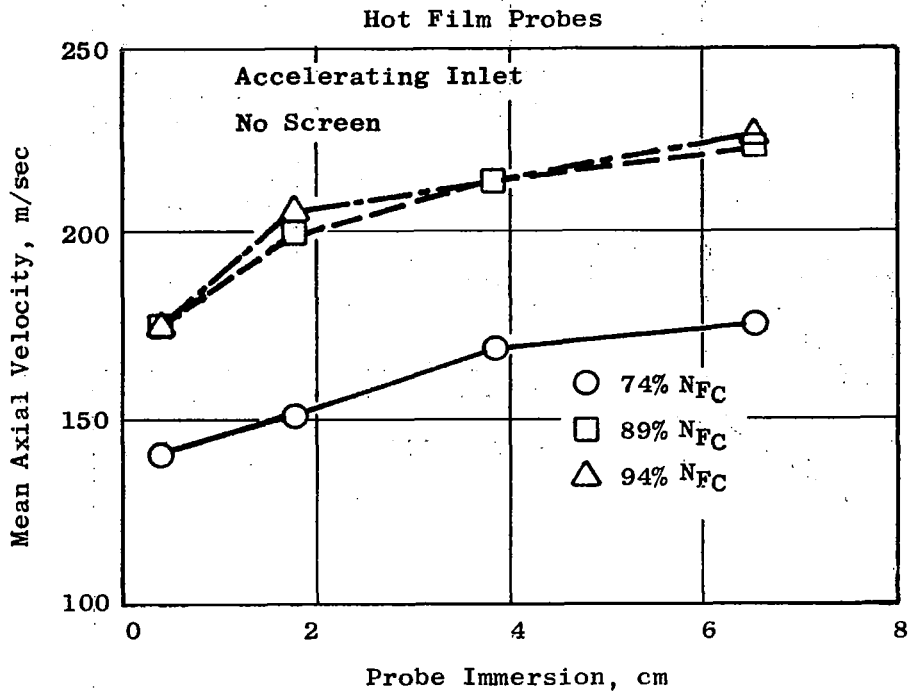


Figure 67. Mean-Velocity Profiles, Accelerating Inlet.

Hot-Film Probe

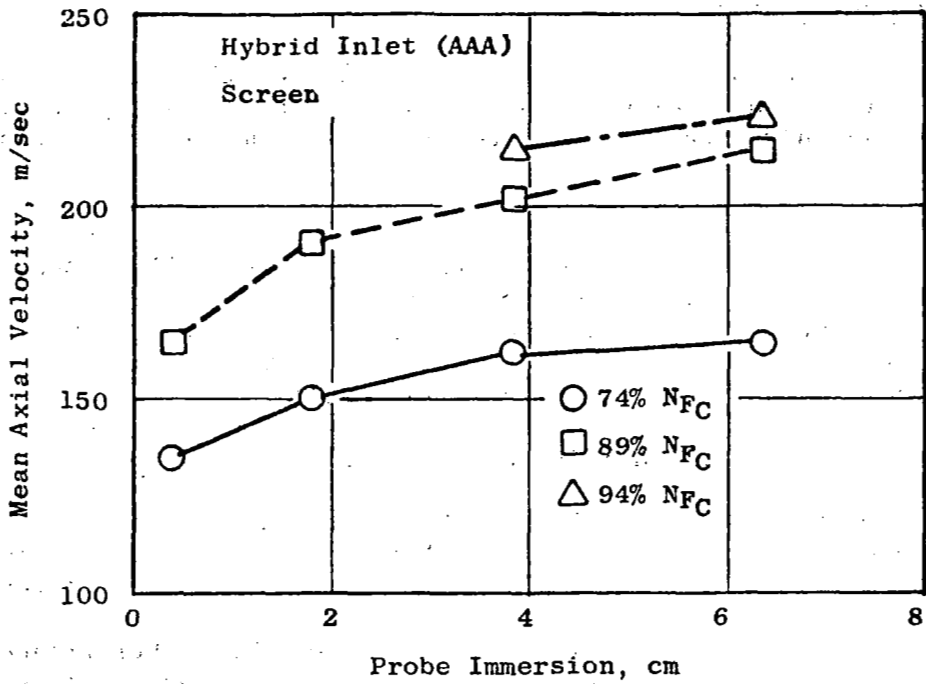
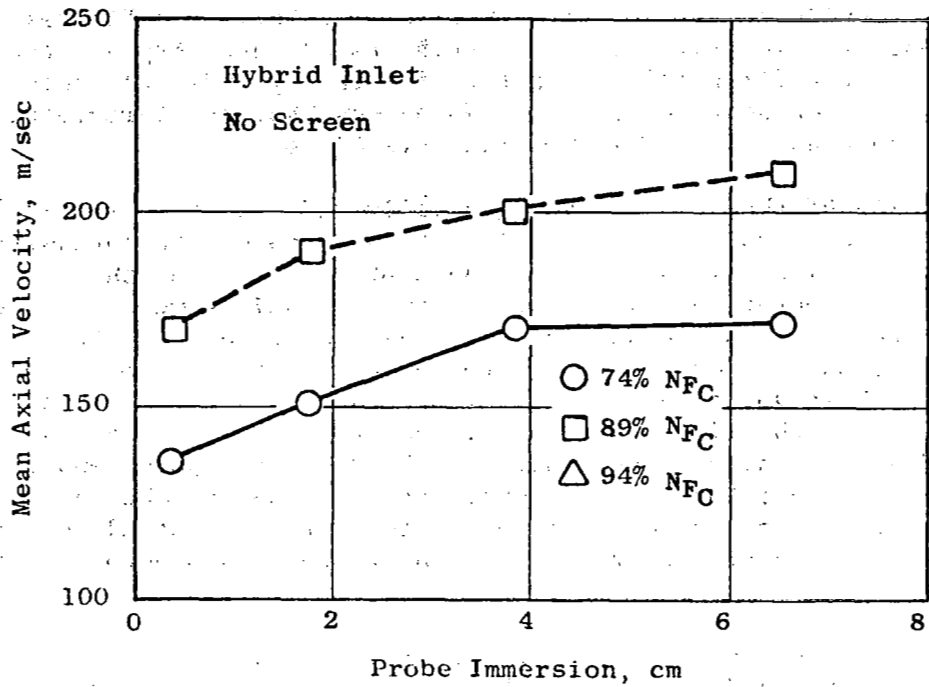


Figure 68. Mean-Velocity Profiles, Hybrid Inlet.

The axial and circumferential turbulence intensity levels for each of the three inlets with and without inlet screens are given in Figures 69, 70, 71, 72, 73, and 74. The first three give the axial intensity and the second three give the circumferential intensities for the cylindrical, accelerating, and hybrid inlets, respectively. These data show that the turbulence intensity levels are about the same for all three inlets.

The addition of the inlet screen generally reduced the intensity levels by a factor between about 1.5 to 2. Without the screen, the intensity level in the axial direction varied from the range of 3 to 4% near the wall to about 1% near the centerbody; with the screen, the values were reduced to about 2% near the wall and about 0.5% near the centerbody. In the circumferential direction, the levels tended to be more uniform across the duct although the highest value was, with only one exception, nearest the wall. Without the screen, the circumferential intensity level near the wall was between 2 and 4%, having a higher value at the 74% speed point and a lower value at the 89% point; the screen reduced these values to the range of 1 to 2%. Through the rest of the duct traverse, the circumferential intensity level was in the range of 1 to 2% without the screen and 0.5 to 1% with the screen.

Thus, the screen was effective in significantly reducing turbulence intensity levels, but did not appreciably affect the axial integral-length scale, at least insofar as its expected effect on rotor noise is concerned.

6.4.2 Acoustic Data

The 1/3 octave band PWL spectra for the cylindrical, accelerating, and hybrid inlets are shown in Figures 75, 76, and 77, respectively; in each case, data are shown without and with the inlet screen, for 74, 89, and 94% speed points.

At the lowest (subsonic tip) speed point, the spectra are dominated by the BPF tone or, in the case of the hybrid inlet, by the BPF second harmonic. At the middle (transonic tip) speed point, MPT's appear at levels nearly equal to that of the BPF 1/3 octave band in the case of the cylindrical and accelerating inlet; the hybrid inlet spectra, both with and without the inlet screen, have little MPT content but the high frequency noise from BPF through the next five 1/3 octave bands, dominates. At the highest (supersonic tip) speed point, the spectra for all inlets are dominated by MPT's.

The primary effect of the inlet screen at the lowest speed point, as expected because of the long axial integral-length scale of the turbulence, is to reduce the BPF tone level; smaller but detectable reduction occurred at frequencies above the second harmonic. The reduction of the 1/3 octave band containing the tone was between 2 and 3 dB; that of the higher frequency bands was 1 dB or less. The cylindrical inlet was affected by the screen less than the accelerating or hybrid inlets.

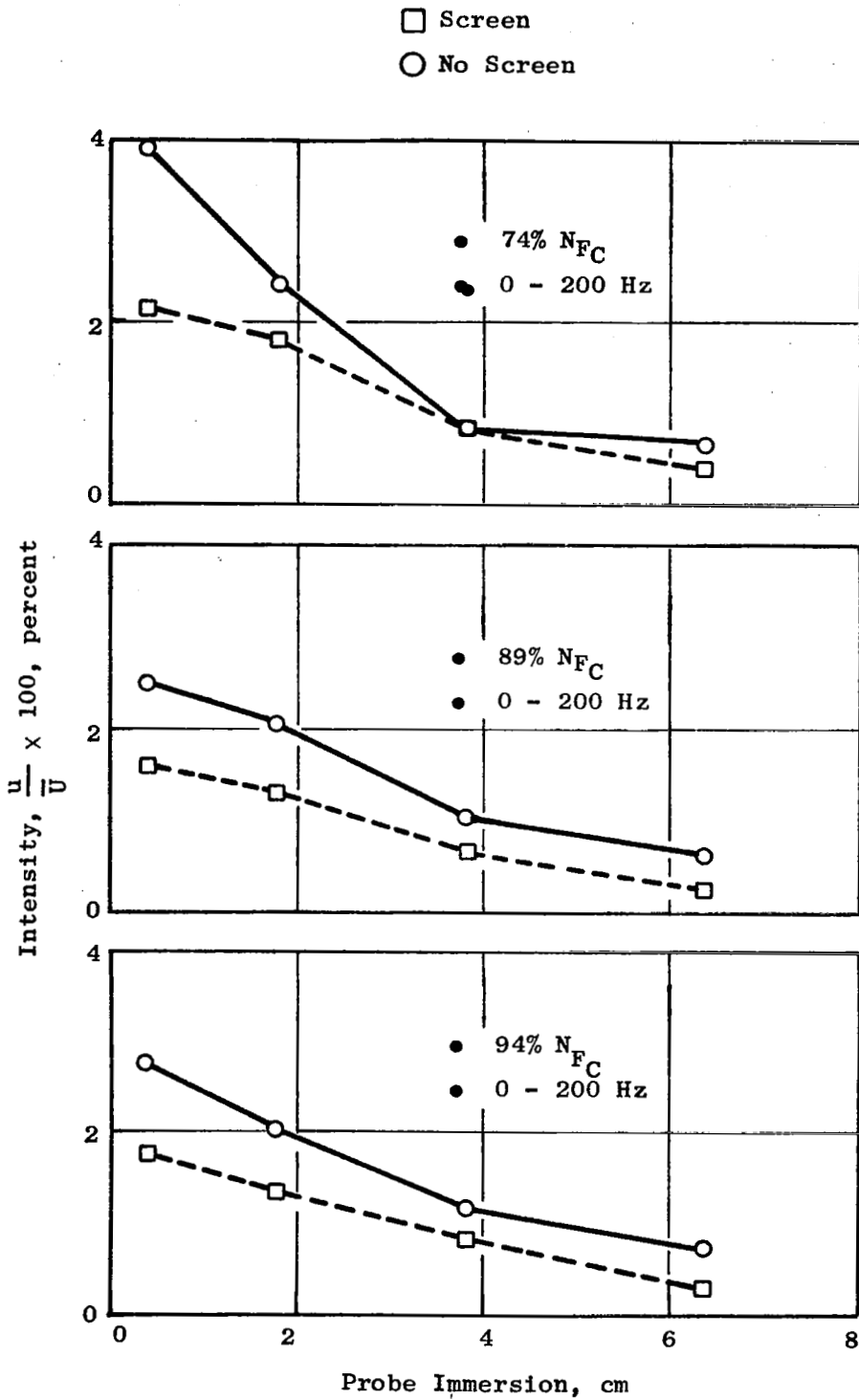


Figure 69. Axial Turbulence Intensity, with and without Inlet Screen, Cylindrical Inlet.

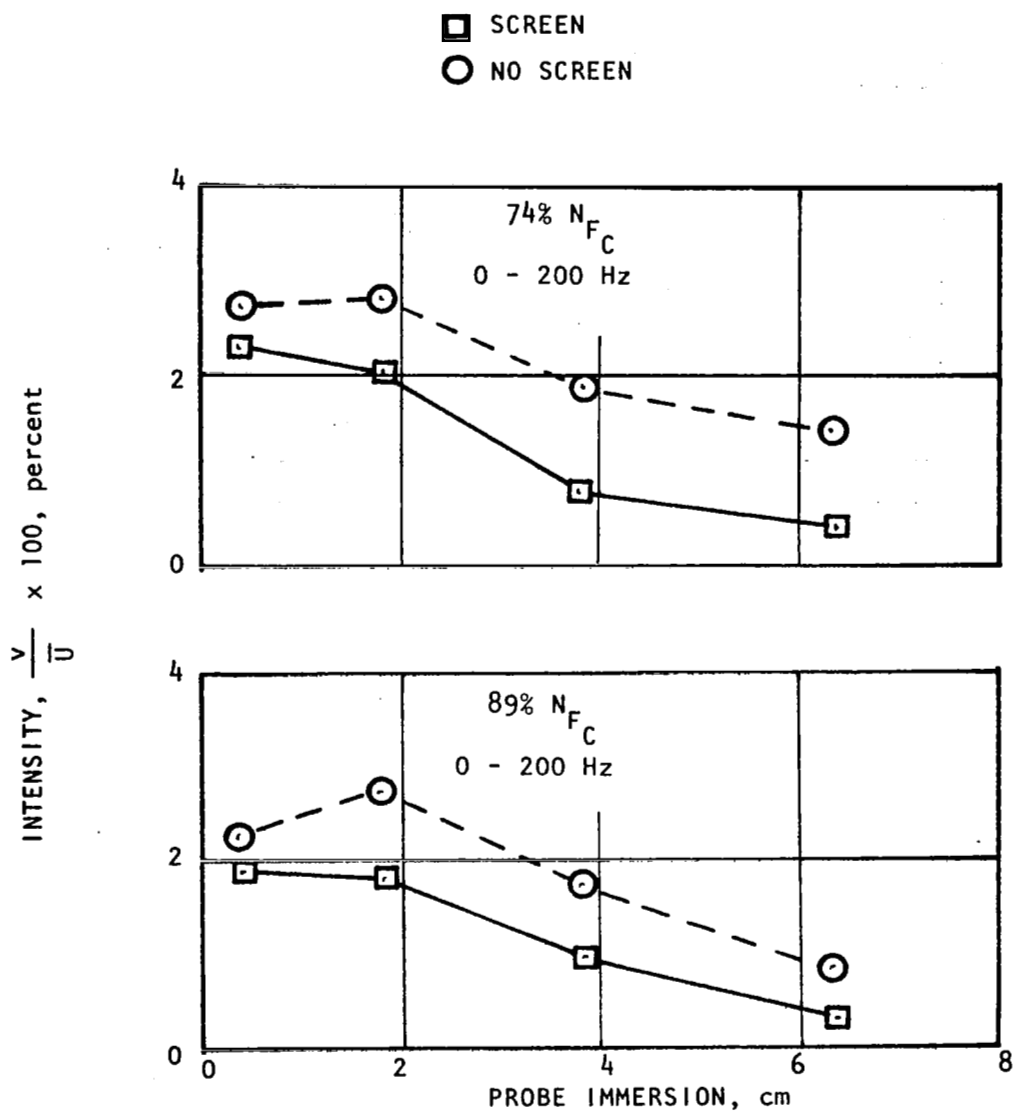


Figure 70. Axial Turbulence Intensity with and without Inlet Screen, Accelerating Inlet.

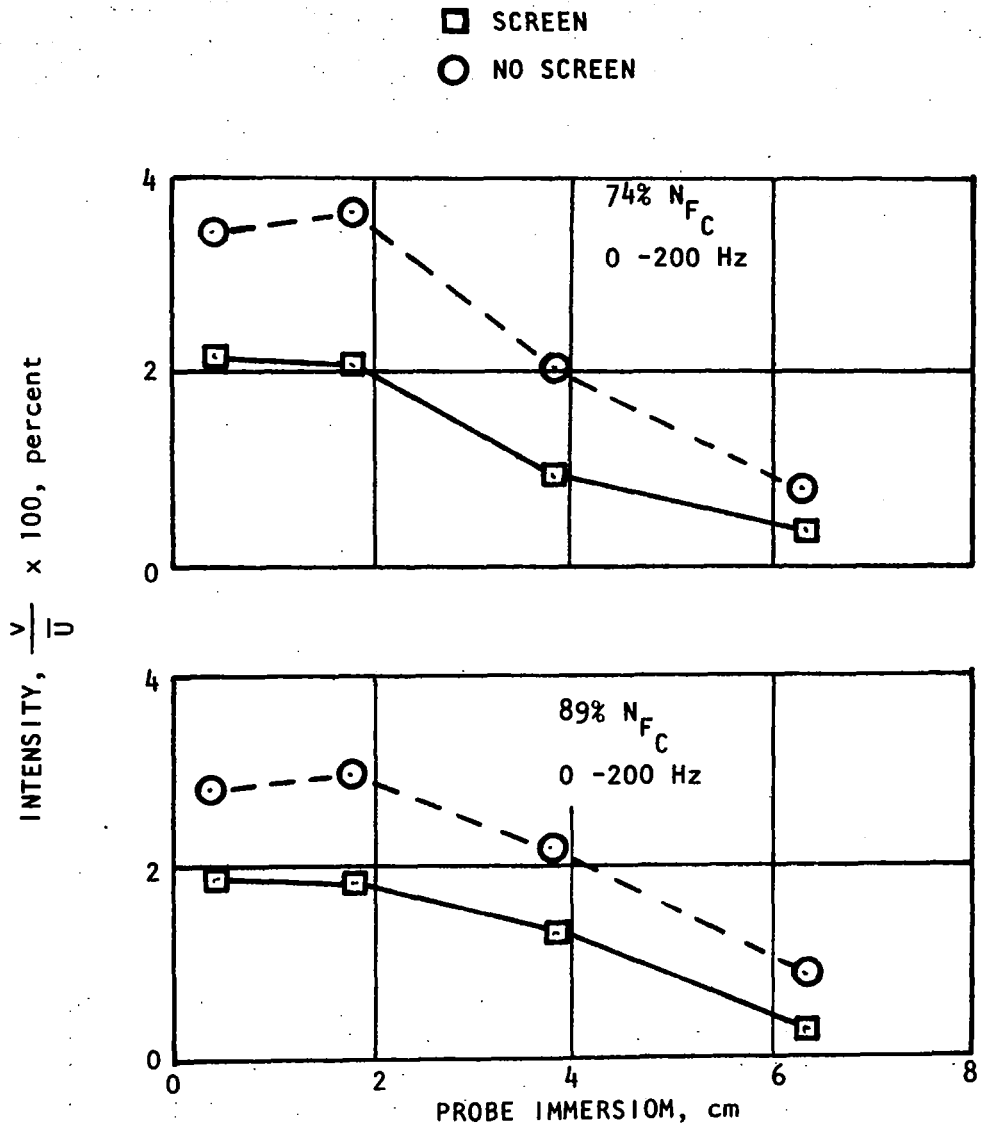


Figure 71. Axial Turbulence Intensity with and without Inlet Screen, Hybrid Inlet.

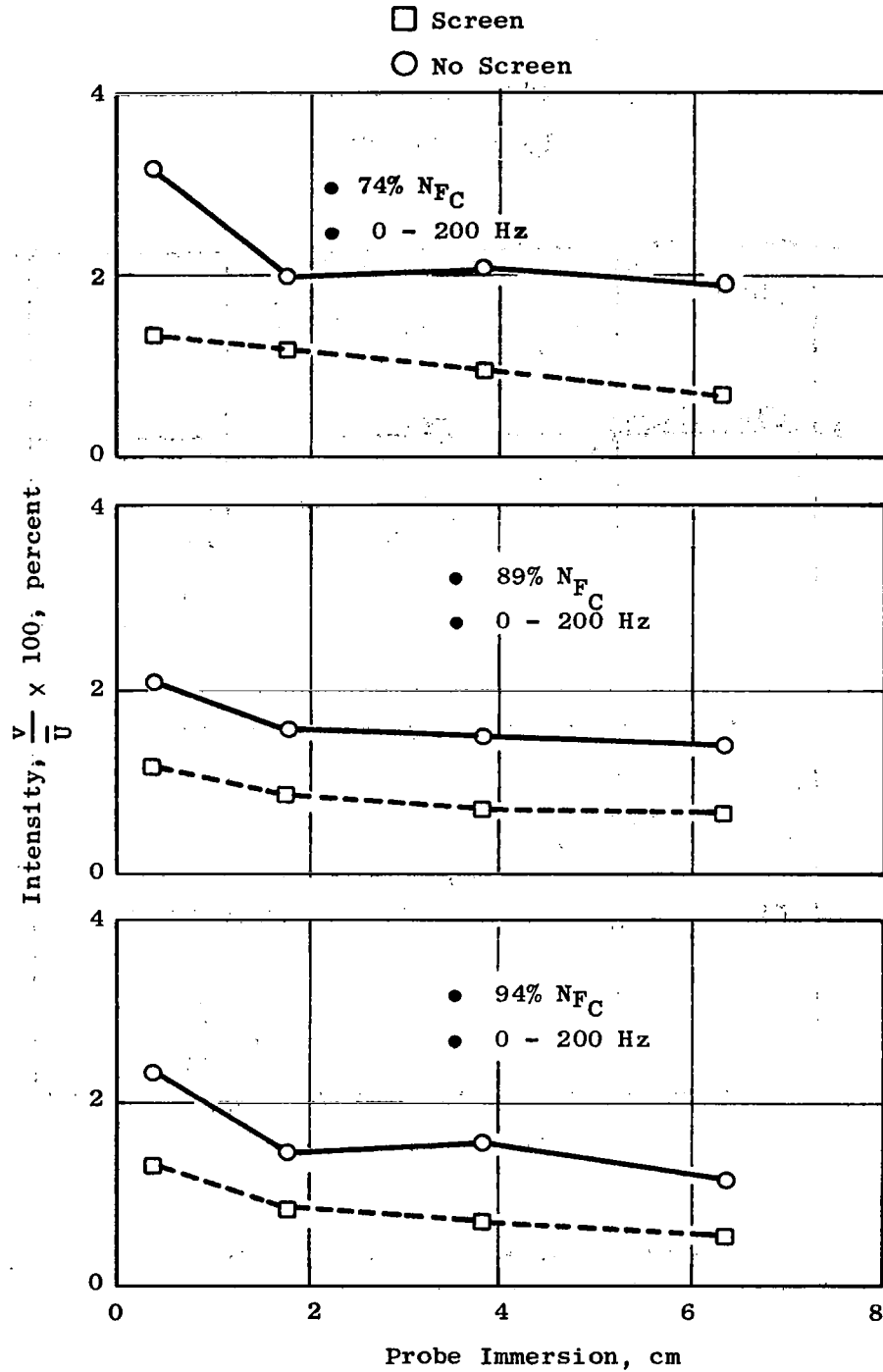


Figure 72. Circumferential Turbulence Intensity with and without Inlet Screen, Cylindrical Inlet.

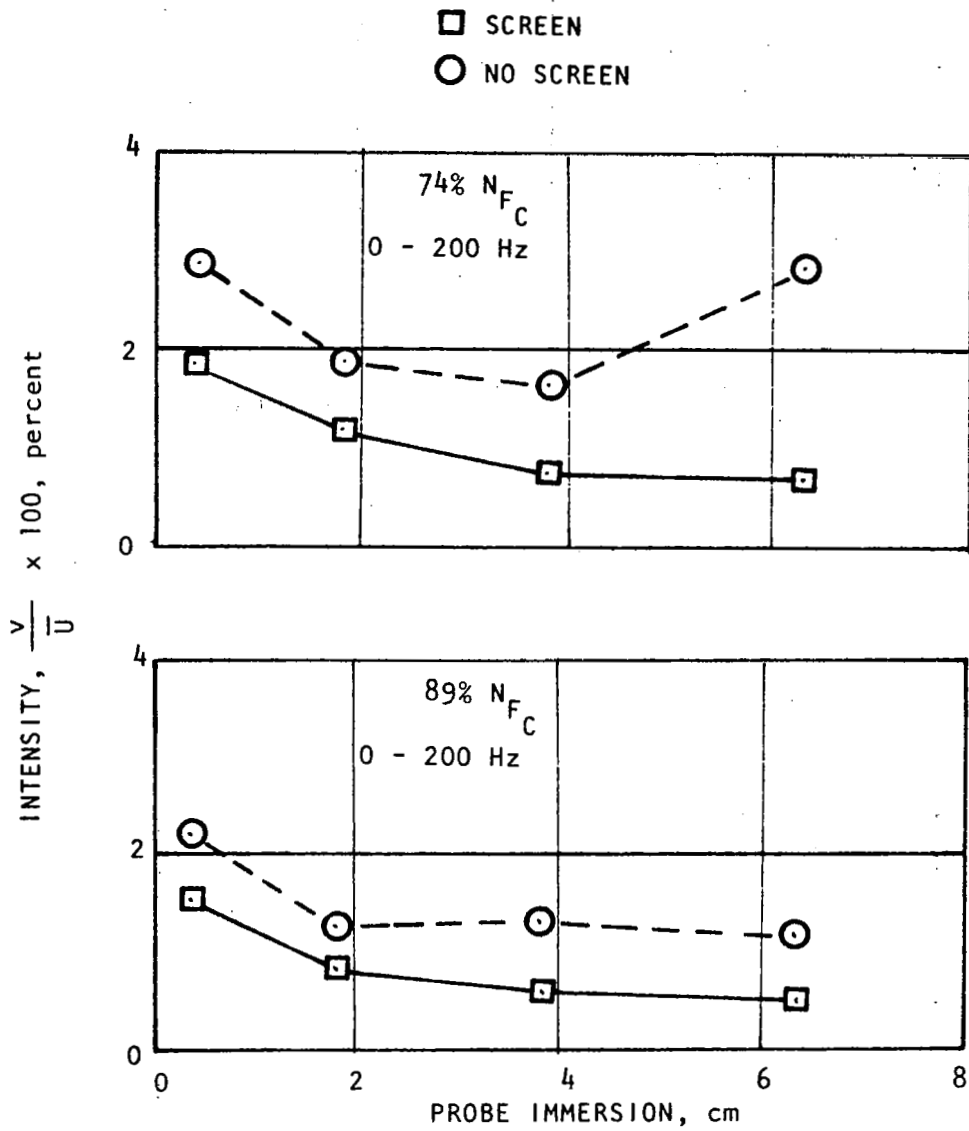


Figure 73. Circumferential Turbulence Intensity with and without Inlet Screen, Accelerating Inlet.

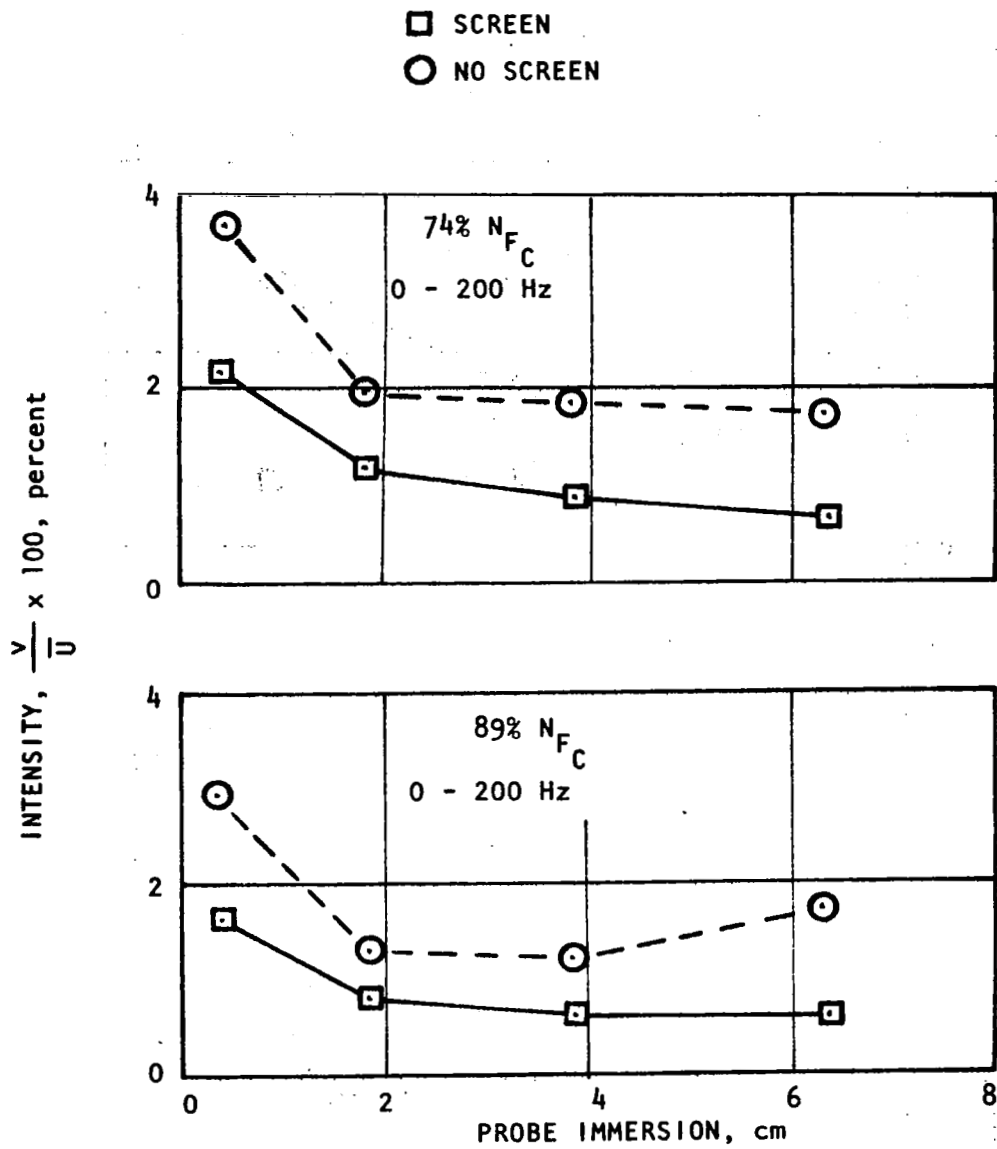


Figure 74. Circumferential Turbulence Intensity with and without Inlet Screen, Hybrid Inlet.

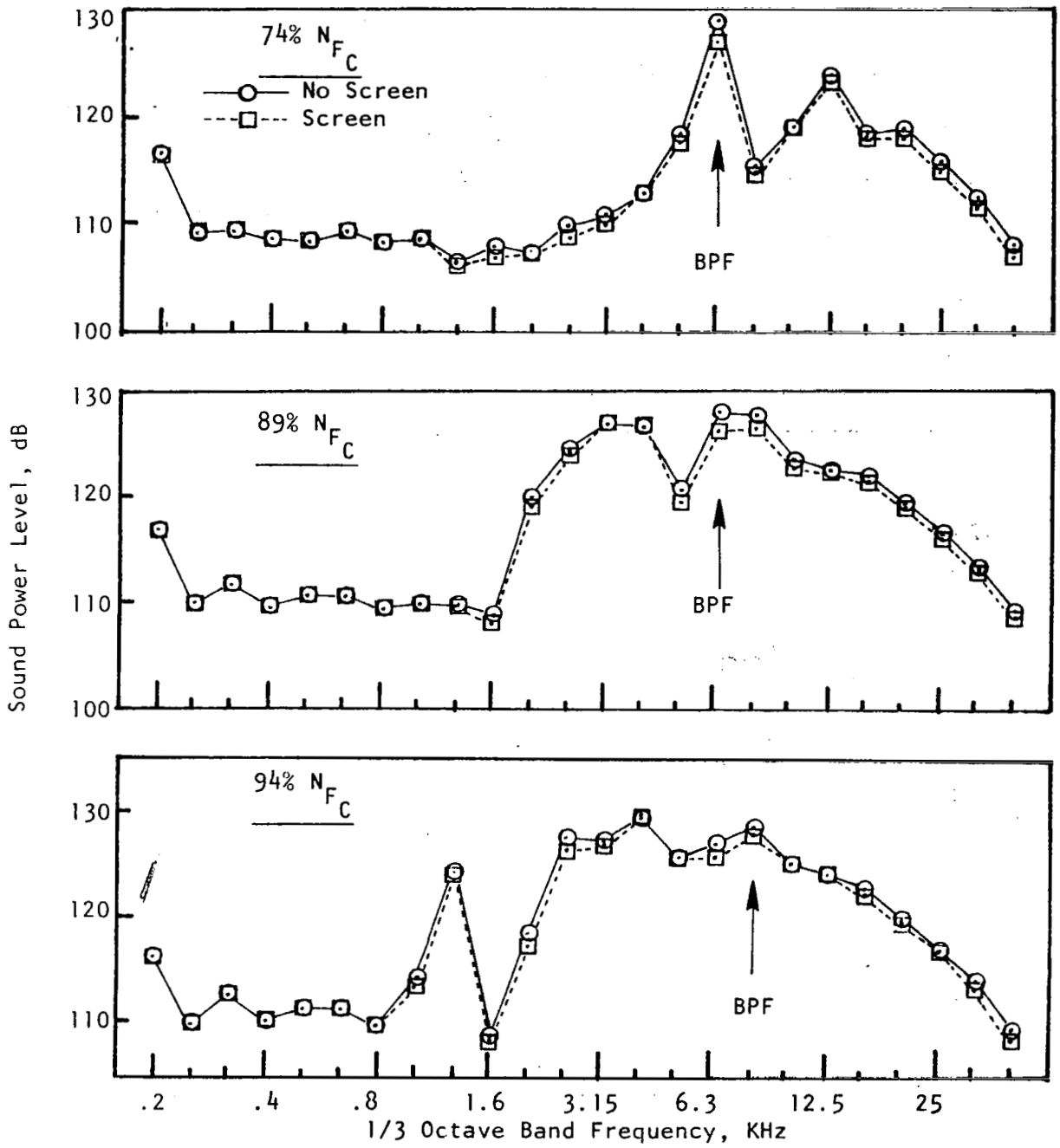


Figure 75. Effect of Inlet Screen on PWL Spectra, Cylindrical Inlet.

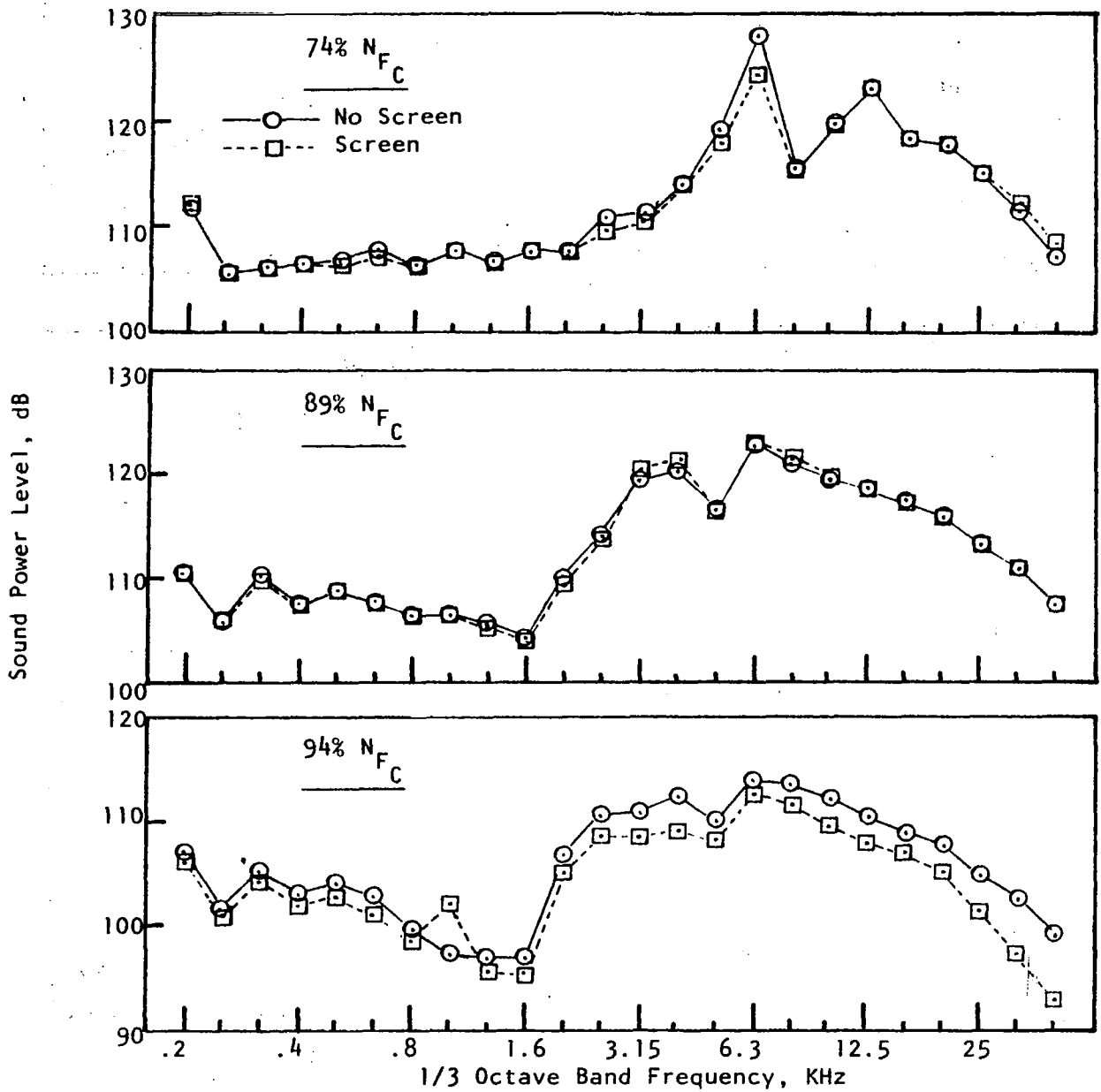


Figure 76. Effect of Inlet Screen on PWL Spectra, Accelerating Inlet.

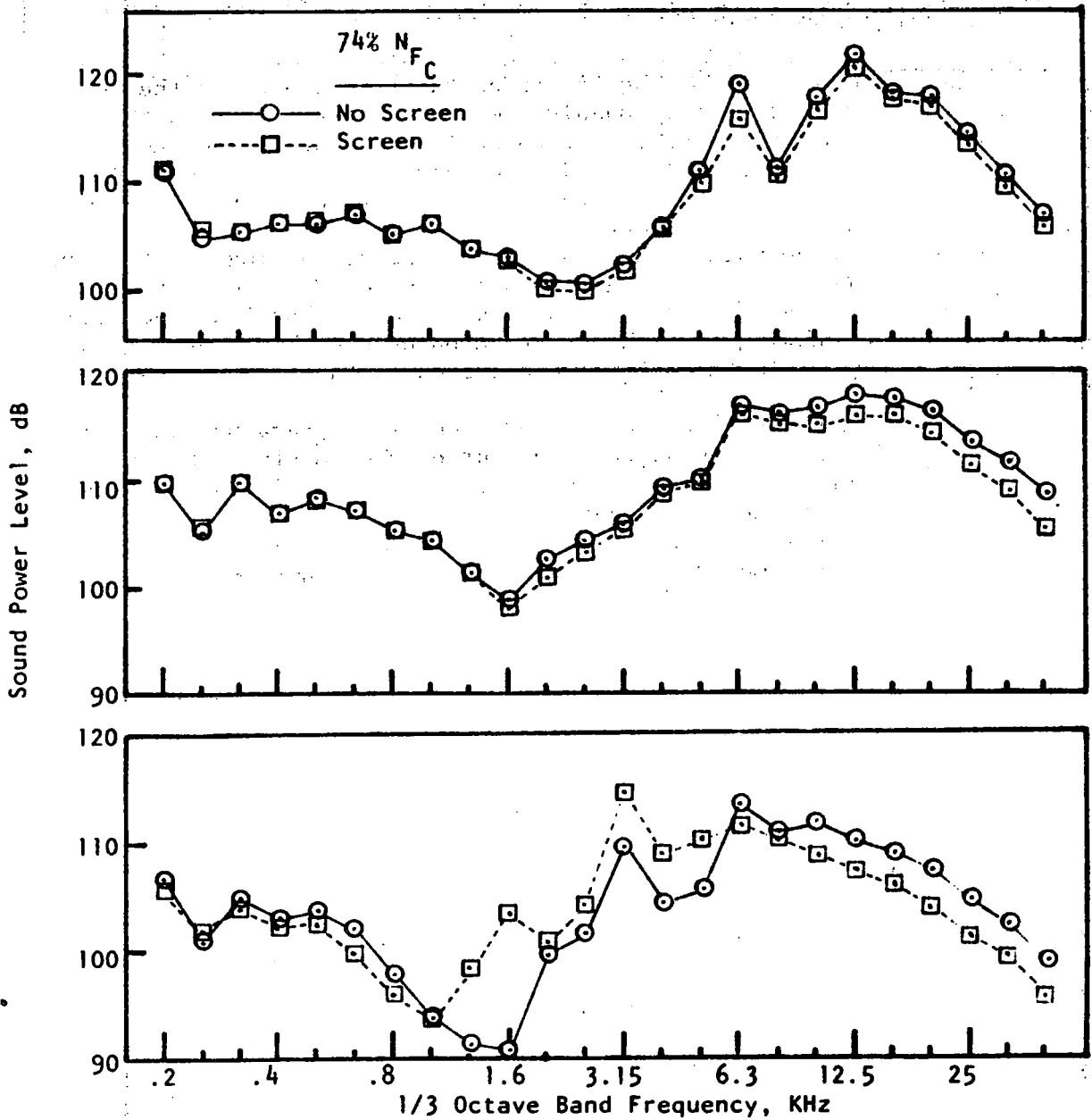


Figure 77. Effect of Inlet Screen on PWL Spectra, Hybrid Inlet.

The effect of the screen at the highest speed point was mixed, varying from showing essentially no change for the cylindrical inlet, to showing a decrease over the full spectral range for the accelerating inlet, and to showing an increase over part and a decrease over the remainder of the spectrum for the hybrid inlet.

This change in behavior of the effect of the screen between the lowest and the highest speed points is probably the result of a change in the source mechanism from one of turbulence-rotor interaction to the one which is responsible for MPT generation. And, the data for the intermediate speed setting is probably the consequence of a mixture of these two effects.

At the lowest speed point, the 1/3 octave band containing the BPF tone varied throughout the farfield arc as shown in Figure 78. The difference caused by the inlet screen varied from zero up to more than 6 dB reduction (never an increase) showing that the inlet turbulence without the screen was an important factor in the BPF noise observed in this test setup.

There is reason to believe that the BPF tone which remained when the screen was installed still contained rotor-turbulence interaction generated noise. The axial turbulence scales, even with the screen installed, were still well above lengths needed to generate pure tone noise. Also, turbulence intensities in the important blade tip region seldom fell much below 2 percent. Further noise reductions may have been obtained with larger decreases in turbulence.

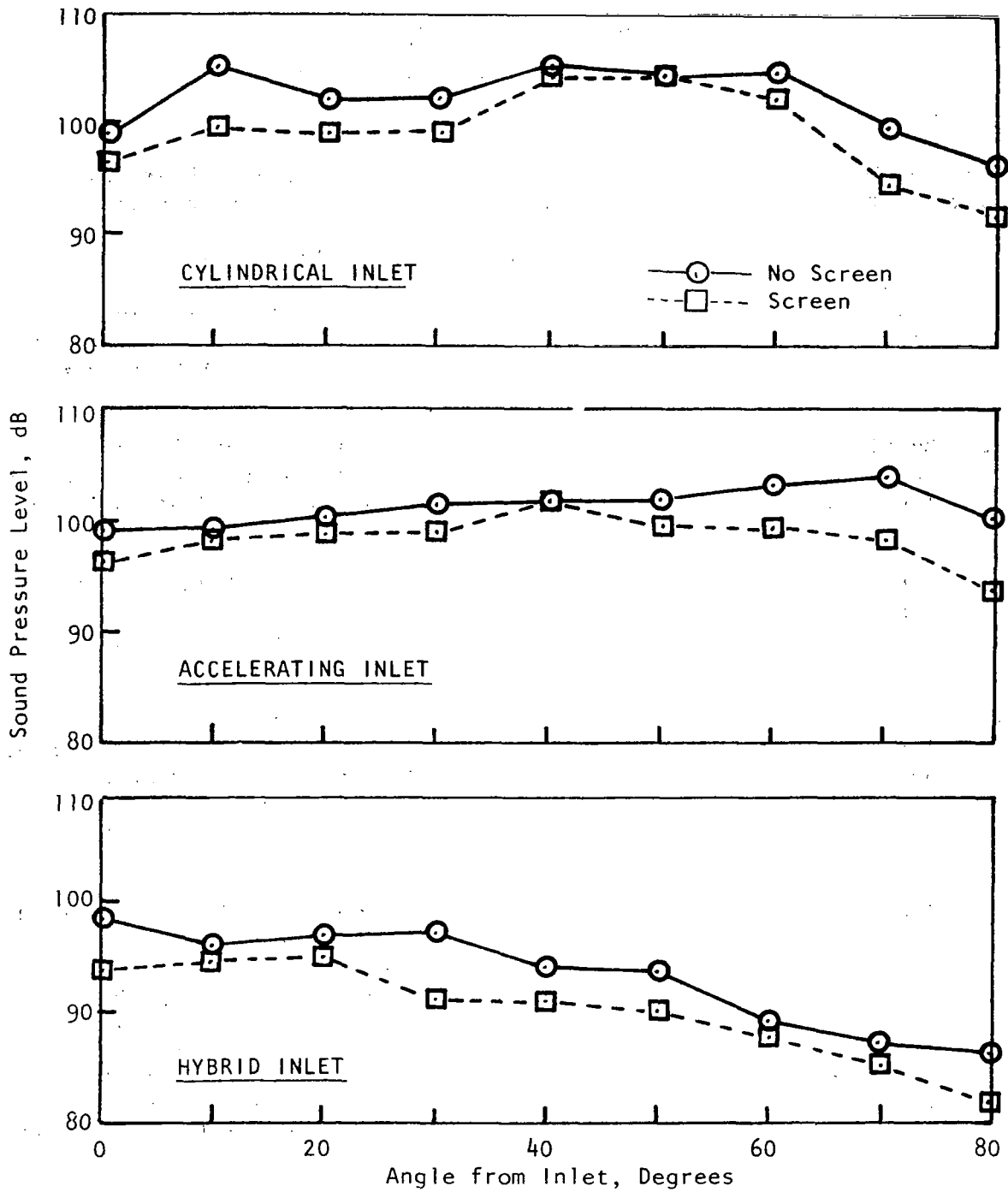


Figure 78. Effect of Inlet Screen on BPF 1/3 Octave Band Level as a Function of Farfield Angle, 74% N_{FC} .

SECTION 7.0

CONCLUSIONS

Based upon the analytical and experimental results from the program described in this report, the following conclusions have been reached:

1. The analysis of Zorumski as implemented in the computer program ACTAMD predicts the correct magnitude and proper trends of suppression, within about 50% of that measured, even with the relatively crude mathematical models used to define the source characteristics and to estimate the acoustic treatment impedance components under the actual test conditions.
2. Multi-segmented acoustic treatment provided substantial improvement, relative to single phase (uniform) treatment, over a broad range of low frequencies. This improved performance was found not only for the cylindrical but also for the hybrid inlet.
3. The accelerating inlet concept provides substantial amounts of suppression when the average throat Mach number is in the range of 0.72 to 0.79, without compromising the aerodynamic performance of the inlet.
4. In the hybrid inlet, the suppression was found to be less than the linear sum of that for the accelerating inlet and for the treatment, based on data for each effect measured separately. Acoustic probe data on blade-passing-frequency tone levels suggests that the difference is not in the loss of treatment effectiveness but is a result of reduced suppression in the throat region.
5. The measurement of the spinning modes by means of the acoustic mode probe used in this program was possible for subsonic tip speeds of the stage, when the measurement was made on the source side of the treatment. Some question remains with regard to the repeatability of the data, and there is some evidence that the probe, itself, influenced the sound field; in future work, attempts at such measurement on compressor or fan inlets should investigate the feasibility and suitability of flush wall mounted sensors. Radial as well as circumferential modal information is required, whichever technique is used.
6. Inlet turbulence levels associated with the test configuration and setup used in this program can be reduced by an inlet screen. Reduction of the blade-passing-frequency and harmonic tones of the test vehicle resulted when a screen was added in the current investigation; some residual turbulence-rotor interaction noise was still present even after the screen was added.

repeatability of the data, and there is some evidence that the probe, itself, influenced the sound field; in future work, attempts at such measurement on compressor or fan inlets should investigate the feasibility and suitability of flush wall mounted sensors. Radial as well as circumferential modal information is required, whichever technique is used.

6. Inlet turbulence levels associated with the test configuration and setup used in this program can be reduced by an inlet screen. Reduction of the blade-passing-frequency and harmonic tones of the test vehicle resulted when a screen was added in the current investigation; some residual turbulence-rotor interaction noise was still present even after the screen was added.

REFERENCES

1. Zorumski, W.; "Acoustic Theory of Axisymmetric Multisectional Ducts", NASA TR R-419, May 1974.
2. Hanson, D.B.; "The Spectrum of Rotor Noise Caused by Atmospheric Turbulence", Acoustical Society of America, Spring Meeting, New York City, April 1974.
3. Pickett, G.F.; "Effects of Non-Uniform Inflow on Fan Noise", Acoustical Society of America, Spring Meeting, New York City, April 1974.
4. Hanson, D.B.; "Measurements of Static Inlet Turbulence", AIAA Spring Meeting, Hampton, Va., 1975.
5. Lansing, D.L., and Zorumski, W.E.; "Effects of Wall Admittance Changes on Duct Transmission and Radiation of Sound", J. Sound and Vib., Volume 27, No. 1, March 8, 1973, pp. 85-100.
6. Zorumski, William E.; "Noise Suppressor", U.S. Patent 3 830 335, August 20, 1974.
7. Tyler, J.M., and Sofrin, T.F.; "Axial Flow Compressor Noise Studies", SAE Transactions, 70, 1962, pp. 309-332.
8. Kraft, R.E., and Wells, W.R.; "Adjointness Properties for Differential Systems with Eigenvalue-Dependent Boundary Conditions, with Application to Flow Duct Acoustics", Journal of the Acoustical Society of America, Volume 58, Supp. 1, Fall 1975, p. 56, (Abstract).
9. Keith, J.S., et al.; "Analytical Method for Predicting the Pressure Distribution About a Nacelle at Transonic Speeds," NASA CR-2217, July 1973.
10. Rice, E.J.; "A Model for the Pressure Excitation Spectrum and Acoustic Impedance of Sound Absorbers in the Presence of Grazing Flow", AIAA Paper No. 73-995, October 1973.
11. Phillips, B.; "Effects of High-Wave Amplitude and Mean Flow on a Helmholtz Resonator", NASA TMX-1582, May 1968.
12. "Standard Values of Atmospheric Absorption as a Function of Temperature and Humidity for use in Evaluating Aircraft Flyover Noise", SAE Aerospace Recommended Practice 866, August 1964.
13. Scheid, F.; Theory and Problems of Numerical Analysis, McGraw-Hill, New York, 1968, p. 293.

REFERENCES (Cont'd)

14. Kraft, R.E., and Posey, J.W.; "Preliminary In-Duct Measurement of Spinning Modes in the Inlet of a Rotating Vehicle", Journal of the Acoustic Society of America, Volume 59, Supp. No. 1, Spring 1976, (Abstract).
15. Posey, J.W.; "Comparison of Cross-Spectral and Signal Enhancement Methods for Mapping Steady State Acoustic Fields in Turbomachinery Ducts", NASA TMX-73916, August 1976.
16. Motsinger, R.E., Kraft, R.E., Zwick, J.W.; "Design of Optimum Acoustic Treatment for Rectangular Ducts with Flow", ASME Paper No. 76-GT-113, December 1975.
17. "Definitions and Procedures for Computing the Perceived Noise Level of Aircraft Noise", SAE Aerospace Recommended Practice, 865A, August 1969.
18. Mani, R.; "Noise Due to Interaction of Inlet Turbulence with Isolated Stators and Rotors", J. of Sound and Vibration, 17, 251-260 (1971).